FREQUENCY CONVERSION OF SINGLE PHOTONS: PHYSICS, DEVICES, AND APPLICATIONS

A DISSERTATION
SUBMITTED TO THE DEPARTMENT OF APPLIED PHYSICS
AND THE COMMITTEE ON GRADUATE STUDIES
OF STANFORD UNIVERSITY
IN PARTIAL FULFILLMENT OF THE REQUIREMENTS
FOR THE DEGREE OF
DOCTOR OF PHILOSOPHY

Jason Scott Pelc
July 2012

Report Documentation Page	*Form Approved* *OMB No. 0704-0188*

Public reporting burden for the collection of information is estimated to average 1 hour per response, including the time for reviewing instructions, searching existing data sources, gathering and maintaining the data needed, and completing and reviewing the collection of information. Send comments regarding this burden estimate or any other aspect of this collection of information, including suggestions for reducing this burden, to Washington Headquarters Services, Directorate for Information Operations and Reports, 1215 Jefferson Davis Highway, Suite 1204, Arlington VA 22202-4302. Respondents should be aware that notwithstanding any other provision of law, no person shall be subject to a penalty for failing to comply with a collection of information if it does not display a currently valid OMB control number.

1. REPORT DATE **JUL 2012**	2. REPORT TYPE	3. DATES COVERED **00-00-2012 to 00-00-2012**

4. TITLE AND SUBTITLE **Frequency Conversion Of Single Photons: Physics, Devices, and Applications**	5a. CONTRACT NUMBER 5b. GRANT NUMBER 5c. PROGRAM ELEMENT NUMBER
6. AUTHOR(S)	5d. PROJECT NUMBER 5e. TASK NUMBER 5f. WORK UNIT NUMBER
7. PERFORMING ORGANIZATION NAME(S) AND ADDRESS(ES) **Stanford University,Stanford,CA,94305**	8. PERFORMING ORGANIZATION REPORT NUMBER
9. SPONSORING/MONITORING AGENCY NAME(S) AND ADDRESS(ES)	10. SPONSOR/MONITOR’S ACRONYM(S) 11. SPONSOR/MONITOR’S REPORT NUMBER(S)

12. DISTRIBUTION/AVAILABILITY STATEMENT

Approved for public release; distribution unlimited

13. SUPPLEMENTARY NOTES

14. ABSTRACT

The ability to manipulate the carrier frequency of quantum states of light, through a process called quantum frequency conversion (QFC), has numerous applications for both technology and basic science. For example, one can upconvert a single-photonlevel signal in the 1.5- m telecommunications band (where single-photon detection has been challenging) to a visible wavelength to take advantage of well-developed single-photon detectors based on silicon avalanche photodiodes. On the more fundamental side, the manipulation of a single photon’s frequency may enable the construction of networks of dissimilar quantum systems, whereby one can imagine generating many-body entangled quantum states over vast distances.

15. SUBJECT TERMS

16. SECURITY CLASSIFICATION OF:			17. LIMITATION OF ABSTRACT	18. NUMBER OF PAGES	19a. NAME OF RESPONSIBLE PERSON
a. REPORT **unclassified**	b. ABSTRACT **unclassified**	c. THIS PAGE **unclassified**	**Same as Report (SAR)**	**174**	

Standard Form 298 (Rev. 8-98)
Prescribed by ANSI Std Z39-18

© 2012 by Jason Scott Pelc. All Rights Reserved.
Re-distributed by Stanford University under license with the author.

This work is licensed under a Creative Commons Attribution-Noncommercial 3.0 United States License.
http://creativecommons.org/licenses/by-nc/3.0/us/

This dissertation is online at: http://purl.stanford.edu/zs827ns8173

I certify that I have read this dissertation and that, in my opinion, it is fully adequate in scope and quality as a dissertation for the degree of Doctor of Philosophy.

Martin Fejer, Primary Adviser

I certify that I have read this dissertation and that, in my opinion, it is fully adequate in scope and quality as a dissertation for the degree of Doctor of Philosophy.

Robert Byer

I certify that I have read this dissertation and that, in my opinion, it is fully adequate in scope and quality as a dissertation for the degree of Doctor of Philosophy.

Yoshihisa Yamamoto

Approved for the Stanford University Committee on Graduate Studies.

Patricia J. Gumport, Vice Provost Graduate Education

This signature page was generated electronically upon submission of this dissertation in electronic format. An original signed hard copy of the signature page is on file in University Archives.

Abstract

The ability to manipulate the carrier frequency of quantum states of light, through a process called quantum frequency conversion (QFC), has numerous applications for both technology and basic science. For example, one can upconvert a single-photon-level signal in the 1.5-μm telecommunications band (where single-photon detection has been challenging) to a visible wavelength to take advantage of well-developed single-photon detectors based on silicon avalanche photodiodes. On the more fundamental side, the manipulation of a single photon's frequency may enable the construction of networks of dissimilar quantum systems, whereby one can imagine generating many-body entangled quantum states over vast distances.

Quantum frequency conversion will only be useful if it can be done both efficiently and with little added noise. We demonstrated a conversion efficiency exceeding 99.99% using reverse-proton-exchange waveguides in periodically poled lithium niobate with approximately 150 mW of pump power. Noise has been a more serious issue: the generation of noise photons, due to inelastic scattering of light from the strong pump laser used to drive the frequency conversion, has limited the utility of QFC devices in many applications. We present an analysis of the two primary noise processes in QFC devices (spontaneous Raman scattering and spontaneous parametric fluorescence), and offer solutions on how they may be either mitigated or avoided completely.

We then discuss applications of QFC devices for up- and downconversion of single-photon signals. We used a long-wavelength pump to enable high-efficiency and low-noise single-photon detection for 1.5-μm telecom band signals, and demonstrated a cascaded frequency conversion approach that enabled low timing jitter as well. We also demonstrated a downconversion quantum interface, in which the emission from a single semiconductor quantum dot at a wavelength of 910 nm was downconverted to 1.56 μm while maintaining the single-photon character of the light. The results presented in this dissertation indicate a promising future for QFC devices as the field of quantum communications matures.

Acknowledgements

Life is like riding a bicycle.
To keep your balance you must keep moving.
—Albert Einstein, 1930

Graduate school takes a long time. It is a series of ups and downs, many frustrations with the occasional triumph, and for me, as someone who spent a good deal of effort trying to manipulate and measure single photons, a lot of time spent in very dark rooms. But, more than anything else, my graduate school experience has been defined by the amazing people I have had the chance to interact with, without whom this work would not have been possible.

First and foremost, I owe a tremendous debt of gratitude to my advisor, Prof. Marty Fejer. Marty has an encyclopaedic knowledge of physics, and an astounding ability to explain difficult concepts with clarity. I am extremely grateful not only for the support, guidance, and technical insight Marty gave through all phases of the projects described here, but also for the freedom he granted me to take whatever left turns it seemed might be interesting at the time, even when he presumably knew (well before I did) that they might not pan out to be the great conceptual leaps I might have hoped.

I am also thankful to the support of my two readers, Professors Bob Byer and Yoshi Yamamoto. I have had the privilege to interact with them both throughout my Ph.D. career, and I'd like to thank them both for the rich technical (and nontechnical) discussions, as well as for teaching some of the best courses I took at Stanford (in particular, Prof. Byer's Laser lab and Nonlinear Optics lab courses).

Carsten Langrock and Qiang Zhang have both been instrumental in helping me develop experimental skills and gain an appreciation for the "interesting" topics in the field. Carsten taught me everything I know about the dark arts of waveguide fabrication, and was always available to help debug the fab processes. Qiang introduced me to many of the experimental techniques in quantum optics, and was often the sounding board for my (usually half-baked) ideas for new applications of PPLN waveguides. His enthusiasm for this field is infectious, and I have no doubt he will continue to do great things in his new role as professor at USTC in Shanghai. I would also like to thank Qiang and his student Shentu Guoliang for their hard work and for their hospitality in hosting me in Shanghai in the Fall of 2011 for a visit.

These projects have been highly collaborative. Our group is primarily a device group, and my projects have focused on applications of our devices in quantum optics. As such, nearly all of my projects involved a great deal of collaboration, not only within the Byer-Fejer group but outside it as well. Several collaborators deserve special recognition.

Firstly, the quantum dot team: Kristiaan De Greve, Leo Yu, Peter McMahon, and Chandra Natarajan. The experiments described in Chapter 6 were intimidatingly complicated, and everyone here was indispensible in making them work. This project was exhilarating, and exhausting—I still don't know how these guys are able to work as hard and as tirelessly as they do on making experiments as complicated as quantum dot spin-control work. To Leo Yu, I owe a special debt of gratitude: Leo and I built the bulk DFG setup together, and Leo rapidly came to take control of running the system and developed a critical improvement (pulsing the signal source) that proved crucial in getting the final experiment to work. Leo has some amazing further experiments planned involving downconversion of quantum dot photons, and I wish him the best of luck in carrying them through—it's satisfying to know that the waveguides we developed are left in such capable hands.

Next, the team of Xiao Tang at the Information Technology Lab at NIST in Gaithersburg, MD: Paulina Kuo, Lijun Ma, and Oliver Slattery. The collaboration with NIST got started when Lijun contacted Carsten in 2009 and it continues on to today. Xiao provided the Tm-doped fiber amplifier which was crucial in the demonstration of long-wavelength-pumped upconversion detection described in Sec. 5.3. Paulina, a former student of Marty's who also served as an early mentor to me during her time at Stanford, joined Xiao's group at NIST in September, 2011 and I was thrilled to get the chance to work with her on the multichannel upconversion experiment described in Sec. 7.2. I had a great visit to NIST in January, 2012 to set up the multichannel upconverter, and I'd like to thank Paulina for her help on that visit and also for her continued hard work refining the measurements after I'd left.

Next, to two particular members of the Byer–Fejer group who joined at roughly the same time I did and with whom I've sat next to in the office for several years: Chris Phillips and Derek Chang. Chris and I have worked closely on a number of projects over the years. Even though our projects had very different themes, we often found ourselves thinking about the same nonlinear optical processes, and I am a grateful beneficiary of his incredible toolbox of skills in theory and simulation. Derek has been the other primary PPLN waveguide fabricator in the group: he provided the waveguides for the SHG characterization of random duty-cycle errors in Sec. 4.1.

To the rest of the Byer–Fejer group, I offer sincere thanks. It has been a wonderfully collegial atmosphere in which to do research, and the remarkable breadth of topics is inspiring. After I joined the group, I worked with Joe Schaar on a project that really helped me gain a foothold into the often confusing and jargon-filled world of nonlinear optics. Karel Urbanek has offered lots of technical support. Roger Route has made sure whenever I *really* needed to buy something we could find the funds, and reliably provided a healthy dose of negativity around the lunch table. Charlie Rudy and Alireza Marandi have provided insight and many interesting discussions. I also want to thank Supriyo Sinha, Brian Lantz, Nick Leindecker, Chris McGuinness, Ashot Markosyan, Judith Schwesyg, Angie Lin, Graham Allen, and Amber Bullington for their help. To the new generation of students, Yu-Wei Lin, Vahid Esfandyarpour, and Stephen Wolf, I offer my best wishes as they move forward with their research.

I'd also like to thank the administrative staff of the Applied Physics department, Paula Perron and Claire Nicholas, for their help. And to our group admin Vivian Drew, without whom all work in the Byer–Fejer group would grind to a halt. Tom

Carver has been a tremendous help in the microfab shop, and I appreciate the hard work of Tim Brand and his ensemble at the Crystal Shop for fabricating the monolithic OPO sample and polishing many rounds of waveguide samples. Additional researchers around the Ginzton lab who have also been instrumental have been Steve Sensarn, Il-Woong Jung, Kelley Rivoire, Gary Shambat, Sonia Buckley, Kiarash Aghaie, Na Young Kim, Darin Sleiter, and Kaoru Sanaka.

To my family and friends, who have been there to provide help, and to provide diversion. It's not possible for me to name all the friends who've provided useful distractions during my years at Stanford, so I won't even try. It has been a pleasure to move back within an easy drive's distance of my parents house: to Dr. Mom and Dr. Dad, I thank you not only for the more-than-occasional home-cooked meals, but also for all the technical and career advice. To my sister Emily, I wish you the best of luck in your burgeoning music career. And to my extended family, in particular my grandparents, I thank you for the support and encouragement. Lastly, to Shirley Li, my original physics p-set buddy and friend for many years, and much more than that for the last three: you are my inspiration, and *I love you*.

I am grateful for support as a Robert N. Noyce Stanford Graduate Fellow, and for a Stanford Humanities and Sciences Dean's Fellowship. Additional support for the group was from the US Air Force Office of Scientific Research, from Crystal Technology, Inc. for providing $LiNbO_3$ substrates, from Quantum Telecom, Inc., and from the NIST Quantum Information Initiative.

Contents

Abstract **iv**

Acknowledgements **vi**

1 Introduction **1**
- 1.1 Overview of this dissertation 3

2 Theory and literature review **5**
- 2.1 Three-wave mixing in waveguides 5
- 2.2 Quantum frequency conversion (QFC) 10
- 2.3 Historical overview 13

3 RPE PPLN waveguides **18**
- 3.1 Quasi-phasematching and periodically poled lithium niobate (PPLN) 19
- 3.2 Fabrication of reverse-proton-exchange (RPE) waveguides 23
- 3.3 Device characterization and packaging 26
  - 3.3.1 Loss Measurements 26
  - 3.3.2 Phasematching characterization 29
  - 3.3.3 Pigtailing 30

4 Noise processes in QFC devices **32**
- 4.1 QPM random duty-cycle errors: definitions, characterization, and nonlinear optical effects 34
  - 4.1.1 Theory of SHG in disordered QPM gratings 35

4.1.2 Characterization of RDC errors 38
4.1.3 Observation of QPM pedestal 40
4.1.4 Domain-disorder-enhanced parametric fluorescence 43
4.1.5 RDC error tolerances 50
4.2 Spontaneous Raman scattering 52
4.2.1 Raman spectroscopy of H^+:$LiNbO_3$ 54
4.2.2 Raman noise in QFC devices 57
4.3 Design implications 60

5 Upconversion single-photon detectors 61
5.1 Single-photon detection with avalanche photodiodes 61
5.2 Monolithic OPO long-wavelength pump source 63
5.3 Long-wavelength-pumped upconversion detector at 1.55 μm 67
5.3.1 Experimental setup and characterization 67
5.3.2 Single-photon performance 72
5.4 Upconversion detection of 1-μm radiation 76

6 Single-photon downconversion 79
6.1 Quantum dot single-photon sources 79
6.2 Classical characterization of the downconversion system 83
6.3 Single-photon experiments 87
6.4 Summary 93

7 Advanced QFC devices 95
7.1 Cascaded quantum frequency conversion and applications 95
7.1.1 Cascaded conversion theory and device design 96
7.1.2 Cascaded upconversion for high-speed single-photon detection 99
7.1.3 Two-step downconversion of quantum light sources 102
7.2 Multichannel and time-frequency converters 105
7.2.1 Multichannel upconversion and applications 105
7.2.2 Upconversion with multi-wavelength sampling 116
7.2.3 Future work 119

8 Conclusion **121**
8.1 Summary of contributions 121
8.2 Outlook and future directions 125

A Calculation of QPM pedestal **127**

B Pedestal-QPM Čerenkov-idler interactions **133**

Bibliography **138**

List of Tables

5.1 Performance comparison of single-photon detectors based on either Si or InGaAs avalanche photodiodes 63
5.2 Loss budget and potential performance improvements for 1.5-μm long-wavelength-pumped upconversion single-photon detector. 74

List of Figures

2.1 Photon evolution versus distance in a sum-frequency generator 9

2.2 Schematic diagram of the quantum frequency conversion process in a $\chi^{(2)}$ material. 11

2.3 Conversion efficiency versus pump power in a QFC device. 12

3.1 Intensity evolution of generated sum-frequency radiation for three different phasematching conditions. 20

3.2 Typical voltage and current waveforms during whole-wafer electric-field periodic poling. 22

3.3 Process flow for fabrication of RPE PPLN waveguides. 24

3.4 Schematic of an RPE PPLN waveguide. 26

3.5 Optical transmission vs. wavelength for an RPE PPLN waveguide low-finesse cavity, for calculation of waveguide losses via the Fabry-Perot technique. 28

3.6 Quasi-phasematching tuning curves for RPE PPLN waveguides. . . . 29

3.7 Closeup image of a fiber pigtail. 30

4.1 Schematic of noise processes in (a) short-wavelength-pumped and (b) long-wavelength-pumped quantum frequency upconverters. 33

4.2 Schematic of QPM domains showing random duty-cycle errors. 35

4.3 Simulation and analytic theory of SHG in a QPM grating with domain disorder. 37

4.4 Surface topography of etched PPLN wafer measured using Zygo interferometry. 40

4.5 Random duty-cycle error histogram and Gaussian fit. 41
4.6 Experimental setup for observation of SHG QPM pedestal. 42
4.7 Measured relative SHG efficiency $\langle|\tilde{g}(\lambda)|^2\rangle$ in RPE PPLN waveguide with random duty-cycle errors. 43
4.8 Frequencies and wavelengths involved in downconversion of a weak signal at $\lambda_2 = 633$ nm to a target wavelength $\lambda_1 = 1.56$ μm. 44
4.9 Experimental setup for measurement of weak-signal DFG and noise generation via spontaneous parametric fluorescence. 45
4.10 Measured conversion efficiency and parametric fluorescence in short-wavelength-pumped downconverter. 47
4.11 Uponversion of parametric fluorescence noise and fit to semiclassical model. 49
4.12 Random duty-cycle error tolerances for a QFC device with domain disorder. 51
4.13 Diagram of spontaneous Raman scattering in either Stokes or anti-Stokes configurations. 53
4.14 Measured $LiNbO_3$ Raman spectrum and fit to a sum of Lorentzians. . 55
4.15 Spontaneous Raman scattering noise photon spectral density calculated from measured Raman spectrum 59

5.1 Monolithic PPLN OPO schematic diagram for long-wavelength-pumped upconversion single-photon detector for 1.5-μm. 64
5.2 Monolithic OPO signal wavelength versus temperature. 65
5.3 System setup for 1.55-μm long-wavelength-pumped upconversion single-photon detector. 67
5.4 Measured TmDFA optical noise spectrum from 1470 nm to 1580 nm. 68
5.5 Temperature tuning of 1.8 + 1.55-μm SFG waveguide. 70
5.6 Classical-signal characterization of 1.5-μm upconversion device. . . . 71
5.7 1.55-μm upconversion detector performance, for $\lambda_p = 1810$ nm 73
5.8 1.5-μm upconversion SPD noise counts versus pump–signal frequency difference, and calculation of Raman-induced noise counts. 75

5.9 1078-nm upconversion detector performance, for $\lambda_p = 1540$ nm 77

6.1 Band structure of a negatively charged quantum dot in its ground and excited states 81
6.2 Intensity autocorrelation $g^{(2)}(\tau)$ of emission from the quantum dot used in the downconversion experiment. 82
6.3 Experimental setup for downconversion of single photons from quantum dots. 84
6.4 Bulk DFG results for generation of pump radiation at $\lambda_p \approx 2.2$ μm. . 85
6.5 Classical cross-correlation characterization of pulsed downconverter. . 87
6.6 Sampling the spontaneous emission waveform of the quantum dot via pulsed downconversion. 89
6.7 Rabi oscillations in photon counts for downconverted quantum dot single photons. 90
6.8 Photon statistics for downconverted quantum dot light, showing preservation of single-photon character. 92

7.1 Schematic of cascaded frequency upconversion, and PDE vs. wavelength of two common commercial low-jitter Si APD single-photon detectors. 96
7.2 Photon-flux evolution in a two-component grating optimized for efficient cascaded upconversion. 98
7.3 Experimental setup for cascaded upconversion of single photons. . . . 100
7.4 Temperature tuning of two-step upconverter. 101
7.5 Conversion efficiency of two-stage upconverter. 102
7.6 Timing jitter measurement of two-stage upconversion single-photon detector. 103
7.7 Schematic of two-step downconversion of single-photons from diamond NV centers. 104
7.8 Schematic of frequencies involved in multichannel upconversion. . . . 106
7.9 Theoretical and measured QPM tuning curves for SFG in phase-modulated PPLN waveguide. 108

7.10 Phase-modulation period versus channel spacing for two-channel SFG device. 109
7.11 Experimental setup for multichannel upconversion system. 110
7.12 Photon detection efficiency and noise count rate of two-channel upconverter. 112
7.13 Measured single-channel and dual-channel count rates versus input photon flux for two-channel upconversion detector. 113
7.14 Measured second-order correlations $g^{(2)}(\tau)$ for coherent and quasi-thermal light sources using two-channel upconverter. 115
7.15 Timing diagram for detection of high-clock-rate signals via multi-wavelength sampling. 117
7.16 Timing performance of dual-channel upconversion detector. 118
7.17 Schematic of a single-photon time-frequency converter. 120

Chapter 1

Introduction

Computer networks form the basis of the internet and today represent our primary means of communication. They are based on binary switches using digital logic in semiconductor devices, and, even with the rapid rate of miniaturization, are at their heart classical devices. That is, the state of an individual logic device is either a “1” or a “0”. Quantum information processing enables superpositions of these binary states to evolve at the same time, allowing a degree of parallelism not possible in classical information processing [1]. It is known that a quantum computer could solve certain classes of problems exponentially faster (in terms of computational steps) than their classical counterparts. Although a large-scale quantum computer remains a distant goal, those features which enable quantum computation (namely entanglement and coherent superposition) are the very ones that have given quantum mechanics its reputation for being counterintuitive and bizarre. As such, the exploration of quantum computer primitives—the controllable quantum two-level systems and their interactions—makes a very worthwhile topic for research.

Quantum networks are a tantalizing concept. At its heart, a quantum network consists of a number of controllable quantum systems which can interact with each other while separated by some distance [2]. It therefore requires both a stationary quantum node (where information is stored and processed) and an appropriate interface by which distant nodes can communicate over a quantum channel. Most research on quantum networks has focused on optically controlled quantum nodes that interact via the emission and absorption of photons. Recently, a German team demonstrated an elementary two-node network whereby distributed entanglement was created across a distance 60 m as a single ^{87}Rb atom emitted a single photon which was transmitted down an optical fiber and captured by a second trapped ^{87}Rb atom [3].

There exist several promising candidate systems for quantum network nodes: namely the trapped neutral atoms mentioned already, nitrogen–vacancy color centers in diamond [4], and III-V semiconductor quantum dots [5]. However, all these candidate systems have optical transitions in the visible or near visible spectral region. If one is interested in extending the distance over which distributed entangled states can be created, it is evidently necessary to pursue a system whereby the photonic channel consists of transmission of single photons in the 1.5-μm spectral region, where the transmission loss in optical fiber is at its lowest value, below 0.2 dB/km. Such links require either development of a quantum node with 1.5-μm optical transitions, or use of a frequency conversion technique in which the carrier frequency of light can be translated while maintaining the quantum characteristics of the signal. This dissertation is concerned with the latter, which is accomplished through a technique called quantum frequency conversion, first proposed by Kumar in 1990 [6], and demonstrated shortly afterwards [7].

While we have here framed the discussion of quantum frequency conversion in the context of quantum networks, it has other applications in various scientific and technological fields. Frequency conversion in $\chi^{(2)}$ media has been a subject of active research since first observation of $\chi^{(2)}$ processes by Franken just over 50 years ago [8]. It has been used primarily for the generation of radiation at optical frequencies inaccessible with current laser technology, but in recent years the development of highly efficient $\chi^{(2)}$ frequency converters based on waveguides has enabled its use in nonlinear all-optical signal processing [9]. The results of this dissertation can be viewed as an extension of classical signal processing applications to the quantum realm. As quantum communications systems are in their infancy, we believe that the potential for future research along this direction is promising.

1.1 Overview of this dissertation

Chapter 2 presents the theory of frequency conversion in $\chi^{(2)}$ materials using both classical and quantum mechanical descriptions. We give an overview of experimental achievements in this field, and point out the primary impediments to progress towards a long-distance quantum network. Chapter 3 gives a description of the device technology we use for QFC: reverse-proton-exchange waveguides in periodically poled lithium niobate. The principles of quasi-phasematched frequency conversion devices are presented, along with device fabrication by periodic poling of ferroelectrics. We then describe the waveguide technology, giving some special attention to the fabrication and characterization procedures used in our lab to produce the highest quality devices possible.

A primary contribution of this dissertation is a detailed discussion of the non-idealities of the QFC process via the generation of noise photons, which will be presented in Chapter 4. Apart from technical noise (e.g. stray light or improperly filtered pump sources), the sources of noise in QFC devices can be traced to two physical effects. The first is parametric fluorescence, a process endemic to $\chi^{(2)}$ nonlinear materials. Naïve calculations of parametric fluorescence show that in the highly phase-mismatched regime it should not be a significant noise source, but imperfections in the fabrication of periodically poled gratings enhance the generation rate substantially, by up to a factor of about 10^4. Tolerances for these fabrication errors are derived. The second noise source is spontaneous Raman scattering. By a careful investigation of the Raman spectrum of $LiNbO_3$ we find certain system configurations by which Raman scattering can be avoided, leading to design rules by which we can achieve low-noise quantum frequency conversion for diverse applications in science and technology.

Chapters 5 and 6 present applications of QFC technology to the up- and down-conversion of single photons. Upconversion has been used as a technique to improve detection of infrared radiation since the early days of nonlinear optics [10]. It has also been the primary technological driver of quantum frequency conversion: quantum key distribution and other quantum communications technologies require high-efficiency, fast, and low-noise single-photon detectors for light in the spectral range in which optical fibers (the primary quantum channels) have the lowest attenuation: namely the region around $\lambda = 1.5$ μm. While some emerging 1.5-μm single-photon detection technologies are improving, the best single-photon detectors are those based on Si, which, due to the 1.1-eV bandgap of Si, are unable to detect photons with wavelengths longer than approximately 1 μm. Chapter 5 describes our efforts at developing upconversion single-photon detectors: we achieved, to the best of our knowledge, the highest efficiency long-wavelength-pumped (low-noise) upconversion detector for the 1.5-μm band, and demonstrated a 1-μm upconversion detector, with approximately 30 noise counts/s at peak conversion efficiency.

Chapter 6 presents a downconversion interface suitable for linking an InAs/GaAs quantum dot with an optical transition at 910-nm, a promising quantum network node candidate, with the 1.5-μm spectral window suitable for long-distance transmission down optical fiber. We demonstrate time-resolved downconversion of the single photons emitted from the quantum dot, and show that the photon statistics of the quantum dot emission are preserved. Additionally, through the observation of Rabi oscillations in the converted photons, we prove that downconversion system is fully compatible with the types of coherent control operations on the quantum dot spin needed for its use as a quantum network node.

In Chapter 7, we move past simple up- and downconversion devices and explore additional design space to bring added functionality to single-photon frequency conversion systems. We present two main concepts: first, we describe the demonstration of cascaded frequency conversion. As it is possible to achieve near-unity conversion efficiency of a single process in RPE PPLN waveguides, using approximately twice as much pump power it is possible to convert an input signal twice. As a proof-of-concept, we demonstrate two-stage frequency conversion of a 1.5-μm single-photon signal to the green spectral region for high-speed single photon detection. The second device concept is based on a multi-channel QFC device, whereby one can switch on and off multiple pumps to demultiplex a single-photon signal to enable higher clock-rate quantum communications systems. In Chapter 8, we conclude the dissertation, and describe some avenues for further research and development.

Chapter 2

Theory and review of quantum frequency conversion

In the following sections we provide a theoretical basis for both classical and quantum mechanical descriptions of three-wave interactions in $\chi^{(2)}$ nonlinear waveguides, and describe how these interactions can be used to translate the carrier frequency of a quantum state of light. We will also briefly review experimental work in this field.

2.1 Three-wave mixing in waveguides

Classical electromagnetic field theory can be used to describe nonlinear optical interactions [11]. Classical electromagnetism, encapsulated in Maxwell's equations and Newton's laws, describes the motion of free and bound charges in response to electric and magnetic fields, and then how the motion of charges acts as a source of electromagnetic radiation. As a prototypical three-wave interaction, we will study sum-frequency generation (SFG), in which a signal at ω_1 is combined with a pump at ω_p to produce an output at $\omega_2 = \omega_1 + \omega_p$. The goal of this treatment will be to derive coupled wave equations for field amplitudes at each of the frequencies ω_j with $j \in \{1, p, 2\}$. This subject is treated in all standard texts on nonlinear optics [12], so we offer only an abbreviated discussion. Maxwell's equations are given by

$$\nabla \times \tilde{\mathbf{E}} = -\frac{\partial \tilde{\mathbf{B}}}{\partial t}, \tag{2.1a}$$

$$\nabla \times \tilde{\mathbf{H}} = \tilde{\mathbf{J}} + \frac{\partial \tilde{\mathbf{D}}}{\partial t}, \tag{2.1b}$$

$$\nabla \cdot \tilde{\mathbf{D}} = \rho, \tag{2.1c}$$

$$\nabla \cdot \tilde{\mathbf{B}} = 0, \tag{2.1d}$$

where $\tilde{\mathbf{E}}$ and $\tilde{\mathbf{H}}$ are the electric and magnetic fields, $\tilde{\mathbf{D}}$ is the electric displacement field, $\tilde{\mathbf{B}}$ is the magnetic flux density, and $\tilde{\mathbf{J}}$ and ρ are the free current and charge densities [13]. We use tildes to denote quantities that are rapidly varying in time at an assumed optical carrier frequency, and boldface to denote vectors. The relationships between $\tilde{\mathbf{E}}$ and $\tilde{\mathbf{D}}$ and between $\tilde{\mathbf{H}}$ and $\tilde{\mathbf{B}}$ are given by the constitutive relations, where we assume a nonmagnetic material and separate the polarization response of the medium into linear and nonlinear components $\tilde{\mathbf{P}}_{\mathrm{L}}$ and $\tilde{\mathbf{P}}_{\mathrm{NL}}$. We incorporate the linear component into the electric field via the use of a relative permittivity ϵ_r:

$$\tilde{\mathbf{B}} = \mu_0 \tilde{\mathbf{H}}, \tag{2.2a}$$

$$\tilde{\mathbf{D}} = \epsilon_0 \epsilon_r \tilde{\mathbf{E}} + \tilde{\mathbf{P}}_{\mathrm{NL}}, \tag{2.2b}$$

where $\epsilon_r = 1 + \chi^{(1)} = n^2$ where $\chi^{(1)}$ is the linear susceptibility of the medium an n is the refractive index. Taking the curl of Eq. (2.1a) and using Eq. (2.1b) we obtain

$$\nabla^2 \tilde{\mathbf{E}} + \sigma \mu_0 \frac{\partial \tilde{\mathbf{E}}}{\partial t} + \frac{\epsilon_r}{c^2} \frac{\partial^2 \tilde{\mathbf{E}}}{\partial t^2} = \frac{1}{\epsilon_0 c^2} \frac{\partial^2 \tilde{\mathbf{P}}_{\mathrm{NL}}}{\partial t^2}, \tag{2.3}$$

where we have assumed a source-free medium (i.e. $\rho = 0$), and used the vector identity

$$\nabla \times \left(\nabla \times \tilde{\mathbf{E}}\right) = \nabla \left(\nabla \cdot \tilde{\mathbf{E}}\right) - \nabla^2 \tilde{\mathbf{E}}. \tag{2.4}$$

Neglecting the the $\nabla(\nabla \cdot \tilde{\mathbf{E}})$ component [12], Eq. 2.3 is evidently a driven, damped vector wave equation. Note that we have introduced an effective conductivity σ such that $\tilde{\mathbf{J}} = \sigma \tilde{\mathbf{E}}$, which incorporates the effect of losses.

We will be concerned primarily with nonlinear optical interactions in waveguides, which consist of discrete bound modes and a continuum of radiation modes (which can usually be neglected). We first give a useful factorization of the full electric field of a particular frequency component at ω_j, where the normalizations serve to provide a bridge to the quantum mechanical description in Sec. 2.2. Since the waveguides used in this dissertation are weakly confining and support only a single polarization of light [14], we now drop the vector nature of the electric fields:

$$\tilde{E}_j(x, y, z, t) = \xi_j u_j(x, y) a_j(z) e^{i(\omega_j t - k_j z)}. \tag{2.5}$$

Here, $a_j(z)$ is a slowly varying envelope with units $[|a_j(z)|^2]$ = photons/s, $k_j = \omega_j n_j / c$ is the propagation constant (where n_j is taken to be the effective index of the waveguide mode), and $u_j(x, y)$ is the spatial mode of the waveguide and is normalized such that

$$\iint |u_j(x, y)|^2 \, \mathrm{d}x \, \mathrm{d}y = 1. \tag{2.6}$$

The scale factor $\xi_j = (2Z_j \hbar\omega_j)^{1/2}$, where $Z_j = Z_0/n_j$ where $Z_0 = \sqrt{\mu_0/\epsilon_0} \approx 376.73\ \Omega$ is the impedance of free space, and $\hbar = h/2\pi$ is Planck's constant.

To arrive at coupled wave equations, it is necessary to specify the form of the frequency components of the nonlinear polarization $\tilde{\mathbf{P}}_{\mathrm{NL}}$. For sum-frequency generation, we are interested in the upconversion of a signal at ω_1 via the interaction with a pump at ω_p, producing a target field at $\omega_2 = \omega_1 + \omega_p$. The scalar magnitudes of the nonlinear polarization at these three frequencies are

$$\mathcal{P}_{\mathrm{NL}}(\omega_2) = 2\epsilon_0 d E(\omega_1) E(\omega_p) \tag{2.7a}$$

$$\mathcal{P}_{\mathrm{NL}}(\omega_1) = 2\epsilon_0 d E(\omega_2) E^*(\omega_p) \tag{2.7b}$$

$$\mathcal{P}_{\mathrm{NL}}(\omega_p) = 2\epsilon_0 d E(\omega_2) E^*(\omega_1) \tag{2.7c}$$

where $d = \chi^{(2)}/2$ is the nonlinear coefficient and is a function of position: it has lateral dependence due to the waveguide structure and axial dependence due to quasi-phasematching (QPM, see Sec. 3.1).

Coupled wave equations can be derived by inserting the nonlinear polarization of

Eqs. (2.7) into Eq. (2.3). Inserting the complete electric field (consisting of a sum of the waves at the three frequencies involved in the problem) and using the slowly varying envelope approximation [12], one obtains the following coupled first-order nonlinear differential equations:

$$\left(\frac{\mathrm{d}}{\mathrm{d}z}+\frac{\alpha_1}{2}\right)a_1=-i\kappa a_p^* a_2\, e^{-i\Delta k' z} \tag{2.8a}$$

$$\left(\frac{\mathrm{d}}{\mathrm{d}z}+\frac{\alpha_p}{2}\right)a_p=-i\kappa a_1^* a_2\, e^{-i\Delta k' z} \tag{2.8b}$$

$$\left(\frac{\mathrm{d}}{\mathrm{d}z}+\frac{\alpha_2}{2}\right)a_2=-i\kappa a_1 a_p\, e^{i\Delta k' z}, \tag{2.8c}$$

where $\Delta k' = k_2 - k_p - k_1$ is the phase mismatch, α_j is the power loss coefficient ($j \in \{1,\, p,\, 2\}$), and the coupling coefficient

$$\kappa = \epsilon_0 d \left(\frac{2\hbar\omega_1\omega_p\omega_2 Z_0^3}{n_1 n_p n_2}\right)^{1/2}\Theta. \tag{2.9}$$

Here, n_j is the effective index of the waveguide mode at frequency ω_j, and Θ is the mode-overlap integral in the waveguide, given by

$$\Theta = \iint \bar{d}(x,y)u_1(x,y)u_p(x,y)u_2^*(x,y)\ \mathrm{d}x\ \mathrm{d}y, \tag{2.10}$$

where we have incorporated the spatial form of the nonlinear coefficient $d = d_0\bar{d}(x,y)$, where $\max\left\{\left|\bar{d}(x,y)\right|\right\} = 1$.

As an illustrative example, we shall proceed to solve Eqs. (2.8) for the case $a_1(z=0)=a_{10}$ and $a_2(z=0)=0$, corresponding to the upconversion of a weak signal. We make several simplifying asumptions. First, the input signal a_{10} is much weaker than the pump a_p, such that we assert $a_p(z) = a_p(0)$, i.e. an undepleted pump, and thus can set the right-hand side of Eq. (2.8b) equal to 0. We also consider perfect phasematching, that is, that $\Delta k' \neq 0$ has been corrected by some phase-matching technique (e.g. QPM, see Sec. 3.1), and also that the propagation losses of the waveguide are negligible. This last assertion is not strictly true for the waveguide technology described in Chapter 3, but the low losses of our waveguides do not

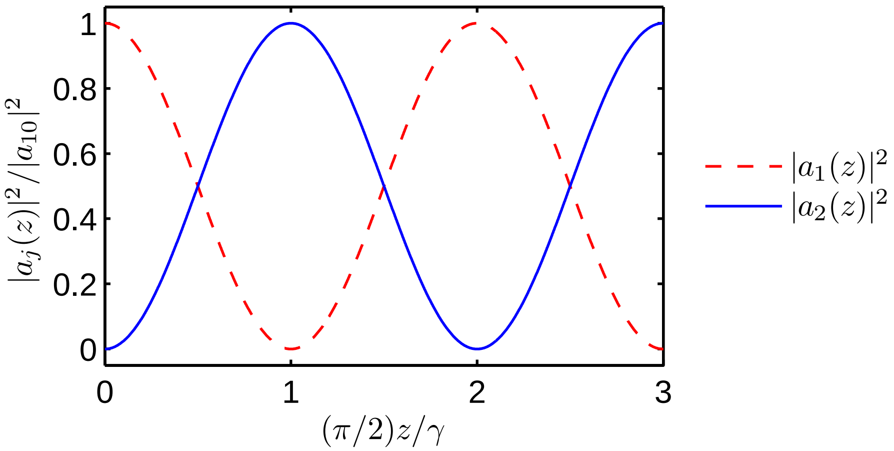

Figure 2.1: Photon flux evolutions $a_1(z)$ and $a_2(z)$ in a classical SFG process where $a_1(0) = a_{10}$, and $a_2(0) = 0$. Complete conversion occurs after a distance $z = \pi/2\gamma$.

substantially change the conversion dynamics but rather only reduce the maximum conversion efficiency. Rewriting Eqs. (2.8) with these assumptions, we have

$$\frac{\mathrm{d}a_1}{\mathrm{d}z} = -\gamma a_2 \tag{2.11a}$$

$$\frac{\mathrm{d}a_2}{\mathrm{d}z} = \gamma a_1 \tag{2.11b}$$

where $\gamma = \kappa A_p$ and we write $a_p = A_p e^{i\phi_p}$ (with A_p real and positive) and have chosen the arbitrary overall phase $\phi_p = \pi/2$. The solution to Eqs. (2.11) proceeds straightforwardly by differentiating Eq. (2.11b) and inserting the equality of Eq. (2.11a), whereby we are led to the solutions

$$a_1(z) = a_{10} \cos \gamma z, \tag{2.12a}$$

$$a_2(z) = a_{10} \sin \gamma z. \tag{2.12b}$$

These solutions are plotted in Fig. 2.1. We see that complete conversion of a signal at ω_1 to ω_2 occurs after a propagation distance of $z = \pi/2\gamma$.

2.2 Quantum frequency conversion

Eqs. (2.12) give the classical solution to the upconversion of a signal at ω_1 by interaction with a pump at ω_p via SFG. One attains a proper quantum mechanical treatment of three-wave interactions via the Hamiltonian of the quantized electric fields in a nonlinear dielectric [15, 16]. This is a subtle process, and is beyond the scope of the dissertation. However, it can be shown, and all experimental observations have verified, that Eqs. (2.11) give the proper quantum mechanical description if the field envelopes a_1 and a_2 are replaced with the annihilation operators $\hat{a}_1$ and $\hat{a}_2$ of photons at frequencies ω_1 and ω_2. The operator $\hat{a}_1$ ($\hat{a}_1^\dagger$) annihilates (creates) one photon at frequency ω_1. These operators obey the commutation relations $[\hat{a}_j, \hat{a}_k^\dagger] = \delta_{jk}$, where δ_{jk} is the Kronecker delta, and have the properties

$$\hat{a}|n\rangle = \sqrt{n}|n-1\rangle, \tag{2.13a}$$

$$\hat{a}^\dagger|n\rangle = \sqrt{n+1}|n+1\rangle, \tag{2.13b}$$

where $|n\rangle$ is the Fock (photon-number) state containing n photons, and $\hat{a}|0\rangle = 0$ [17].

Here, we present the input–output relation (after propagation over a distance L corresponding to the length of the device) for the annihilation operators $\hat{a}_1$ and $\hat{a}_2$ as the two fields exchange photons through the conversion process. A quantum-mechanically accurate version, unlike the results of Eqs. (2.12), must include both input operators such that the effects of vacuum fluctuations are included. Working in the Heisenberg picture (whereby the operators evolve in time but the quantum state does not), this input–output relation is given by

$$\hat{a}_1(L) = \hat{a}_1(0)\cos\gamma L + \hat{a}_2(0)\sin\gamma L, \tag{2.14a}$$

$$\hat{a}_2(L) = -\hat{a}_1(0)\sin\gamma L + \hat{a}_2(0)\cos\gamma L. \tag{2.14b}$$

We see, evidently, that if $\gamma L = \pi/2$, up to an arbitrary overall phase factor the annihilation operators have switched places [6]

$$\hat{a}_1(0) \Rightarrow -\hat{a}_2(L) \qquad \text{and} \qquad \hat{a}_2(0) \Rightarrow \hat{a}_1(L). \tag{2.15}$$

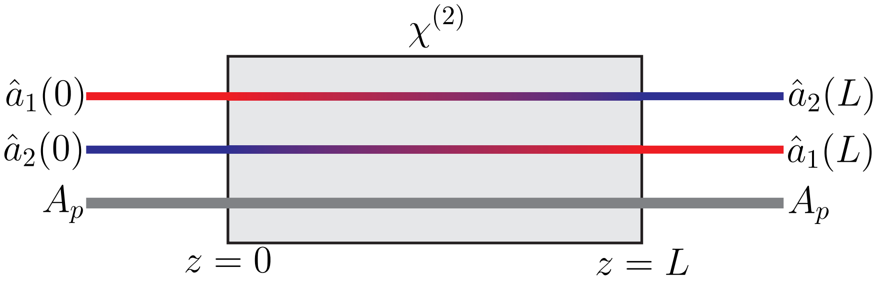

Figure 2.2: Schematic diagram of the quantum frequency conversion process in a $\chi^{(2)}$ material. A quantum state of light at ω_1 (ω_2) is upconverted (downconverted) to ω_2 (ω_1) via interaction with a pump field at ω_p, where $\omega_1 + \omega_p = \omega_2$.

Eq. (2.15) captures the concept of the quantum frequency converter, which is shown schematically in Fig. 2.2. Through interaction with a strong pump, if the device length and pump power are chosen such that $\gamma L = \pi/2$, the annihilation operators for photons at the input and output have swapped frequencies. Importantly, this means that the quantum frequency converter is capable of simultaneously upconverting and downconverting two input quantum states. In most experimental implementations, one of the input states will be a vacuum state. However, based on the similarity of Eqs. (2.14) to a beamsplitter input–output relation [18], there is a proposal to use the quantum frequency converter as a method by which one could interfere two photons of different color [19].

We consider one example of the effects of quantum frequency conversion on an input quantum state, and calculate the conversion efficiency of a signal at ω_1 to a target at ω_2. We consider an input state $|\psi\rangle = |n_1\rangle_{\omega_1}|0\rangle_{\omega_2} \equiv |n_1\,0\rangle$. We calculate the conversion efficiency as the ratio of photon number at the target frequency at the output of the device to the photon number at the signal frequency at the input of the device:

$$\eta \equiv \frac{\langle\psi|\hat{n}_2(L)|\psi\rangle}{\langle\psi|\hat{n}_1(0)|\psi\rangle} = \frac{\langle\psi|\hat{a}_2^\dagger(L)\hat{a}_2(L)|\psi\rangle}{\langle\psi|\hat{a}_1^\dagger(0)\hat{a}_1(0)|\psi\rangle} \tag{2.16a}$$

$$= \sin^2 \gamma L \tag{2.16b}$$

where the result of Eq. (2.16b) is due to applying Eqs. (2.14) and (2.13) to Eq. (2.16a).

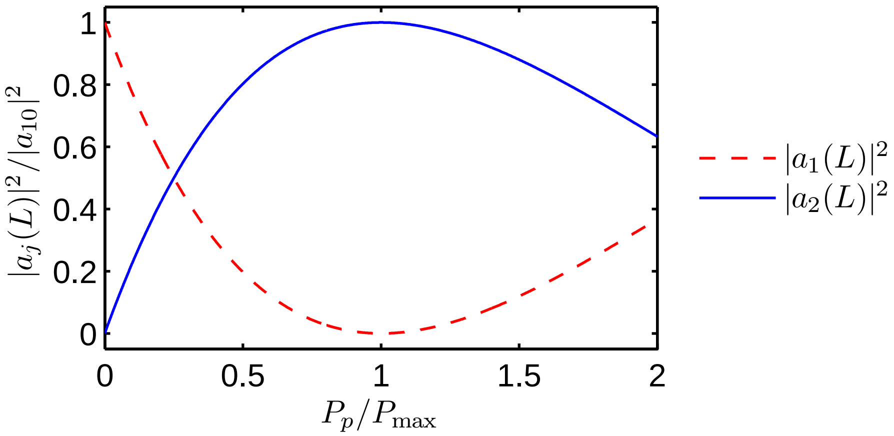

Figure 2.3: Conversion efficiency η versus normalized pump power $P_p/P_{\max}$ for a SFG process, where $P_{\max} = \pi^2/(4L^2\eta_{\text{nor}})$, as given in Eq. (2.19). Note that this result is the same as is obtained for the classical case of Eqs. (2.12).

These results are also evident classically from Eqs. (2.12). Generalizing further, we note that for a general state $|\psi_{12}\rangle$, quantum properties of the two modes are determined by $\langle \hat{f}_1 \rangle = \langle \psi_{12} | \hat{f}_1(\hat{a}_1) | \psi_{12} \rangle$, and $\langle \hat{f}_2 \rangle = \langle \psi_{12} | \hat{f}_2(\hat{a}_2) | \psi_{12} \rangle$ where $\hat{f}_1$ ($\hat{f}_2$) is a generic function of the annihilation operator $\hat{a}_1$ ($\hat{a}_2$). Therefore, for $\gamma L = \pi/2$, when Eq. (2.15) holds, we have

$$\langle \hat{f}_1(z = L) \rangle = \langle \psi_{12} | \hat{f}_1[\hat{a}_2(0)] | \psi_{12} \rangle \tag{2.17a}$$

$$\langle \hat{f}_2(z = L) \rangle = \langle \psi_{12} | \hat{f}_2[-\hat{a}_1(0)] | \psi_{12} \rangle . \tag{2.17b}$$

We see, therefore, that the quantum properties of the mode $\hat{a}_1$ ($\hat{a}_2$) at the device output are determined by the input mode $\hat{a}_2$ ($\hat{a}_1$) for a complete quantum frequency conversion process [6].

It is worthwhile to express the conversion efficiency of Eq. (2.16) and the coupling coefficient γ in terms of experimental parameters and physical constants. Recalling that $\gamma = \kappa A_p$, where κ is given by Eq. (2.9) and using the field definitions of Eq. (2.5), we define a normalized efficiency of the device η_{nor} by equating $\gamma = \sqrt{\eta_{\text{nor}} P_p}$, where

P_p is the pump power. Using this definition, we find that

$$\eta_{\text{nor}} = \epsilon_0^2 d_0^2 |\Theta|^2 \frac{2\omega_1 \omega_2 Z_0^3}{n_1 n_2 n_3}. \tag{2.18}$$

As the main experimental parameter once a device is fabricated is the pump power, we plot the conversion efficiency η as a function of P_p,

$$\eta = \sin^2\left(\sqrt{\eta_{\text{nor}} P_p} L\right) = \sin^2\left(\frac{\pi}{2}\sqrt{\frac{P_p}{P_{\text{max}}}}\right), \tag{2.19}$$

in Fig. 2.3, where we have defined P_{max} as the pump power requried for complete conversion, given by $P_{\text{max}} = \pi^2/(4L^2\eta_{\text{nor}})$. For pump powers larger than P_{max}, back-conversion reduces the conversion efficiency.

2.3 Historical overview

Quantum frequency was first proposed by Prem Kumar in 1990, who showed theoretically that the properties of a quantum state of light are unchanged upon frequency conversion in a $\chi^{(2)}$ material [6]. The first experimental demonstration of QFC followed in 1992, where Kumar's group was able to upconvert a squeezed state from 1064 nm to 532 nm, and it was proposed that QFC can provide a wavelength-tunable source of nonclassical light [7]. In this initial demonstration, the nonlinear medium was a bulk KTP crystal; due to the low nonlinearity it was necessary to use a Q-switched mode-locked Nd:YAG laser to achieve appreciable conversion efficiencies.

Following this demonstration, it seems that QFC was not actively pursued for several years. A resurgence of interest followed the development of entangled photon sources based on spontaneous parametric downconversion (SPDC) in $\chi^{(2)}$ crystals, which provided a much more convenient source of nonclassical light than the atomic physics techniques which had been used before that time [20]. Additionally, following the development of experimental quantum cryptography [21], it was realized that the limiting factor for system performance was the relatively poor single-photon detectors for telecom-band photons [22]. Vandevender and Kwiat developed a telecom single-photon detector based on quantum frequency upconversion of the telecom-band photons, followed by detection with a higher-performance Si APD single-photon detector [23]. Again, short pump pulses (a few ns, at $\lambda_p = 1064$ nm) were needed due the use of a bulk crystal, but here the use of PPLN enabled 80% conversion efficiency although at a peak power level of 12 kW.

We note, however, that, dating to the earliest days of nonlinear optics, upconversion was proposed as a technique to improve infrared detector technology [11]. In the late 1960s, Midwinter demonstrated upconversion of both optical signals [10] and images [24] at 1.7 μm to the visible using a ruby laser as a pump. While it was realized that upconversion occurs on a photon-by-photon basis, the implications for quantum optics were not yet realized: a reasonably comprehensive theory of quantum optics had only recently been developed by Glauber [25]. In the first experiment, conversion efficiencies of approximately 1% were achieved, using a LiNbO_3 crystal using noncritical birefringent phasematching [12]. Upconversion techniques were later extended further into the infrared for use in astronomy [26]. In both of the image upconversion experiments mentioned here, the conversion efficiences were limited to approximately 10^{-7}. We note that there has been a recent theoretical proposal on the frequency upconversion of a *quantum* image, a state of light in which there are quantum correlations between the various spatial modes comprising the state [27].

The first demonstrations of continuous-wave upconversion for single-photon detection were based on a RPE PPLN waveguide [28], or a bulk PPLN crystal placed in a pump-resonant cavity [29]. In the resonant cavity of Albota and Wong, up to 90% conversion efficiency was observed for a circulating pump power of 21.6 W. Roussev and coworkers observed a signal depletion level of 99%, with overall conversion efficiency limited to 82% due to waveguide losses of approximately 0.18 dB/cm. The waveguide used was of the RPE type that will be described in the following chapter, and had $P_{\max} = 88$ mW, approximately 350 times lower than for the bulk PPLN device of [29].

A common issue in the first generation of quantum frequency upconverters was a very high level of noise photons. As an extremely large flux of pump photons is required to obtain efficient conversion, even very weak spontaneous inelastic scattering processes can significantly reduce the system performance. The two spontaneous scattering processes responsible for noise in QFC devices are SPDC [23, 29] and spontaneous Raman scattering [30]. In fact, even in the early upconversion papers it was found that noise processes were a significant limiter of the system performance [10]. In Chapter 4 we present a detailed discussion of these noise processes, which had not been studied in detail until this work. However, it was realized that the use of a pump frequency $\omega_p < \omega_1$ is highly effective at reducing the noise, as it becomes difficult for photons scattered from the strong pump to overlap spectrally with the acceptance bandwidth of the converter near ω_1. Two low-noise upconversion detectors demonstrated this fact, one for the 1-μm band [31], and a second for the 1.55-μm telecom band [32].

To date, upconversion has been used to bring significant added functionality to quantum optics and quantum information systems. Low-jitter upconversion detectors were developed, which were useful in QKD systems [33, 34]. In a pioneering experiment, Tanzilli and collaborators showed that if the signal photon of an entangled photon pair was upconverted, its entanglement (using the time-bin variable) with the idler photon was preserved [35]. Recently, polarization entanglement was also shown to be preserved [36]. Two additional concepts of technological importance were the use of the combination of the narrow acceptance bandwidth of the upconverter with a tunable pump frequency to enable a single-pixel upconversion spectrometer [37], and the demonstration of high-dynamic-range time-domain reflectometry for characterizing fiber optic links [38]. Recently, interfaces of quantum frequency upconverters with a 1.3-μm quantum dot single-photon source were demonstrated, showing the preservation of photon antibunching upon upconversion [39], and temporal shaping by modulation of the pump waveform [40]. Additionally, it has been shown the phase coherence of a quantum state is preserved [41] and that photon statistics (up to fourth order) are preserved upon upconversion [42].

While the bulk of experimental work on QFC has focused on upconversion, it was realized early on that downconversion of quantum states of light is also possible. As was discussed in Chapter 1, downconversion represents a critical functionality needed to connect quantum nodes with transitions in the visible or near-visible spectral region with the telecom band, allowing long-distance quantum communication over optical fiber. This application is in contrast to a naïve view of "downconversion" as a process that involves the amplification of quantum noise [43]. Rather, in a single-photon downconverter, the single-photon is at the highest frequency and the strong pump driving the conversion is at a lower frequency[1], such that the resulting OPA has negligible gain, and therefore negligible noise (but of course subject to the same constraints of parasitic spontaneous scattering processes as apply in upconversion devices). A theoretical discussion of single-photon downconversion was presented by Z. Y. Ou in 2008 [44], where it was shown that QFC enables frequency translation of quantum states and the storage of photonic states in stationary matter-based quantum memories. A number of single-photon downconversion experiments followed in the next three years [45, 46, 47, 48, 49]. These experiments have shown preserved coherence in interference experiments, and have also demonstrated high conversion efficiencies. In a recent experiment, entanglement properties have also been shown to be preserved upon downconversion, as was done by Tanzilli in upconversion [50]. This dissertation presents the first demonstration of a downconversion interface to a solid-state qubit system, which is expected to be of interest for quantum communication based on quantum repeaters [51].

While this dissertation focuses on quantum frequency conversion in $\chi^{(2)}$ media, there have been recent proposals and a few experimental demonstrations using four-wave mixing in $\chi^{(3)}$ media. In one such implementation, known as Bragg scattering, two pumps at ω_{p1} and ω_{p2} are used to convert a signal at ω_1 to targets at $\omega_{2\pm} = \omega_1 \pm (\omega_{p1} - \omega_{p2})$, although phasematching can be used to preferentially create ω_{2+} or ω_{2-} [52]. Since one signal photon and one pump photon are destroyed as a target photon and a second pump photon are created, this process, similar to SFG and single-photon DFG, should also be noiseless. The first experimental demonstration of Bragg scattering for a weak signal was done in 2006, and a signal depletion of 22 dB was observed, with a large amount of noise (on single-photon scales, but moderate on classical telecommunications scales) due to Raman scattering as all signals were in the

---

[1] In this dissertation, we always use the term "pump" to refer to the field driving the conversion process, in contrast with optical parametric amplification (OPA) terminology.

1.5-μm telecom band [53]. Demonstration of QFC with $\chi^{(3)}$ processes was achieved using a photonic crystal fiber, with depletion efficiencies of 29% [54]. The use of two pumps makes the $\chi^{(3)}$ QFC techniques attractive for frequency translation between nearby frequencies where a $\chi^{(2)}$ technique would require extremely low ω_p. However, it should be noted that implementations of $\chi^{(3)}$-based QFC techniques have suffered a great deal from noise photons primarily due to spontaneous Raman scattering.

Chapter 3

Reverse-proton-exchange waveguides in periodically poled lithium niobate

The results presented in this dissertation rely heavily on the performing optical frequency conversion with high efficiency. Optical nonlinearities are famously extremely weak [11], and it is only recently that researchers have been able to attain the conversion efficiencies necessary for the realistic implementation of frequency conversion at the single- or few-photon level [23, 28, 29].

The device platform used in this work is based on annealed and reverse proton exchange (RPE) waveguides in periodically poled lithium niobate (PPLN) [55]. The development of sophisticated materials and process models by previous generations of Fejer-group students has enabled a reliable technique where devices can be designed for any application of interest [56]. In the next section, we describe the theory and practice of quasi-phasematching by periodic poling. In Sec. 3.2, we discuss the fabrication process used for making RPE waveguides, and discuss the "toolbox" of waveguide components that enables the applications discussed in following chapters. In Sec. 3.3 we outline the characterization procedures by which fabricated devices are screened for performance, and describe the fiber-pigtailing technique by which the devices can be integrated into fiber-based quantum optical systems.

3.1 Quasi-phasematching and periodic poling

For the work in this dissertation we are primarily concerned with high-efficiency sum- or difference-frequency generation processes. Eqs. (2.8) gave the coupled wave equations for an SFG process in which a target field at ω_2 was generated from a signal ω_1 and pump ω_p, where $\omega_2 = \omega_1 + \omega_p$. Neglecting propagation losses, the growth of the field at the sum-frequency (SF) is given by

$$\frac{\mathrm{d}a_2}{\mathrm{d}z} = \Gamma d_0 a_1 a_p \, e^{i\Delta k z}, \tag{3.1}$$

where the $\Gamma = i\kappa/d_0$, with κ given by Eq. (2.9), and the phase mismatch $\Delta k' = k_2 - k_1 - k_p$, where $k_j = \omega_j n(\omega_j)/c$ is the wave vector at frequency $j \in \{p, 1, 2\}$. Due to dispersion, the quantity Δk will in general be nonzero. In the limit of low conversion where $a_1(z) = a_1(0)$ and $a_p(z) = a_p(0)$, the evolution of $a_2(z)$ will thus be governed by the rotation of the complex exponential $\exp(i\Delta k' z)$, causing oscillations in the power $P_2(z) = \hbar\omega_2 |a_2(z)|^2$, with periodic reversals in power flow occurring every coherence length $L_c = \pi/\Delta k'$. The earliest demonstrations of nonlinear frequency conversion operated in this phase-mismatched regime, and as such were unable to attain appreciable conversion efficiencies [8].

Until quasi-phasematching (QPM) was developed, achieving phasematching of nonlinear optical interactions was a matter of finding materials with suitable birefringence for the interaction of interest. Many non-centrosymmetric crystals suitable for $\chi^{(2)}$ nonlinear optics also have linear-optical anisotropy: the refractive index varies as the orientations of the polarization and propagation direction are changed with respect to the crystalline axes. In some circumstances, it is possible to choose the polarizations and **k**-vectors of interacting waves such that $\Delta k' = 0$, enabling a phase-matched interaction. This technique is known as birefringent phasematching, and enables quadratic growth of power with propagation distance, as is shown by the green curve in Fig. 3.1.

In the case of $\mathrm{LiNbO_3}$, the largest nonlinear coefficient (by approximately a factor of 6) involves the interaction of three waves polarized along the crystalline z-axis , and is therefore not compatible with birefringent phasematching [12]. The technique of

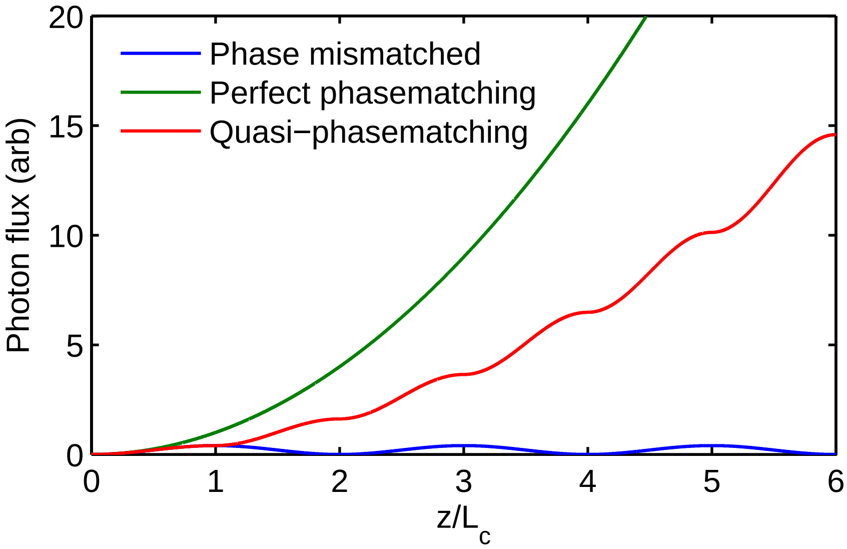

Figure 3.1: Intensity evolution of generated sum-frequency radiation for three different phasematching conditions.

quasi-phase-matching, introduced by Armstrong and Bloembergen in 1962, involves a periodic modulation of the sign of the $\chi^{(2)}$ throughout the medium [11]. Allowing the nonlinear coefficient to include a spatial dependence $d(z)$, we find that the SF field at the output of the medium is given by an integration of Eq. (3.1):

$$a_2(L) = \Gamma a_1(0) a_p(0) \int_0^L d(z)\, e^{-i\,\Delta k'\, z}\, \mathrm{d}z, \tag{3.2}$$

which (assuming the $d(z)$ is only nonzero on the range $[0,\ L]$) is the Fourier transform of $d(z)$. For periodic modulation with period Λ, $d(z)$ can be constructed as a Fourier series:

$$d(z) = d_0 \sum_{m=-\infty}^{\infty} G_m e^{iK_m z}, \tag{3.3}$$

where $K_m = 2\pi m/\Lambda$. In the case of periodic poling, $d(z)$ takes the values $\pm d_0$ alternating in a square wave fashion with duty cycle D. The Fourier coefficients have the values

$$G_m = \frac{2}{m\pi} \sin m\pi D \tag{3.4}$$

Incorporating the form of Eqs. (3.3) and (3.4) into the integral in Eq. (3.2), in the case where K_m is close to $\Delta k'$, the integral is dominated by the mth term of the summation in Eq. (3.3), and thus

$$a_2(L) = \Gamma d_m a_1(0) a_p(0) e^{i\Delta kL/2} \operatorname{sinc}\left(\frac{\Delta kL}{2}\right) \tag{3.5}$$

where $d_m = d_0 G_m \equiv d_{\text{eff}}$ is the amplitude of the utilized harmonic of the square wave modulation, and $\Delta k = \Delta k' - K_m$ [57].

From Eq. (3.5), we see that the behavior of a QPM interaction is the same as that of a birefringently phasematched interaction but where the effective phase mismatch has been shifted by an amount K_m, and the nonlinear coefficient d has been replaced by d_m. For first-order ($m = 1$) QPM, d_1 is maximized for a 50/50 duty cycle $D = 0.5$, in which case $d_1 = (2/\pi)d_0$. This case corresponds to a reorientation of d every coherence length $L_c = \pi/\Delta k'$. We can calculate the power growth of the SF field by a direct integration of Eq. (3.2). The power growth for this case where $\Delta k = 0$ is plotted as the solid red curve in Fig. 3.1, where we see, on coarse spatial scales, a quadratic growth of the field as the phase is reset every coherence length. The normalized, or small-signal, efficiency of the QPM process compared with a birefringently phasematched interaction is reduced by a factor $\eta_{\text{QPM}}/\eta_{\text{BPM}} = (2/\pi)^2 \approx 41\%$. For LiNbO_3, the use of quasi-phase-matching enables the use of the $d_{33} = 27$ pm/V nonlinear coefficient, which allows for frequency conversion with efficiencies approximately 16 times larger than for interactions using the largest birefringently phasematcheable nonlinear coefficient $d_{31} = 4.1$ pm/V [12].

Several techniques have been utilized to achieve quasi-phase-matching in nonlinear optical materials, including stack-of-plates methods [58], orientation-patterned semiconductors [59], and periodically poled ferroelectrics [60]. The work described in this dissertation takes advantage of electric-field poling techniques [61]. Lithium niobate, the material of choice for the work of this dissertation, is a ferroelectric material and thus has a spontaneous electric dipole moment. Applying an electric field pulse above the coercive field of the material can reorient the crystal structure and change the sign of the d_{33} nonlinear coefficient. The dynamics of the electric-field poling process

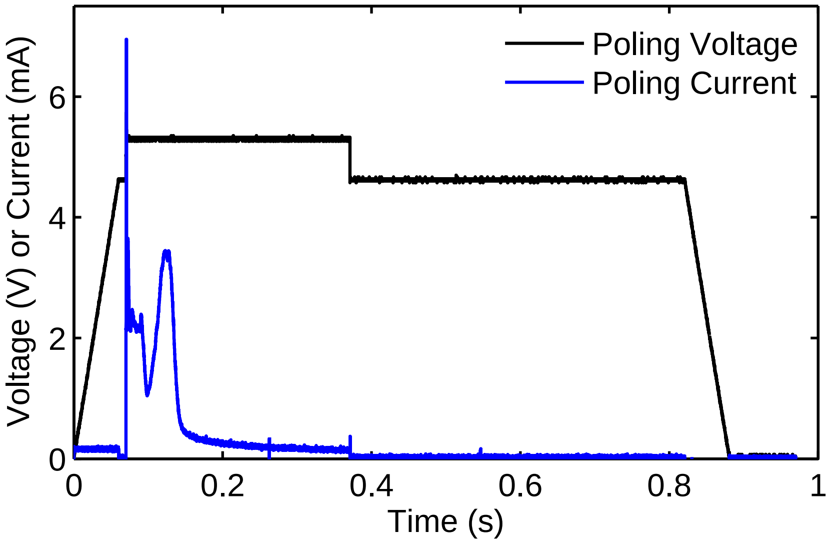

Figure 3.2: Typical voltage and current waveforms during whole-wafer electric-field periodic poling.

have been studied in detail [62]. By patterning the surface of the material, electric-field poling enables a structuring of the volume of the medium. Inverted domains propagate from the $+z$ to $-z$ surface of the wafer, and can be poled with an aspect ratio (domain height):(domain width) exceeding 100:1.

The poling procedure we use is outlined schematically in Fig. 3.3. We pattern the $+z$ surface of a 0.5-mm-thick, 72.6-mm-diameter congruent-composition $LiNbO_3$ wafer. A thick layer (approximately 3 to 5 μm) of photoresist is spun onto the wafer surface. Electrodes are patterned via UV illumination through a photolithographic mask followed by developing the pattern in LDD-26W developer solution. As electrical contact to the wafer will be made through a liquid electrolyte (saturated solution of lithium chloride in water), the photoresist layer (used as an insulator) is hard-baked onto the wafer. Metal electrodes, while used in initial poling experiments [63], are not used here as it has been found that it is difficult to remove all traces of metal from the wafer surface, which is necessary here as waveguides are formed very close to the $+z$ surface. The wafer is placed into an electrical circuit where the $+z$ surface receives a high-voltage pulse created using a function generator followed by a Trek

×2000 high-voltage amplifier, and the $-z$ surface is connected to ground through a 1 kΩ resistor. Poling requires electric fields exceeding the the $\mathrm{LiNbO_3}$ coercive field of 21 kV/mm, which for the 0.5-mm-thick samples indicates a voltage of 10.5 kV. The voltage across the 1 kΩ resistor is monitored, giving a measurement of the poling current. The applied voltage pulse (measured by the output monitor of the amplifier) is shown in black in Fig. 3.2, and consists of a ramp up to a field level slightly below the coercive field, a voltage spike above the coercive field to aid in nucleation of inverted domains, and a voltage hold at a level slightly above the coercive field. As is seen in Fig. 3.2, once the domains start to nucleate, current begins to flow through the wafer as the ferroelectric domains reorient. Poling is done in the self-terminating regime, whereby the growth of domain walls is stopped at a certain duty cycle D determined by the poling initial conditions [64]. We have found that poling quality (uniformity of domain pattern) is highest under self-terminating conditions. Unlike previous work [55], in which the poling current $I(t)$ was limited by the amplifier's current limit of 20 mA, in Fig. 3.2 we see current levels in the range of a few mA so the amplifier is still in the linear regime. When one designs a photolithographic mask for poling, one can calculate the expected area A_{pol} to be poled, which in turn be related to the total charge Q transported through the wafer as

$$A_{\text{pol}} = \frac{Q}{P_{\text{sp}}} = \frac{1}{P_{\text{sp}}} \int_0^T I(t)\ \mathrm{d}t \tag{3.6}$$

where $P_{\text{sp}} = 78\ \mu\mathrm{C\ cm^{-2}}$ is the spontaneous polarization charge density associated with the spontaneous dipole moment in $\mathrm{LiNbO_3}$ [55]. For various projects throughout this dissertation, we have poled a range of periods between 7 and 25 μm using these techniques, sometimes even within the same waveguide [65].

3.2 Fabrication of RPE waveguides

Nonlinear optical interactions can be performed most efficiently when the interacting fields are confined to a small area, hence high intensity and high field strength, over

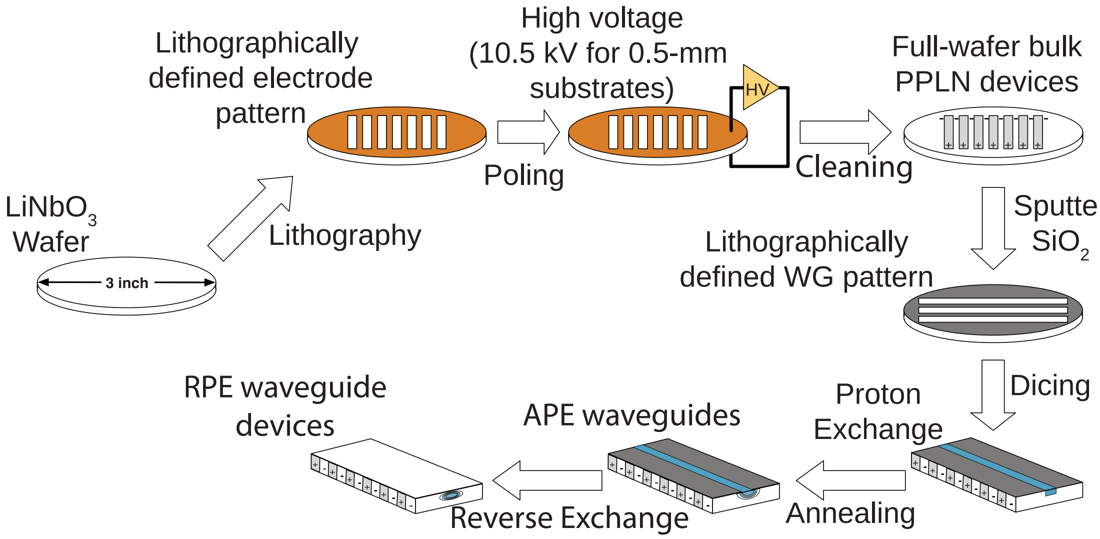
Lithographically defined electrode pattern
High voltage (10.5 kV for 0.5-mm substrates)
HV
Full-wafer bulk PPLN devices
Poling
Cleaning
LiNbO3 Wafer
3 inch
Lithography
Sputter SiO2
Lithographically defined WG pattern
Dicing
RPE waveguide devices
APE waveguides
Proton Exchange
Reverse Exchange
Annealing

Figure 3.3: Process flow for fabrication of RPE PPLN waveguides.

long distances. Performing frequency conversion in waveguides has two distinct advantages. (1) In bulk nonlinear optical media, diffraction sets limits on the minimum spot size for a given interaction length; an analysis of coupled-wave interactions with focused Gaussian beams indicates an optimum efficiency for near-confocal focusing [66]. Therefore, for bulk interactions, the area of an optimally focused beam is proportional to the length of the crystal, so the conversion efficiency η increases only linearly with sample length. (2) In waveguides, the interactions involve discrete eigenmodes of the structure. For bulk interactions, conversion efficiency is a function of intensity and therefore varies across a beam profile, making it difficult to attain near unity conversion efficiencies, while for waveguides, an entire mode converts as a single entity. This aspect of nonlinear interactions in waveguides has enabled extremely high signal depletions in SFG, at the level of 41 dB [67], a level only achievable with very large pump beams in bulk devices which therefore have a very large value of P_{max} for complete conversion.

There are several techniques for forming waveguides in PPLN, including Ti indiffusion [68], mechanical ridge waveguides [69], and annealed proton exchange (APE) waveguides [70]. In this work we have focused on annealed and reverse proton exchange (RPE) waveguides [71], which have substantially lower propagation losses and higher mode-overlap integrals than APE waveguides, making them the platform of choice for applications where high throughput and conversion efficiency are essential.

Following preparation of PPLN wafers via the procedure outlined in Sec. 3.1, we form annealed and reverse proton exchange waveguides via the steps diagrammed schematically in Fig. 3.3. RF sputtering of an 80 nm SiO_2 layer followed by a second photolithography step is used to create channels through which protons enter the substrate. Following the lithography and development of the masking pattern, channels are etched in the SiO_2 mask using a 20:1 buffered-oxide wet etch. We use molten benzoic acid, buffered with approximately 5 wt % lithium benzoate, at a temperature of between 170 and 180° C, as a proton source. Following proton exchange, samples are annealed in air at 310° C for a typical duration of 22.5 hrs. Following removal of the SiO_2 mask, reverse exchange, by which protons are removed from the material and exchanged with lithium ions, is done in a eutectic melt of $LiNO_3/NaNO_3/KNO_3$, at temperatures of approximately 300° C. The proton dose may be measured *in situ* via absorption spectrophotometry of an O–H absorption resonance at a wavelength of 2.85 μm. A detailed model of the concentration-dependent nonlinear diffusion of protons in $LiNbO_3$ has been carried out in the dissertation work of Roussev [56]. Combining the diffusion model with a model for the dispersion of $H_xLi_{1-x}NbO_3$ and a 2D waveguide eigenmode solver has enabled a platform via which critical design parameters may be simulated.

The existence of a fabrication model has enabled accurate prediction of linear and nonlinear optical properties of RPE PPLN waveguides, enabling the inclusion of complex integrated optical structures such as directional couplers, tight-radius bends, and mode multiplexers and demultiplexers. For most of the experiments described in this dissertation, the waveguides used have schematic designs as shown in Fig. 3.4.

At the input of the device is a mode filter, a single-mode waveguide in which the mode shape is generally designed to closely match that of an optical fiber used for input coupling. As RPE waveguides and optical fibers have approximately the same core-cladding index contrast, it is possible to achieve spatial mode matching of approximately 90%. For RPE PPLN waveguides, there exists a noncritical waveguide width for which the QPM wavelength is first-order insensitive to waveguide width

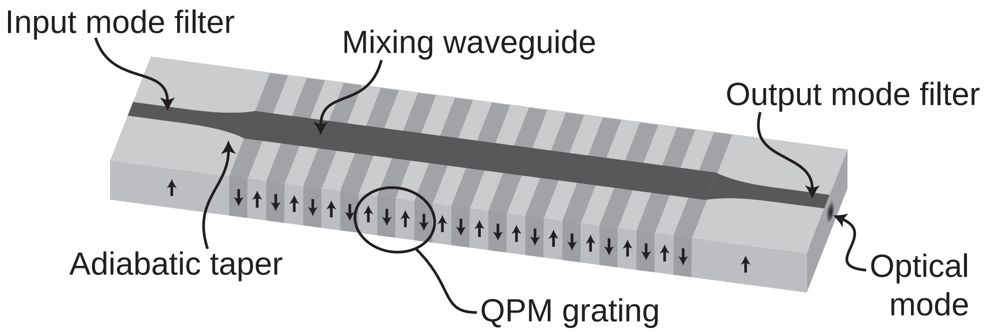

Figure 3.4: Schematic of an RPE PPLN waveguide.

variations [72]. The width of the mixing waveguide is chosen to be noncritical for the interaction of interest, and typically occurs for channel widths between 7 and 9 μm. The mode filter therefore serves a second purpose; the adiabatic taper converts the fundamental (TM_{00}) spatial mode of the mode filter to the TM_{00} mode of the mixing waveguide, such that all of the power in the input signal can participate in the conversion process. At the output of the device, an additional adiabatic taper and mode filter can be included to enable high-efficiency outcoupling into another optical fiber.

3.3 Device characterization and packaging

In this section we describe the techniques by which RPE PPLN waveguides are characterized and prepared for use in systems experiments. A typical waveguide chip is 5.9 mm wide, and contains approximately 100 candidate waveguides spaced by 50 μm. A processing run consisting of devices from two $LiNbO_3$ wafers can therefore entail over 1500 individual waveguides to test. Therefore, a screening process is important to select the best-performing waveguide for a particular application.

3.3.1 Loss Measurements

The first method by which waveguides are screened is a measurement of waveguide propagation loss. For frequency conversion of single photons, high device throughput is of paramount importance. We typically measure propagation loss via the Fabry-Perot technique [73]. A single-spatial-mode waveguide with uncoated facets with transmittivity T polished orthogonal to the waveguide forms a monomode low-finesse Fabry-Perot resonator. The transmitted power P_T through the waveguide is given by

$$P_T = \frac{T^2 e^{-\alpha L}}{\left(1-\tilde{R}\right)^2 + R\tilde{R}\sin^2\left(\phi/2\right)} P_0 \eta_c \tag{3.7}$$

where P_0 is the input power, η_c is the input coupling efficiency, and $\phi = 2\beta L$ is the round-trip phase accumulation, where β the propagation constant and L is the total device length, and $\tilde{R} = R\exp(-\alpha L)$. If one has knowledge of the facet reflectivity R, by measuring the contrast ratio

$$K = \frac{P_{\text{max}} - P_{\text{min}}}{P_{\text{max}} + P_{\text{min}}}, \tag{3.8}$$

a function only of $\tilde{R}$, one can determine the propagation loss α. Combining Eqns. (3.7) and (3.8) yields

$$\tilde{R} = \frac{1}{K}\left(1 - \sqrt{1-K^2}\right). \tag{3.9}$$

For weakly confining waveguides, the mode reflectivity is found using the effective index of the mode n_{eff} as $R = (n_{\text{eff}}-1)^2/(n_{\text{eff}}+1)^2$. For RPE waveguides in LiNbO_3, $R \approx 0.1324$ for $\lambda = 1.55$ μm. The propagation loss α, measured in dB cm^{-1} is then found as

$$\alpha = \frac{4.34}{L}\left(\ln R - \ln \tilde{R}\right). \tag{3.10}$$

We generally have measured propagation losses in the 1.55-μm telecom band. By sweeping the wavelength of a tunable single-frequency laser, the propagation phase ϕ can be varied continuously. For a typical device of length $L = 5.2$ cm, the free spectral range of the Fabry-Perot cavity is $\Delta f = 1.3$ GHz, corresponding to a wavelength range $\Delta\lambda = 11$ pm. A sample transmission curve versus wavelength is shown in Fig. 3.5, where we observe interference fringes with average contrast ratio $K = 0.243$, corresponding to a propagation loss of 0.09 dB/cm. The best waveguides typically have propagation losses in the range 0.05 to 0.1 dB/cm, although on an individual

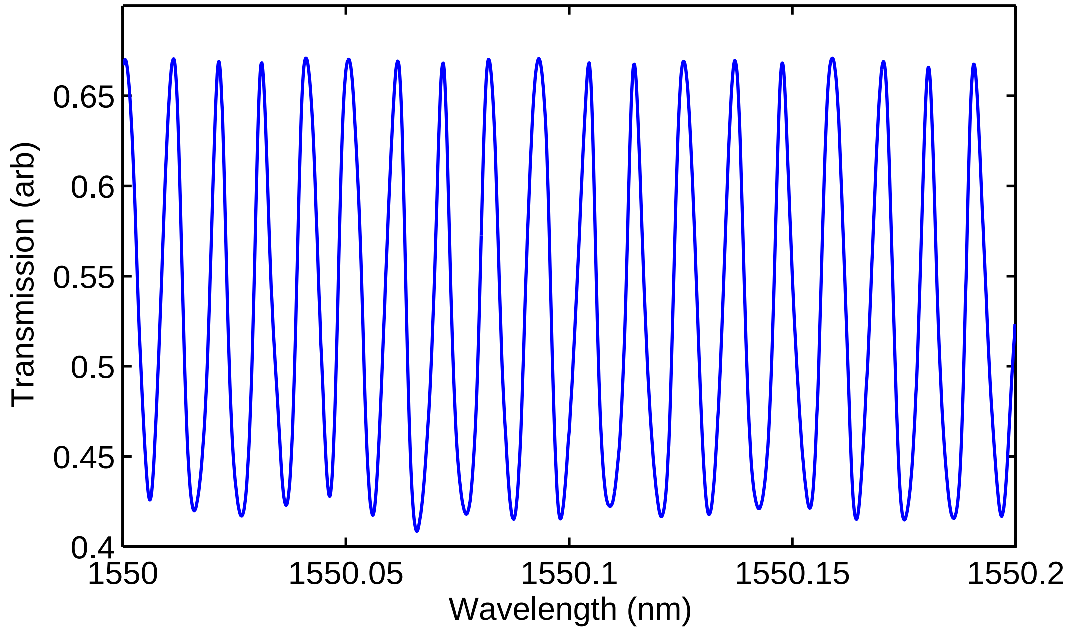

Figure 3.5: Transmission vs. wavelength for a 5.2-cm RPE PPLN waveguide. The observed fringe contrast of 0.243 corresponds to a propagation loss $\alpha = 0.09$ dB cm^{-1}.

chip it is not uncommon to find a large variation in waveguide quality, which can often be traced back to lithographic defects, or to scratches on the facet formed during polishing. We note that the expected error in loss $|\Delta\alpha|$ can be calculated from Eq. (3.7) by the techniques of error propagation [74] as

$$|\Delta\alpha| = \frac{4.34}{L}\frac{|\Delta K|}{K} \tag{3.11}$$

For our cases, we have fractional uncertainty in the contrast $|\Delta K|/K \approx 2\%$, which implies a value $|\Delta\alpha| \approx 0.02$ dB/cm. For accurate loss measurements, one must be careful that the any detector dark voltage or signal due to stray light is subtracted off before calculating the contrast ratio.

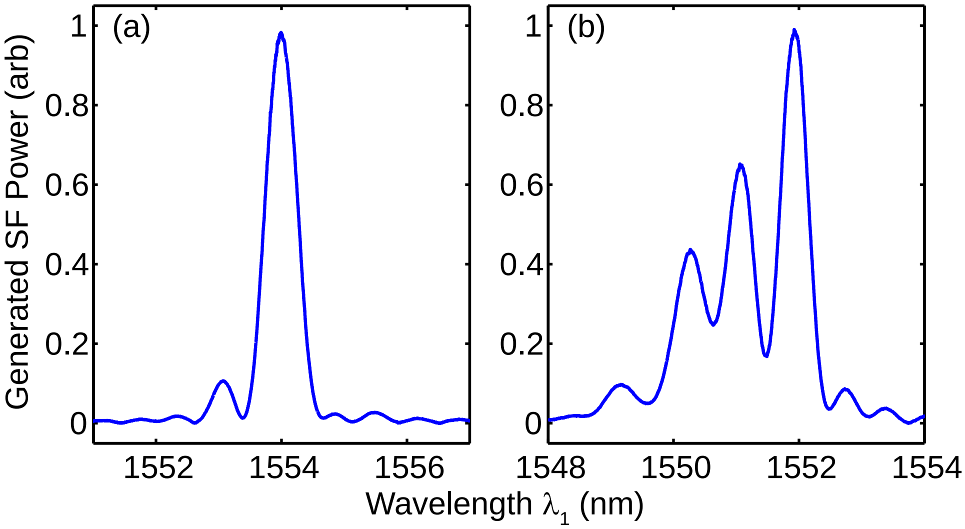

Figure 3.6: Phasematching tuning curves for SFG, showing generated target power at $\lambda_2 = 832$ nm versus wavelength λ_1, showing (a) near-ideal and (b) highly distorted tuning behavior.

3.3.2 Phasematching characterization

The measurement of a QPM tuning curve for a waveguide is a useful diagnostic of waveguide quality. In the low-conversion-efficiency limit, the tuning curve shape is given by $P_2(\Delta k) = \mathrm{sinc}^2\left(\Delta k L/2\right)$. However, any non-ideal waveguide will have nonuniformities in waveguide width and poling quality that will cause the shape of the tuning curve to vary from this ideal shape. Therefore, finding waveguides whose phasematching behavior is near-ideal is an effective method of screening for device quality.

As most of the projects in this dissertation have focused on interactions involving radiation in or near the 1.55-μm telecommunications band, we can make use of the well-developed external-cavity diode lasers (ECDLs), which can be tuned over large bandwidths with no mode hops, enabling a single-shot measurement of the phasematching tuning curve. The use of computer control via GPIB and data digitization using a data acquisition card enabled rapid screening of candidate waveguides.

Two example phasematching tuning curves are shown in Fig. 3.6. In this case, single-frequency radiation at $\lambda_p = 1.8$ μm was combined with the telecom band

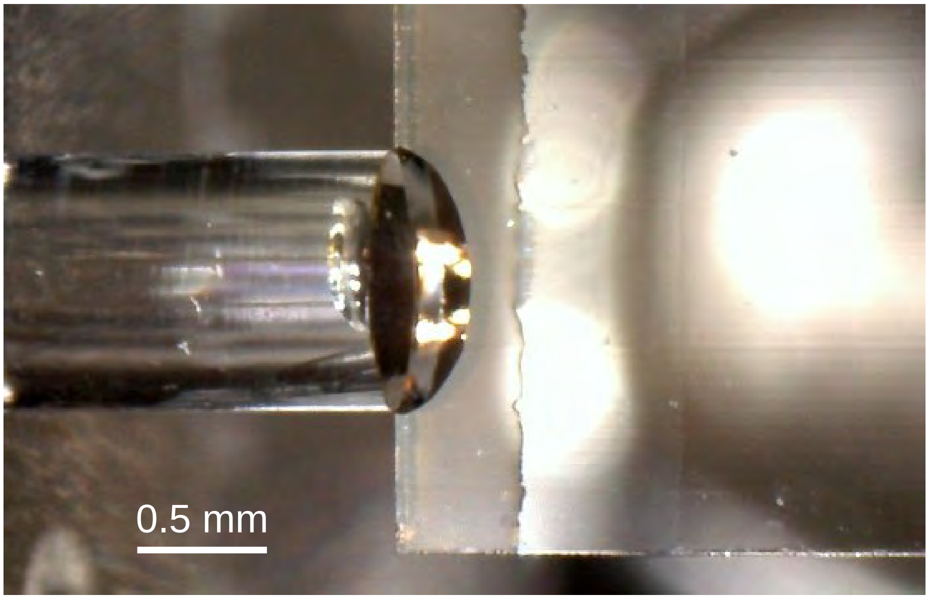

Figure 3.7: Closeup image of a fiber pigtail.

signal at λ_1 in a fiber-optic wavelength combiner. The combined beams were then launched using a fiber collimator and coupled into the waveguide using an aspheric lens ($f = 8$ mm). The waveguides under test were designed for sum-frequency generation to produce target radiation at $\lambda_2 = \left(\lambda_1^{-1} + \lambda_p^{-1}\right)^{-1} = 832$ nm. The generated target radiation was collimated using a second aspheric lens and detected using an amplified Si photodiode. Fig. 3.6(a) shows a near-ideal tuning curve, while the curve in Fig. 3.6(b) shows significant distortions.

3.3.3 Pigtailing

In the previous sections we have described the techniques used for fabricating and characterizing RPE PPLN waveguides for efficient nonlinear optics. Owing to the small size of the optical mode of these waveguides, their use in systems experiments requires some technique to maintain stable alignment. We have designed the input mode filters to support optical modes which closely match those of optical fiber, and therefore can bypass these alignment difficulties by attaching or “pigtailing” an optical fiber ferrule to either the input or output of the waveguide, or both.

Fig. 3.7 shows a closeup image of a fiber pigtail. A SMF-28 optical fiber is packaged inside of a 1-mm-diameter glass ferrule and flat polished. The ferrule is carefully aligned to the desired waveguide while monitoring the transmission of a probe optical signal. To ensure mechanical stability during the alignment procedure, the ferrule is held in a mechanical clamp and the waveguide is held to a working surface using a vacuum clamp. Alignment is done using piezoelectric actuators. As an adhesive we use UV-curing optical-grade epoxy (for example, Norland's NOA-61). A tiny droplet of epoxy is applied between the ferrule and the waveguide using an optical fiber tip. The ferrule is then brought into contact with the waveguide, and then cured using a handheld UV gun. For C-band signals, we can typically achieve coupling loss (including the 4% Fresnel reflection between fiber and $LiNbO_3$) of approximately 0.5 dB. We have also pigtailed waveguides designed for other wavelengths, but because loss measurements are typically done at 1550 nm, it can be difficult to decouple propagation and coupling loss.

Chapter 4

Noise processes in quantum frequency converters

The theory of quantum frequency conversion was described in Chapter 2, and a device platform for achieving high-efficiency frequency conversion was described in Chapter 3. An important aspect of the theory described in Chapter 2 is that the conversion process is, in principle, noiseless. We recall here from Eq. (2.19) that the conversion efficiency in, for example, an upconverter for an input signal ω_1 pumped at ω_p, is given by

$$\eta = \frac{\langle N_2(z = L)\rangle}{\langle N_1(z = 0)\rangle} = \sin^2\left(\sqrt{\eta_{\mathrm{nor}} P_p} L\right) = \sin^2\left(\frac{\pi}{2}\sqrt{\frac{P_p}{P_{\mathrm{max}}}}\right) \tag{4.1}$$

where $N_j = P_j/(\hbar\omega_j)$ and P_p is the pump power [30], and we have assumed negligible propagation loss and pump depletion. For RPE PPLN waveguides, a typical value of η_{nor} is approximately 100%/W/cm^2, which, for a device of length $L = 5$ cm gives a value $P_{\mathrm{max}} = 100$ mW. This power requirement means that, for a pump at, say, 1.06 μm, approximately 5×10^{17} pump photons per second are necessary to reach complete conversion.

Since, even for an extremely efficient converter, such a huge pump photon flux is required for substantial conversion, the converter is highly susceptible even to very weak scattering processes. Any photon within the acceptance bandwidth of the frequency converter, whether present as an input signal or generated via an inelastic

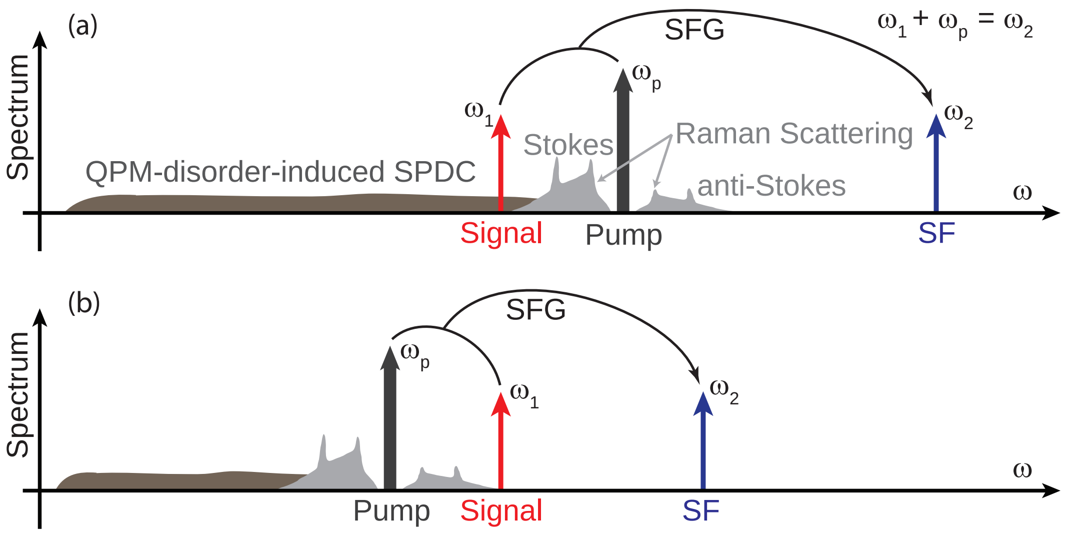

Figure 4.1: Schematic of noise processes in (a) short-wavelength-pumped and (b) long-wavelength-pumped quantum frequency upconverters.

spontaneous scattering event due to the strong pump, will register as a signal. For instance, for a scattering process with a scattering probability of 10^{-12}, one would have a noise floor (for signal-to-noise ratio of 1) of 5×10^5 signal photons/s, a large signal on "single-photon" scales.

In this chapter, we seek to describe the two main spontaneous scattering processes that have been limiting factors in the performance of QFC devices. A schematic of the noise processes we will address is shown in Fig. 4.1. A first such process is spontaneous parametric downconversion (SPDC). In Sec. 4.1, we show that nonidealities in the QPM grating lead to a "white" phasematching noise floor, such that SPDC occurs in a broadband fashion for frequencies lower than ω_p. In Sec. 4.2 we address the second scattering process: spontaneous Raman scattering (SRS). SRS involves either the creation (for the Stokes process) or annihilation (for the anti-Stokes) of an optical phonon in the nonlinear medium. SRS is also found to occur over a broad bandwidth. In Sec. 4.3 we will give a summary of the noise processes and outline some constraints for designing QFC devices with low noise. The theoretical descriptions throughout this chapter will be semiclassical, where our goal is to understand the factors influencing noise performance. Devices for low-noise upconversion will be discussed in Chapter 5, and an application for low-noise downconversion will be discussed in Chapter 6.

We also note that in addition to the scattering processes discussed here, which are fundamental in origin, there are additional technical noise sources that must be overcome in any system implementation. These include noise photons, for example, emitted directly from the pump source used in an experiment. We have studied the noise emission from both erbium- and thulium-doped laser systems, which will be addressed in Chapter 5. One must also take precautions by shielding the devices from environmental stray light that can also manifest as noise photons.

Our work on characterization of SPDC noise and its enhancement due to QPM grating disorder has been published in [48], and measurements of second-harmonic generation and domain characterization studies have been published in [75]. A study of Raman scattering was included in our publication [67].

4.1 QPM random duty-cycle errors: definitions, characterization, and nonlinear optical effects

QPM gratings are subject to a wide variety of fabrication errors, which can influence the nonlinear optical performance of a device. One such error type, random duty-cycle (RDC) errors, are illustrated schematically in Fig. 4.2. We consider a grating with period Λ_G, such that the domains are inverted every $l = \Lambda_G/2$, where, for first-order QPM, $l = L_c = \pi/\Delta k'$. In a device with random duty-cycle errors, the position of the n'th domain boundary z_n deviates from its ideal position by an amount $\delta z_n = z_n - z_{n,0}$, where the ideal domain boundary position $z_{n,0} = nl$. The deviation of the length of the nth domain is thus given as $\delta l_n = l_n - l$, where $l_n = z_{n+1} - z_n$. In a device with RDC errors (and no random period errors), the expectation value $\langle \delta l_n \rangle$ is independent of the domain number n, corresponding to a preservation of long-range order inherent in the fabrication of the grating by lithographic methods. We assume

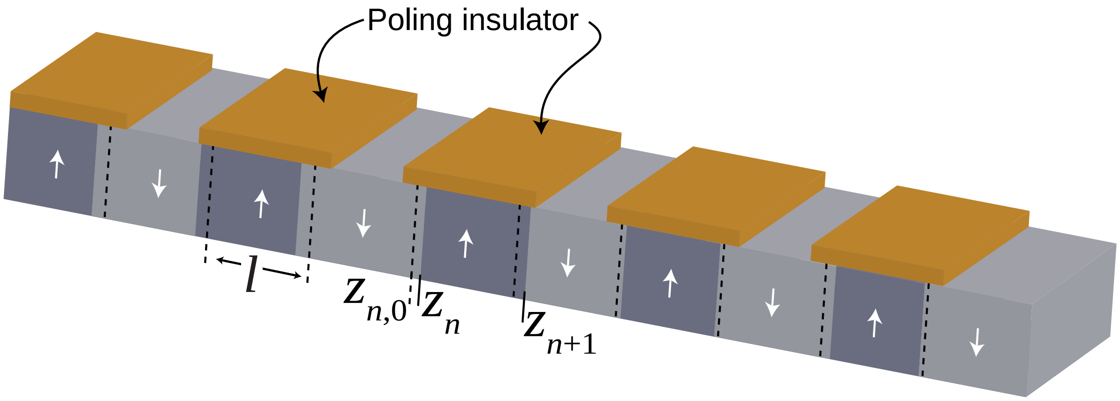

Figure 4.2: Schematic of QPM domains showing random duty-cycle errors.

a Gaussian probability distribution for the l_n:

$$p(l_n) = \frac{1}{\sqrt{2\pi}\sigma_l} \exp\left[-\frac{1}{2}\left(\frac{l_n - l}{\sigma_l}\right)^2\right]. \tag{4.2}$$

where we have defined the domain-length variance as σ_l^2.

4.1.1 Theory of SHG in disordered QPM gratings

Following [57], we consider SHG in the limit of low conversion efficiency. In the following, the subscript 1 indicates the fundamental frequency (FF) and 2 indicates the second-harmonic (SH). In an ideal first-order QPM grating, the intrinsic wave-vector mismatch $\Delta k' = k_2 - 2k_1$ is compensated by a periodic reversal in the sign of the nonlinear coefficient $d(z)$ every coherence length $l_c = \pi/\Delta k'$. For a device of length L, the SH field at $z = L$ relative to a device with an ideal first-order QPM grating is

$$a_2(L) = \int_0^L g(z) e^{i\Delta k' z}\, \mathrm{d}z, \tag{4.3}$$

where we have introduced the normalization $g(z) = (\pi/2L)d(z)/d_0$ such that the Fourier transform $\tilde{g}(\Delta k')$ represents the SHG relative to an ideal QPM grating, as we have previously shown in Sec. 3.1 [75].

For a QPM grating with random duty-cycle (RDC) errors, we can write $g(z)$ as follows:

$$g(z) = \frac{\pi}{2L}\sum_{n=1}^{N}(-1)^n \Pi\left(\frac{z-(z_n-l_n/2)}{l_n}\right), \tag{4.4}$$

where $\Pi((x-x_0)/w)$ is a shifted and scaled rectangle function

$$\Pi\left(\frac{x-x_0}{w}\right) = \begin{cases} 0, & x \leq x_0 - w/2, \\ 1, & x_0 - w/2 < x < x_0 + w/2, \\ 0, & x \geq x_0 + w/2. \end{cases} \tag{4.5}$$

We are interested in the quantity $\langle|\tilde{g}(\Delta k')|^2\rangle$, the efficiency, relative to an ideal grating, of SHG at a phase mismatch $\Delta k'$, where the expectation value is over an ensemble of gratings with randomly perturbed, independent and identically distributed (IID) z_n. For deviations from phasematching small compared to an inverse domain length, i.e. $|\Delta k| = |\Delta k' - \pi/l| \ll l^{-1}$, we find

$$\langle|\tilde{g}(\Delta k)|^2\rangle = f(\sigma_l)\,\mathrm{sinc}^2\left(\frac{\Delta k L}{2}\right) + \frac{1-f(\sigma_l)}{N}, \tag{4.6}$$

where the function $f(\sigma_l) = \exp(-\pi^2\sigma_l^2/2l^2)$. A complete derivation of Eq. 4.6, valid not only for SHG but for difference-frequency generation, is given in Appendix A.

The relative SHG efficiency $\langle|\tilde{g}(\Delta k)|^2\rangle$ calculated in Eq. (4.6) consists of two components. The first represents the $\mathrm{sinc}^2(\Delta k L/2)$ tuning behavior of a QPM device with an efficiency reduced by the amount $f(\sigma_l)$, an effect discussed in [57]. The second component is a flat QPM pedestal of height $(1-f(\sigma_l))/N$ that is independent of Δk. We note that as the grating disorder σ_l is reduced, $f(\sigma_l)$ approaches 1, and the device regains the characteristics of an ideal grating. Conversely, as the grating disorder is increased, one encounters the behavior of the random QPM devices studied in [76, 77], in which the growth of the SH field scales as $L^{1/2}$, i.e. the field grows in a random-walk fashion. The pedestal height can be estimated to within numerical factors by a simple physical argument: on average, the portion of a domain in which the SH evolution occurs randomly is $\bar{\sigma}_l = \sigma_l/l$. Therefore, the intensity of the random component of the SHG scales as $(\bar{\sigma}_l\sqrt{N})^2$, which when divided by the N^2 dependence of ideal SHG intensity, gives $\bar{\sigma}_l^2/N$.

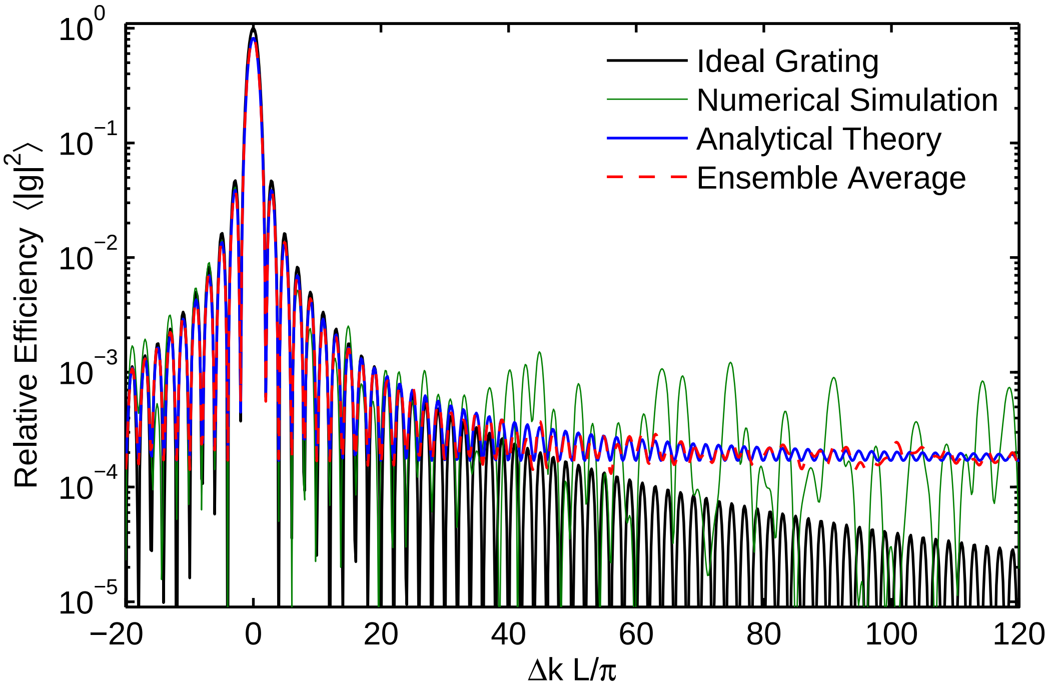

Figure 4.3: Simulation and analytic theory of SHG in a QPM grating with domain disorder. Parameters: $\bar{\sigma}_l = 0.2$, $L = 1$ cm, ensemble average over 100 disordered gratings.

To test the analytical theory, we performed both numerical simulations and experiments. Our experiments on SHG in an RPE PPLN waveguide will be discussed in Sec. 4.1.3. Numerically, we constructed an ensemble of 100 disordered QPM gratings, with domain lengths drawn from a Gaussian distribution and with normalized pseudo-random duty-cycle error $\bar{\sigma}_l = 20\%$. The simulation was for a device of length $L = 1$ cm with a poling period of $\Lambda_G = 16$ μm, suitable for 1.55-μm SHG, and the total number of domains was $N = L/(\Lambda_G/2) = 1250$. The SHG tuning behavior is calculated by a direct integration of Eq. 4.3 for each grating. The SHG tuning behavior for each grating is normalized to the performance of an ideal grating, and an ensemble average is computed. This ensemble average is plotted in Fig. 4.3 (dashed red curve) along with the prediction of the analytical theory (solid blue curve), showing excellent agreement on the height of the QPM pedestal. For frequencies far from the QPM peak, the pedestal results in elevated generation efficiency when compared with the ideal QPM grating (solid black). Also shown are the results for a single disordered QPM grating (thin solid green). We note that while the ensemble average of the pedestal is white, an individual grating can exhibit large fluctuations in efficiency far from the QPM peak. Properties of the statistics of the pedestal height are discussed in Appendix A.

4.1.2 Characterization of RDC errors

A direct study of random duty-cycle errors via microscopy or other means would enable an estimate of the expected QPM pedestal height $\langle|\tilde{g}|^2\rangle$ in real devices. We analyzed the severity of random duty-cycle errors in an electric-field periodically poled $\mathrm{LiNbO_3}$ sample. We poled a 76-mm-diameter 0.5-mm-thick lithium niobate wafer via the techniques described in Sec. 3.1. To decorate the inverted domains, we etched the original $+z$ surface of the wafer in hydrofluoric acid (HF) for 20 min. HF etches the $+z$ domain orientation at a higher rate than the $-z$ orientation, and thus the etch provides topographic contrast between the two domain orientations, which can be observed optically. We chose to measure the domain statistics on the original $+z$ surface of the wafer as this is the side upon which the waveguides are formed. As the domains do not propagate perfectly straight through the substrate during poling, the domain positions on the $+z$ surface will provide the best representation of the domain disorder “experienced” by a signal propagating through a RPE waveguide.

We next sought a technique whereby we could accurately measure the positions of a large number of ferroelectric domain boundaries, such that statistics of their positions and the domain sizes could be obtained. An effective measurement technique would provide lateral resolution below 0.1 μm, while providing enough field of view (> 100 μm) to measure a large number of domains simultaneously. The first measurement technique we explored was atomic force microscopy (AFM) [78], which has excellent spatial resolution due to the extremely sharp AFM tip (a few nm, easily) but limited field of view due to the fact that spatial scanning is done using piezoelectric actuators. A second techinque widely used to measure topographic contrast is surface profilometry, in which a metal stylus is dragged over a surface and the surface topography is recorded. Profilometry can give very long linear travel ranges (hundreds of μm or even a few mm) with very high (sub-nm) depth resolution. The disadvantage of such techniques is that the stylus tip diameter is usually on the order of 10 μm, on the order of a typical domain size for a PPLN device. As we were seeking to characterize domains with $l \approx 5$ μm, profilometry was not an appropriate choice, but could be used for very-long-pitch QPM gratings.

The most effective domain characterization techniques were based on optical microscopy. One can view the domain pattern directly using a high-magnification objective lens. Provided any imaging abberations can be corrected (for example, by imaging a lithographic mask as a calibration sample), using image processing methods one can accurately determine the domain boundary positions. Microscopy has been used since earliest days of periodic poling to measure statistics of domains sizes [79]. While microscopy is effective, our best results were obtained using Fizeau (Zygo) interferometry, which can more easily provide quantitative information on the depth as it is measured by interfering the wavefront off the sample to be characterized with the perfectly flat wavefront from a reference surface [80].

We obtained Zygo micrographs at 7 positions across a 76-mm-diameter PPLN wafer. A sample image is shown in Fig. 4.4. Using a 50× objective, we have a field of view of 150×113 μm in a 640×480 pixel image. To determine the domain size, we first projected each domain row onto an axis parallel to K_G, which formed a line trace of surface height for each domain. We numerically defined the domain boundary as the position at which the surface height is midway between the minimum (in the $+z$ areas) and maximum (on the $-z$ poled islands). After analyzing all the images, we formed a histogram of the inverted domain sizes: the results are shown in Fig. 4.5.

The wafer we analyzed was poled with a grating period $\Lambda_G = 10.22$ μm. We observed a mean inverted-domain width of 5.90 μm, which for the poling which corresponds to a duty cycle of 58%. From the histogram we also calculate $\sigma_l = 0.41$ μm, which corresponds to normalized RDC error of $\bar{\sigma}_l = 8.0\%$. The solid line in Fig. 4.5 is a fit to a Gaussian distribution, which shows good agreement with the observed histogram, supporting the assumptions made in the development of the analytical theory. The only significant deviation from Gaussian statistics is a longer tail towards

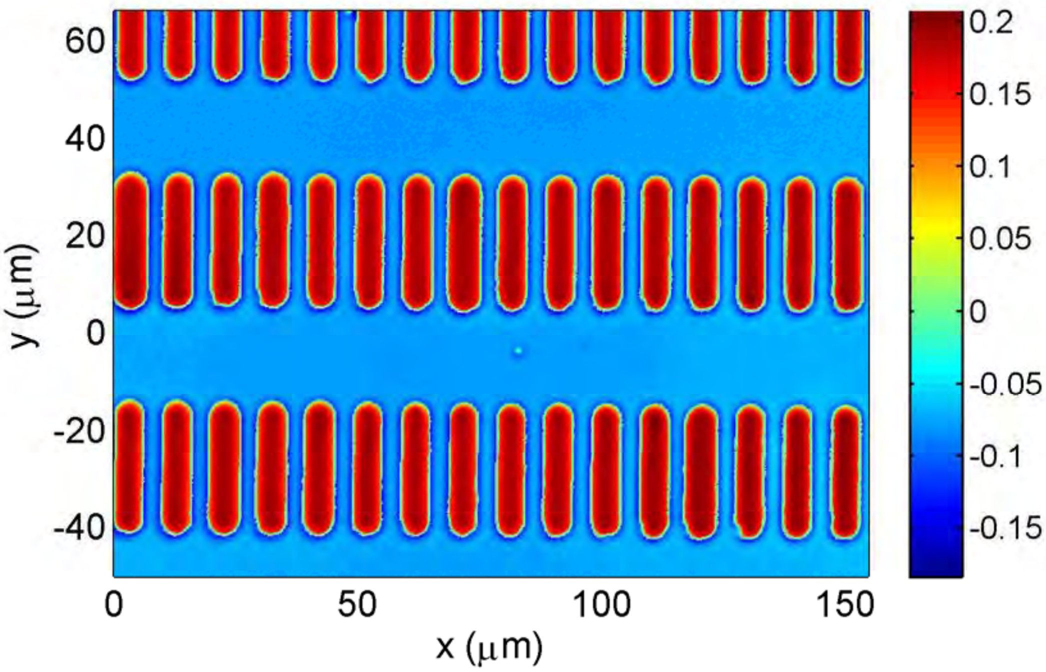

Figure 4.4: Surface topography of etched PPLN wafer measured using Zygo interferometry, showing inverted ferroelectric domains with random duty-cycle errors. Color bar scale in μm.

larger domains. To test whether the tail has a significant influence on the behavior of the QPM pedestal we performed SHG simulations with domain length statistics drawn from the distribution we observed in Fig. 4.5 and compared the results to those done using a Gaussian distribution with the same average duty cycle. The computed efficiency far from the QPM peak agreed to within approximately 2% using both sets of domain statistics.

4.1.3 Observation of QPM pedestal

We next sought to characterize the effects of RDC errors on SFG far from phasematching in a real PPLN sample. Because the theory and simulations described above both

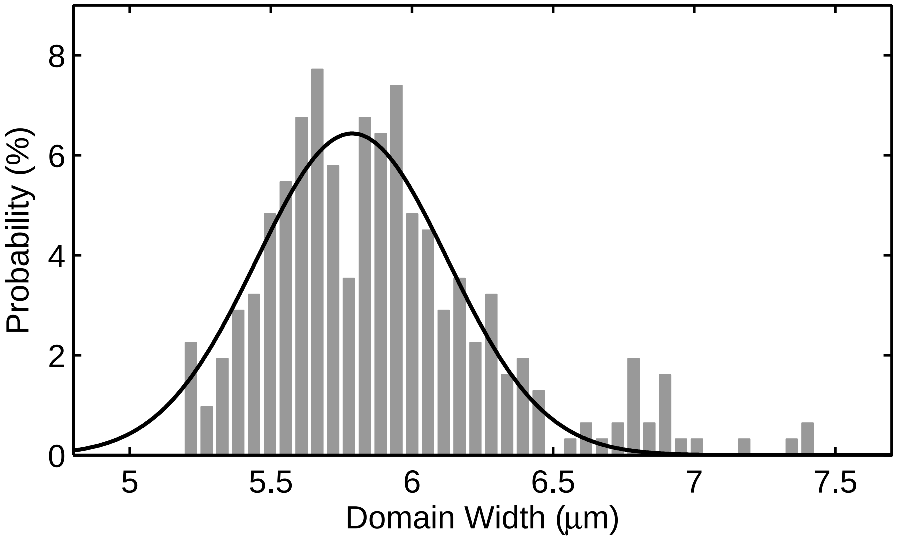

Figure 4.5: Histogram of inverted domain sizes l for a PPLN wafer with $\Lambda_G = 10.22$ μm, with Gaussian fit. $\langle l \rangle = 5.90$ μm, with $\sigma_l = 0.41$ μm.

represent plane-wave physics, we performed experiments using guided-wave interactions, which are mathematically isomorphic to plane-wave interactions. We fabricated reverse-proton-exchanged PPLN waveguide devices with 59-mm-long QPM gratings. The waveguides incorporate mode filters and adiabatic tapers to facilitate launching the FF fundamental spatial mode [30]. The output facet of the waveguide was polished at an angle of 5° to prevent Fabry-Perot interference effects. The poling period was 15.9 μm, which resulted in a first-order QPM peak at 1533.75 nm at a temperature of 25° C, as seen in Fig. 4.7 Inset 1. The experimental setup is shown schematically in Fig. 4.6. In the experiment, we used two external cavity diode lasers to cover the 90-nm measurement range. The FF light was modulated with a mechanical chopper and was was coupled in and out of the waveguide using aspheric lenses ($f = 8$ mm), and the outgoing SH and residual FF light were separated using a dichroic mirror. The SH light at the chopper frequency was detected using an unbiased Si photodiode connected to the current input of a lock-in amplifier, and the outgoing FF light was monitored using a calibrated InGaAs detector. The FF wavelength was stepped in increments of 0.01 nm, and the sensitivity of the lock-in amplifier was adjusted depending on the SH signal level to enable a high dynamic

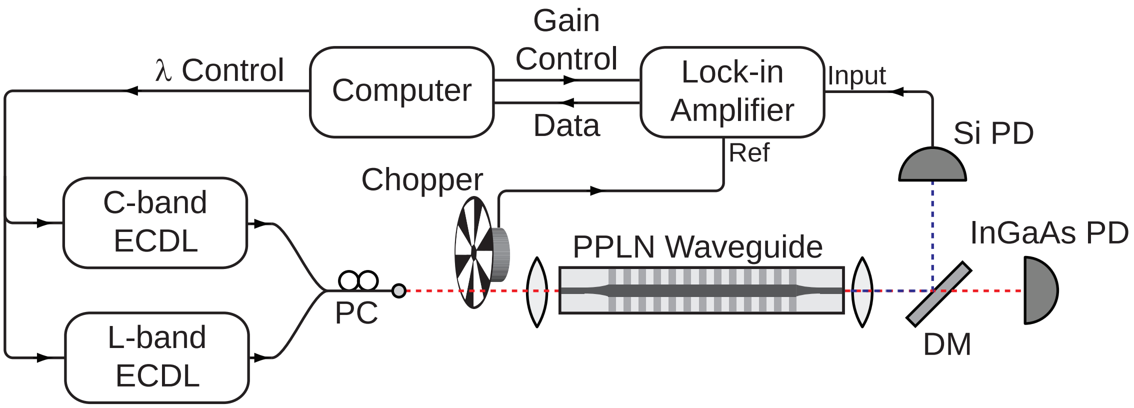

Figure 4.6: Experimental setup for observation of SHG QPM pedestal.

range measurement.

The normalized SHG efficiency $\langle|\tilde{g}(\lambda)|^2\rangle$ was computed from the measured SH and FF data, and is plotted as the dashed line in Fig. 4.7. When compared with the phasematching behavior of an ideal grating (solid black curve), at large detunings from the QPM peak one observes a QPM pedestal. Although the data appear noisy, ripples in the generation efficiency are in fact well-resolved by the lock-in measurement technique, as demonstrated by Inset 2, which shows an expansion of the data from 1555 to 1560 nm. Similar ripples are observed in the simulations, and the observed spectral features are repeatable over a series of measurements of an individual device. The solid red line is the average efficiency far from phasematching: the pedestal height $\langle|\tilde{g}(\lambda)|^2\rangle = 5.2 \times 10^{-6}$, which, according to Eq. (4.6), corresponds to a RDC error of $\bar{\sigma}_l = 8.9\%$.

Also observed in Fig. 4.7 is a parasitic QPM peak at 1586 nm, at a level 27 dB below the main QPM peak. We believe this smaller peak to be due to an interaction involving a higher-order spatial mode of the waveguide. To investigate this possibility, we used the predictions of the waveguide mode solver that has been described in [56]. For a primary QPM peak (involving the TM_{00} modes at both the FF and SH) at 1534 nm, the simulations predict a QPM peak for a sum-frequency generation process involving one TM_{00} and one TM_{01} mode at 1586 nm, which is coincident with the observed parasitic QPM feature. We therefore hypothesize that a small amount of

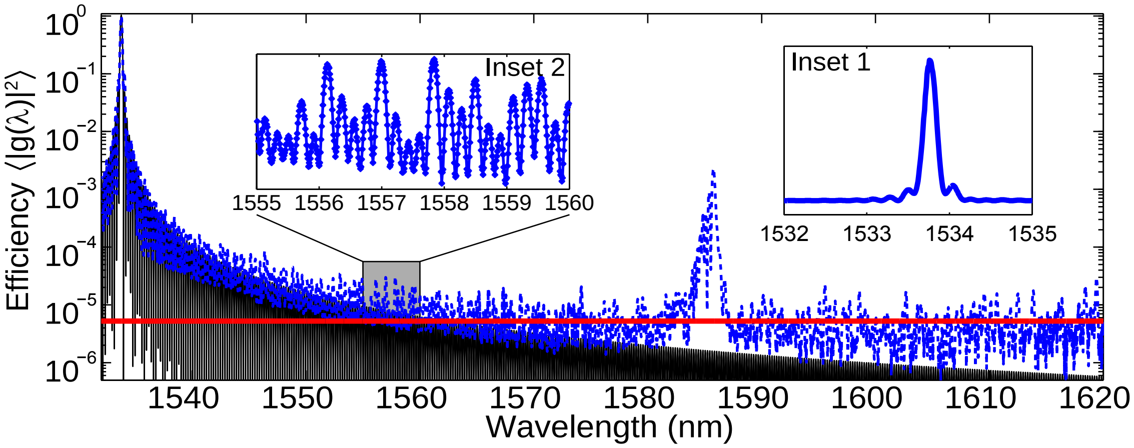

Figure 4.7: Measured relative SHG efficiency $\langle|\tilde{g}(\lambda)|^2\rangle$ (blue dashed) plotted against ideal $\mathrm{sinc}^2(\Delta kL/2)$ QPM tuning curve (solid black), showing efficiency pedestal far from the QPM peak. Inset 1: measured SHG tuning curve plotted on linear scale. Inset 2: zoom of measured data between 1555 and 1560 nm.

power was coupled into the TM_{01} mode at the input of the waveguide due to an imperfect mode filter or adiabatic taper. Because the parasitic QPM peak is 27 dB below the main peak, it does not affect the observed results for the QPM pedestal away from the parasitic peak: any QPM pedestal for this process would also be at a level 27 dB below the QPM pedestal for the fundamental spatial-mode interaction. We also note that at wavelengths bluer than the primary QPM peak at 1534 nm we observed several additional QPM peaks due to SHG of higher-order spatial modes at the second-harmonic frequency.

4.1.4 Domain-disorder-enhanced parametric fluorescence

In a quantum frequency conversion device, the QPM pedestal described here can have several effects. The first is that, since a strong pump at λ_p must be used, there will be parasitic second-harmonic radiation created at $\lambda_p/2$. Since this parasitic process produces radiation at a known frequency that is generally far removed from either the signal or target frequencies it can generally be filtered straightforwardly.

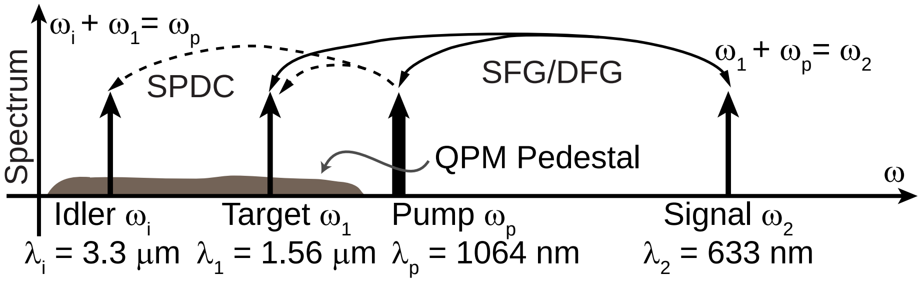

Figure 4.8: Frequencies and wavelengths involved in downconversion of a weak signal at $\lambda_2 = 633$ nm to a target wavelength $\lambda_1 = 1.56$ μm. The strong pump at $\lambda_p =$ 1064 nm is also undergoing parametric fluorescence, creating noise when the signal photons overlap spectrally with the detection bandwidth near λ_1.

However, an additional effect of the QPM disorder is in the process of spontaneous parametric fluorescence. Parametric fluorescence is the spontaneous splitting of a pump photon into a lower energy signal/idler pair with energies $\omega_{\text{sig}} + \omega_{\text{idl}} = \omega_p$. It is a phasematched process, and has been studied in both the microwave [43] and optical domains [81] since the 1960s. The mathematical expressions describing low-gain parametric amplification (a classical approximation to parametric fluorescence) are the same as for SHG (i.e. in both cases there is no pump depletion, and the phase-matching behavior is governed by the same Fourier transform relation of Eq. (4.3)). However, its effects as a parasitic process are to generate a "white noise"-like collection of photons at all frequencies $\omega < \omega_p$ for which both the signal and idler photons are within the transparency range of the material. While the existence of the noise photons throughout the entire transparency window has not been verified, here we describe an experiment in which a noise signal was observed in the 1.5-μm band using a pump at $\lambda_p = 1.06$ μm, in a waveguide in which this parametric fluorescence process was strongly phase-mismatched.

We investigated the parasitic parametric fluorescence noise in the context of an experiment designed to simulate the downconversion of single photons from a diamond NV center (with a zero-phonon emission wavelength of $\lambda_2 = 637$ nm; NV center single-photon sources are described in more detail in Sec. 7.1.3) to a wavelength $\lambda_1 = 1.56$ μm in the telecommunications band using a pump wavelength $\lambda_p = (\lambda_2^{-1} - \lambda_1^{-1})^{-1} = 1064$ nm. A schematic of the frequencies that are involved in

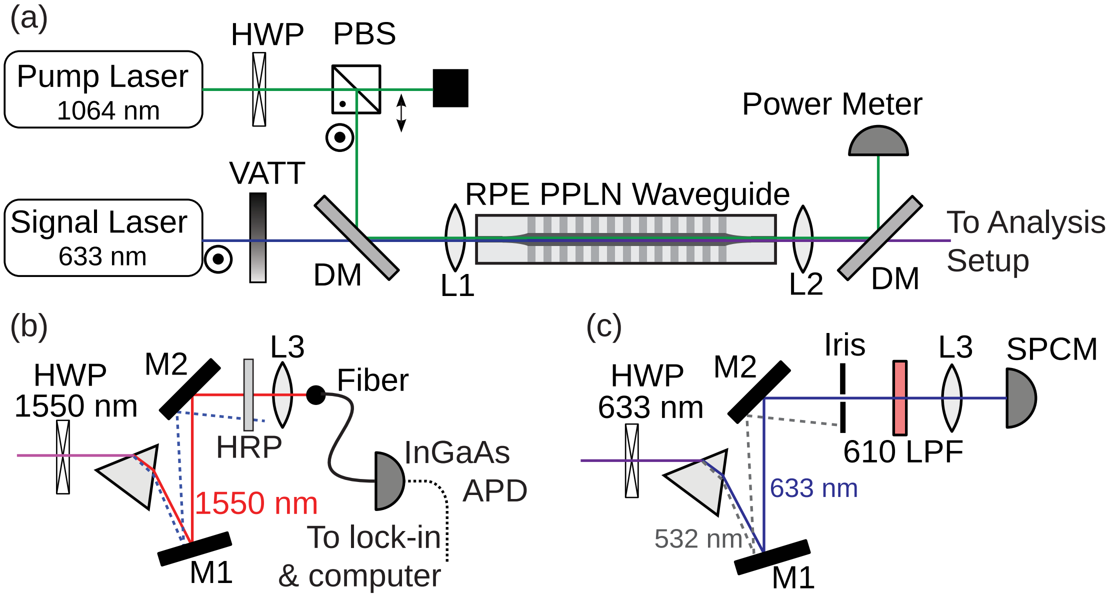
(a)
Pump Laser
1064 nm
HWP
PBS
Power Meter
VATT
RPE PPLN Waveguide
Signal Laser
633 nm
DM
L1
L2
DM
To Analysis Setup
(b)
HWP
1550 nm
M2
L3
Fiber
HRP
InGaAs
APD
1550 nm
To lock-in
& computer
M1
(c)
HWP
633 nm
M2
Iris
L3
SPCM
610 LPF
633 nm
532 nm
M1

Figure 4.9: Experimental setups for measurement of weak-signal downconversion from 633 nm to 1.56 μm. For the measurement of SPDC noise, we either (b) used a linear-mode InGaAs APD and a lock-in detection technique, or, (c) measured the upconversion of noise photons to 633 nm using a Geiger-mode Si APD.

this process are shown schematically in Fig. 4.8. In addition to pumping the conversion process between the signal at λ_2 and the target at λ_1, the strong pump can also undergo parametric fluorescence, indicated by the "QPM pedestal". For pump photons splitting into a photon at the target wavelength λ_1, the corresponding idler wavelength is $\lambda_i = 3.3$ μm.

A schematic of our experimental setup is shown in Fig. 4.9. As a weak signal we used a HeNe laser at 632.8 nm in which the power was adjusted using a variable attenuator. The pump laser was a Nd:YAG nonplanar ring oscillator (NPRO, [82]) with maximum output power of 0.75 W. The pump power was controlled using a half-wave plate (HWP) and polarizing beam splitter (PBS) and was combined with the signal beam on a dichroic mirror (DM). The light was in- and out-coupled from the PPLN waveguide using aspheric lenses (f = 8 mm) with AR coating for the strong pump. We estimate a waveguide coupling efficiency of 40% (5%) at the pump (signal) wavelength. Overall coupling efficiency for the signal was not a concern for this characterization experiment, and as such no special effort was made to maximize this quantity. Additionally, the waveguide mode filter for this device was designed to be single-mode for the 1064-nm pump; a mode filter that was single-mode at $\lambda_2 = 633$ nm would be in the cutoff regime at λ_p.

Using the variable attenuator, we adjusted the signal power such that $P_2(0) = 50$ nW was coupled into the waveguide. We then measured the generated target-wavelength power at the waveguide output $P_1(L)$ as a function of the pump power P_p by coupling the light at the output of the waveguide into an optical spectrum analyzer (OSA). By normalizing to the input signal power, we calculated the conversion efficiency and plotted the results as squares in Fig. 4.10; the solid curve is a fit to Eq. (4.1), showing good agreement. The maximum conversion efficiency was found to be approximately 80% and was reached at $P_p = P_{\text{max}} = 78$ mW. At P_{max} we observed 13 dB (95%) depletion of the input signal, which we suspect was limited by residual higher-order spatial mode content at λ_2. The conversion efficiency was also limited by propagation losses, which were measured (estimated) to be 0.2 (0.1) dB cm^{-1} at λ_1 (λ_2).

Following measurement of the conversion efficiency, we sought to measure the parametric fluorescence noise. Because of the difficulty of counting photons in the 1.55 μm spectral region, this task posed a measurement challenge. We measured the noise in two ways, shown schematically in Fig. 4.9(b) and (c). In short-wavelength-pumped upconversion single-photon detectors pumped with 1.06 μm lasers, noise counts of the level of 10^6 counts/s were observed, nominally within a narrow (0.5 nm) nm spectral window around 1.55 μm [29]. Therefore, it seemed logical that if we deliberately set the collection bandwidth substantially larger than this, we might be able to detect the macroscopic numbers of photons on a sensitive linear-mode detector. In this setup, shown in Fig. 4.9(b), the polarization of the light exiting the waveguide was first rotated from s to p using a 1550-nm HWP. The light was then sent though a prism at Brewster's angle and sent through a plane-parallel dielectric mirror with high reflectivity at 1064 nm (HRP) to remove the pump light from the signal. It was then coupled into a single-mode optical fiber and sent to a linear-mode InGaAs APD. To achieve high sensitivity, the pump was modulated at ~300 Hz using

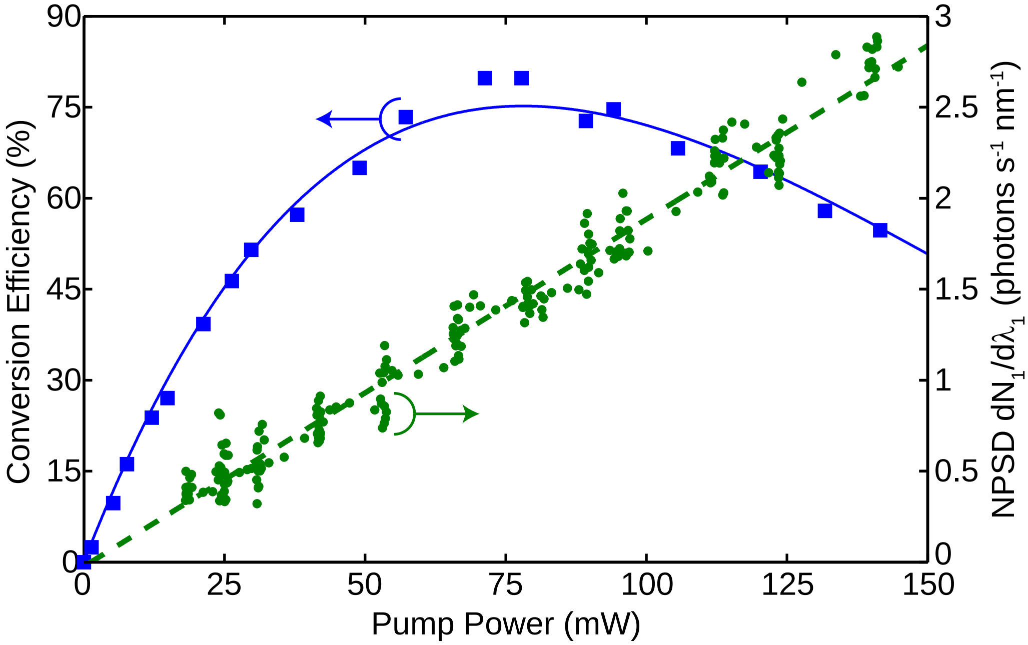

Figure 4.10: Measured DFG conversion efficiency (squares) and fit to Eq. (4.1) (solid blue), showing maximum conversion at $P_{\max} = 78$ mW.

an optical chopper, and the photocurrent of the InGaAs APD was detected using a lock-in amplifier.

We calibrated the measurement bandwidth by sending the light from a tunable C-band ECDL through the waveguide and into the measurement setup: the collection bandwidth was measured to be 44 nm ($1/e^2$ full-width). An absolute calibration of the responsivity of the detection setup was done by inserting a 1.56-μm probe beam of known optical power into the filtering setup. Plotted as dots in Fig. 4.10 are data recorded by monitoring the lock-in signal on a computer while the pump power was varied using the HWP. The data are well fit by a linear dependence on pump power as expected for a spontaneous scattering process. We find a noise-photon spectral density (NPSD) of 1.45×10^6 s^{-1} nm^{-1} at $P_p = P_{\max}$. We note that any noise produced in waveguides without a QPM grating was below the estimated 10^5 s^{-1} nm^{-1} sensitivity of the detection system.

An expression for the generation rate of photon pairs via SPDC in a waveguide has been given by Fiorentino and coworkers [83]. They find

$$\frac{\mathrm{d}N_1}{\mathrm{d}\lambda_1} = \frac{8\pi^2 d_{\mathrm{eff}}^2}{\epsilon_0 n_1 n_i n_p \lambda_1^3 \lambda_i} \frac{P_p}{A_I} L^2 \,\mathrm{sinc}^2\left(\frac{\Delta k L}{2}\right) \tag{4.7}$$

where A_I is the interaction area given as $A_I = \Theta^{-2}$. Evaluating this expression for the expected NPSD for our experimental configuration with $\Delta kL \approx -1.8 \times 10^4$ gives a rate of approximately 10^2 photons s^{-1} nm^{-1}, about 4 orders of magnitude lower than the value observed in the experiment. We note here that additional complexities arise in our experimental configuration due to the fact that the idler wave at 3.3 μm is in the cutoff regime of the waveguide, such that radiation modes must be considered. As a result, A_I for this process cannot be calculated in the way described in Chapter 2 for interactions involving only bound modes of the structure. A detailed discussion of this effect is given in Appendix B: using the waveguide mode completeness relations, when there are no bound modes at the idler wavelength, the mode-overlap integral Θ takes a different form than in Eq. (2.10). We show in Appendix B that in the absence of bound modes at the idler frequency,

$$\Theta_{\mathrm{Cer}}^2 = \frac{1}{A_I} = \iint |u_p(x,y) u_1(x,y)|^2 \,\mathrm{d}x\,\mathrm{d}y\,. \tag{4.8}$$

As we have seen above, the QPM pedestal dominates the efficiency of a process when $|\Delta kL| \gtrsim 100\pi$. We then replace the $\mathrm{sinc}^2(\Delta kL/2)$ in Eq. (4.7) with the QPM pedestal height

$$\tilde{g}_\infty^2 \equiv \langle|\tilde{g}(\Delta k \to \infty)|^2\rangle = \frac{1}{N}\left(1 - e^{-\pi^2 \bar{\sigma}_l^2/2}\right) \tag{4.9}$$

and calculate the NPSD for an observed grating disorder, obtaining a value $\bar{\sigma}_l \approx 21\%$. This value is higher than that observed by direct imaging of a comparably fabricated device, but we have not investigated the uniformity of $\bar{\sigma}_l$ across an ensemble of devices. Unfortunately due to the destructive nature of RDC error measurements using Zygo interferometry we were unable to measure $\bar{\sigma}_l$ directly for this device.

Any noise photons generated via parametric fluorescence within the acceptance bandwidth $\delta\lambda$ around the target wavelength of λ_1 of the device are indistinguishable

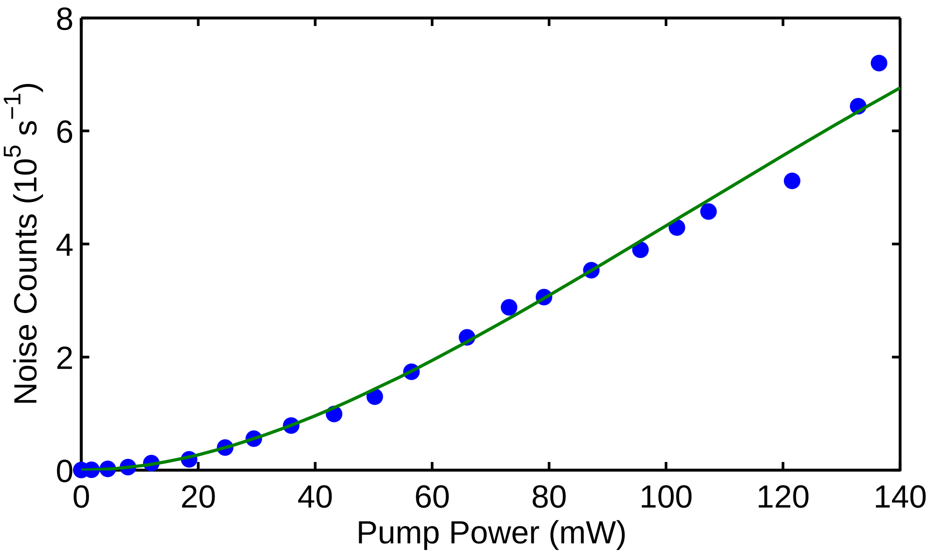

Figure 4.11: Measurement of upconverted parametric fluorescence noise (circles) and fit to semiclassical theory (solid).

from target photons and will be efficiently upconverted via SFG to the signal wavelength at λ_2. We can therefore measure the effects of the parametric fluorescence noise via measuring this upconverted noise signal at 633 nm using a Si photon counter. The experimental setup we used for this measurement is shown in Fig. 4.9(c). The light exiting the waveguide was passed through a HWP for 633 nm to rotate the polarization from s to p, and was then sent through a Brewster-angled prism to separate the upconverted noise photons at 633 nm from the parasitic radiation at 532 nm due to SHG of the pump (which had an optical power of approximately 50 nW due to RDC-error-enhanced SHG). Following the prism, an additional long-pass filter was used and the light was then focused onto a Si APD (PerkinElmer SPCM-AQR-14). Our measurement of the upconverted noise rate is shown as dots in Fig. 4.11. It can be seen that the upconverted noise grows quadratically at first, followed by linear growth with pump power. This behavior can be understood by a simple physical argument: at low pump powers, both the noise-photon generation rate and the upconversion efficiency are linear in pump power, leading to quadratic scaling. At higher pump powers, the noise photon generation rate remains linear but the conversion efficiency flattens, saturates, and rolls over, such that the total upconversion rate is effectively linear.

We have constructed a semiclassical model for this parasitic upconversion process in QPM media with RDC errors. The coupled wave equations for the combined SPDC and SFG processes are given as:

$$\frac{\mathrm{d}a_i}{\mathrm{d}z} = i\kappa_N a_1^* a_p e^{i\,\Delta k_N z} \tag{4.10a}$$

$$\frac{\mathrm{d}a_1}{\mathrm{d}z} = \kappa_1 a_p^* a_2 e^{i\,\Delta k_S z} + i\kappa_N a_i^* a_p e^{i\,\Delta k_N z} \tag{4.10b}$$

$$\frac{\mathrm{d}a_2}{\mathrm{d}z} = i\kappa_S a_p a_1 e^{-i\,\Delta k_S z} \tag{4.10c}$$

where κ_S and $\Delta k'_S$ are the coupling coefficient and phase mismatch for the SFG process, and κ_N and $\Delta k'_N$ are for the noise (parametric fluorescence) process. To study these combined interactions in a material with RDC errors, our approach is to numerically construct a grating with quasi-random duty-cycle errors, and solve Eqns. (4.10), and take an ensemble average over many such disordered gratings. The boundary conditions used to simulate Eqs. (4.10) were a small seed $a_i(0) = a_{i0}$ and $a_1(0) = 0$. The results of this simulation are shown as the solid curve in Fig. 4.11. The simulated curve has one free parameter, an overall scale factor, but the particular shape has been determined by the value $P_{\max} = 78$ mW.

4.1.5 RDC error tolerances

We can combine the rate of SPDC of Eq. (4.7) and the QPM pedestal height of Eq. (4.9) to derive tolerances on the maximum allowable random duty-cycle error $\bar{\sigma}_l$ to achieve a desired conversion efficiency η and NPSD $dN_1/d\lambda_1$. Writing η as a function of P_p using Eq. (4.1) gives

$$P_p = \frac{1}{\eta_{\mathrm{nor}} L^2}\left(\sin^{-1}\sqrt{\eta}\right)^2. \tag{4.11}$$

Inserting this result into the NPSD expression of Eq. (4.7) and rearranging, we are led to the following result following a Taylor series expansion (to second order in σ_l/l)

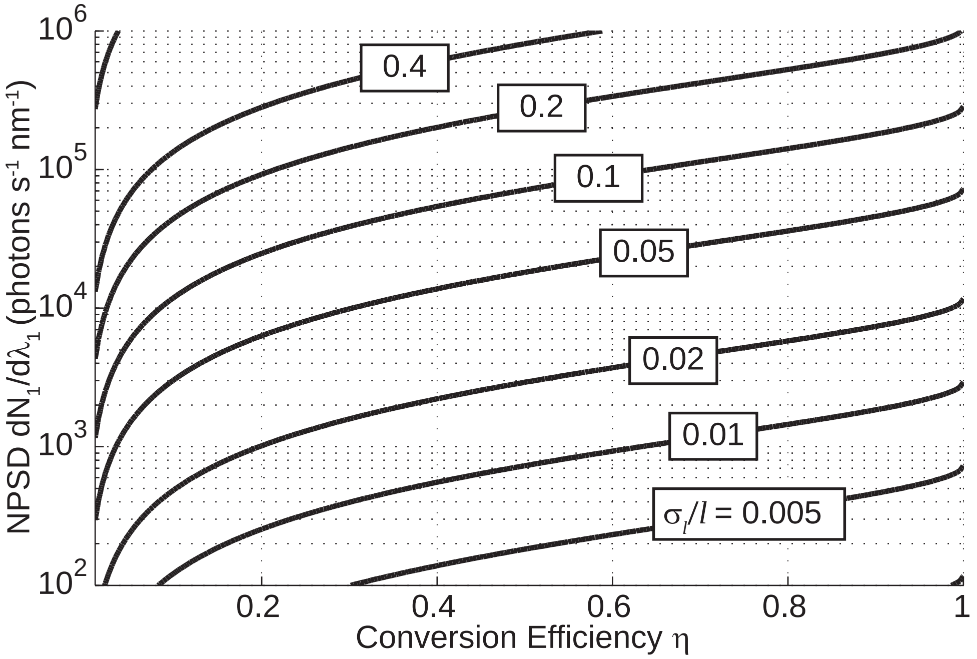

Figure 4.12: Calculated random duty-cycle error $\bar{\sigma}_l = \sigma_l/l$ tolerances for achieving conversion efficiency η and noise-photon spectral density $dN_1/d\lambda_1$ for a QFC device with domain disorder.

for the pedestal height $\tilde{g}^2_\infty$ from Eq. (4.9):

$$\left(\frac{\sigma_l}{l}\right)^2 = \left(\frac{2Nn_i\lambda_i\lambda_1^2}{\pi^2 n_2\lambda_2 c}\right)\frac{\mathrm{d}N_1}{\mathrm{d}\lambda_1}\frac{r}{\sin^{-1}\sqrt{\eta}}. \tag{4.12}$$

Here, $N = L/(\Lambda_G/2)$ is the number of QPM domains in the waveguide, and r is a ratio of the square of the mode-overlap integrals for the SPDC to the SFG/DFG processes. For a waveguide with bound modes at all frequencies, Θ was given in Eq. (2.10), and for a waveguide with a radiated idler, the calculation in Appendix B gives the form of Eq. (4.8). For our experimental parameters, we calculate $r = 1.03$, a result based on simulated waveguide modes for the waveguide parameters used in the device fabrication. By use of the Cauchy-Schwarz inequality it can be noticed that in the Čerenkov configuration $r \geq 1$ in all cases.

We can visualize the implications of Eq. (4.12) by making a contour plot of values of constant $\bar{\sigma}_l$ as a function of the conversion efficiency η and NPSD $\mathrm{d}N_1\,/\,\mathrm{d}\lambda_1$, shown in Fig. 4.12 for a device with $N = 10^4$ (corresponding to a device of length $L = 5$ cm with a poling period $\Lambda_G = 10\ \mu$m) and operating at the wavelengths shown in Fig. 4.8. The ideal QFC device would have as high a conversion efficiency and as low a NPSD as possible, corresponding to a position at the lower right corner of Fig. 4.12. As can be seen from Eq. (4.12), operation in this regime requires extraordinarily tight tolerances on RDC errors during fabrication $\bar{\sigma}_l < 0.5$ %, beyond current fabrication technology. The "state-of-the-art" of our electric field poling procedures as described in Sec. 3.2 seems to yield $\bar{\sigma}_l \approx 10\%$, which corresponds to a noise-photon spectral density of approximately 10^5 photons s^{-1} nm^{-1}, a value that seems prohibitively high for use in applications even if very aggressive optical filtering is used. Another consequence of the result of Eq. (4.12) is that the tolerances on $\bar{\sigma}_l$ are reduced as the device gets longer and N increases. This behavior results from the increase as $\eta \propto L^2$ in the conversion efficiency of the QFC process while the noise generation rate (a spontaneous process) grows as $\mathrm{d}N_1 \,/\, \mathrm{d}\lambda_1 \propto L$, such that longer L is always favored.

We have applied the analyses described here to a previous demonstration of 1064-nm-pumped quantum frequency conversion: an upconversion single-photon detector demonstrated by Albota and Wong at MIT in 2004 [29]. That experiment used a bulk PPLN crystal as the conversion medium, requiring a redefinition of r to include the effects of Gaussian beam propagation. Working in the near-field Gaussian approximation (in which the diffraction of a beam through the crystal is assumed to be negligible) one finds that r can be replaced by a ratio of the g-factors used to describe the overlap of a field with its driving polarization [84]. We find that a value $\bar{\sigma}_l = 28\%$ would explain the observed noise level in that experiment. While this value of $\bar{\sigma}_l$ is large, it is also consistent with the value one would calculate to account for the reduced conversion efficiency reported in Ref. [29] with respect to theory.

4.2 Spontaneous Raman scattering

Raman scattering involves the scattering of a photon off an optical phonon in a material to either redshift the photon by creating a phonon (in so-called Stokes scattering) or blueshifting by absorbing a phonon (anti-Stokes scattering). Fig. 4.13 diagrams

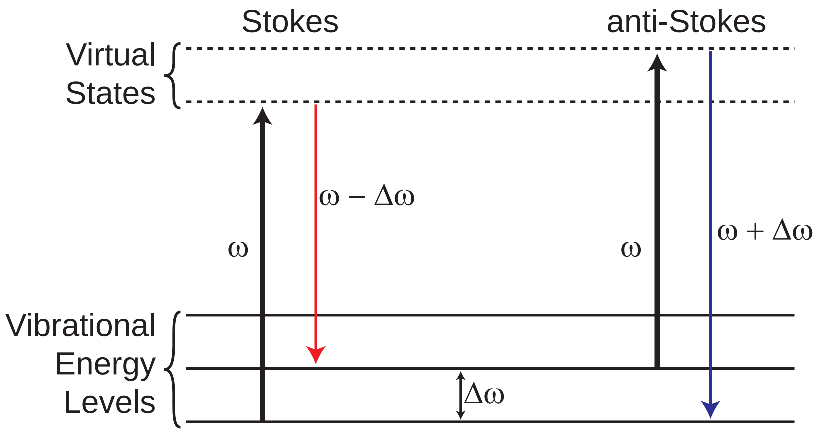

Figure 4.13: Diagram of spontaneous Raman scattering in either the Stokes (in which a photon at frequency ω redshifts to $\omega - \Delta\omega$ via the creation of a phonon of frequency $\Delta\omega$) or anti-Stokes configuration (in which a photon is blueshifted to $\omega + \Delta\omega$ via the annihilation of a phonon).

each of these two processes. Raman scattering was the first inelastic scattering process observed with photons; it was observed by C. V. Raman in 1928 by sending a beam of focused sunlight through a liquid and observing the scattering by eye [85]. Since then, Raman scattering has been used extensively as a material characterization method as the phonon frequencies and polarization response gives a fingerprint of the material.

Raman scattering in crystals has been studied by Loudon [86]. Raman scattering in $LiNbO_3$ appears to have been first observed by Schaufele and Weber in 1966 [87]. Lithium niobate is a trigonal crystal with $3m$ symmetry: the conventional hexagonal unit cell contains 6 formula units [88]. The Raman spectrum has been measured many times, with a focus put on identifying and characterizing the peaks of the Raman spectrum. However, in quantum frequency converters, it seems obvious that Raman peaks should be avoided. To our knowledge, there has not been a detailed investigation of the character of SRS both between and at frequency shifts past the Raman peaks, which we describe in the next section.

4.2.1 Raman spectroscopy of H^+:$LiNbO_3$

We sought a detailed characterization of the Raman scattering behavior of $LiNbO_3$ for frequency shifts away from any of the dominant phonon peaks. In a Raman spectroscopy experiment, the basic quantity measured is the differential scattering cross section $\mathrm{d}\sigma\,/\,\mathrm{d}\Omega$. A Raman spectrometer records a spectrum $S(\Delta f)$, which is a number of photocounts at a frequency difference $\Delta f = f_0 - f_S$, where f_0 is the frequency of the laser excitation and f_S is the Stokes frequency. The measured spectrum and the differential cross section, which can be used to calculate the gain in a stimulated Raman scattering experiment, are related empirically as

$$S(\Delta f) = \left(\frac{\mathrm{d}\sigma}{\mathrm{d}\Omega}\rho_S L_S\right) g_L(\Delta f) N_0\, \Delta\Omega \tag{4.13}$$

where ρ_S is the number density of scatterers, L_S is the length of the scattering volume, N_0 is the number of incident laser photons over the course of the measurement, and $\Delta\Omega$ is the solid angle subtended by the collection optics. These quantities (other than ρ_S which is a material property) depend in detail on the experimental conditions, and can be hard to calibrate accurately. We are primarily interested in the lineshape function $g_L(\Delta f)$, which can be used straightforwardly to compare the Raman scattering rate at different frequency shifts Δf. We have performed Raman spectroscopy experiments on a variety of samples using a WiTec Alpha300 S Raman microscope. The use of a Raman micrsocope rather than a bulk Raman microscopy setup enabled the investigation of the effects of proton doping, which it was thought may alter the Raman spectrum substantially [89].

Initial measurements were of an X-cut $LiNbO_3$ sample. We measured a Raman spectrum in the $x(zz)\bar{x}$ configuration[1], the results of which are shown, in logarithmic units, in Fig. 4.14. Two measurements were taken using a grating with 1800 lines/mm over overlapping frequency ranges, and the background counts from the Peltier-cooled CCD array detector (which were measured to be time invariant to high statistical

---

[1] The notation $a(bc)d$ is commonly used in the Raman scattering literature: a is excitation direction, b and c are the polarizations of the excitation beam and collected signal, and d is the propagation direction of the collected signal. All quantities are defined with respect to the crystal axes.

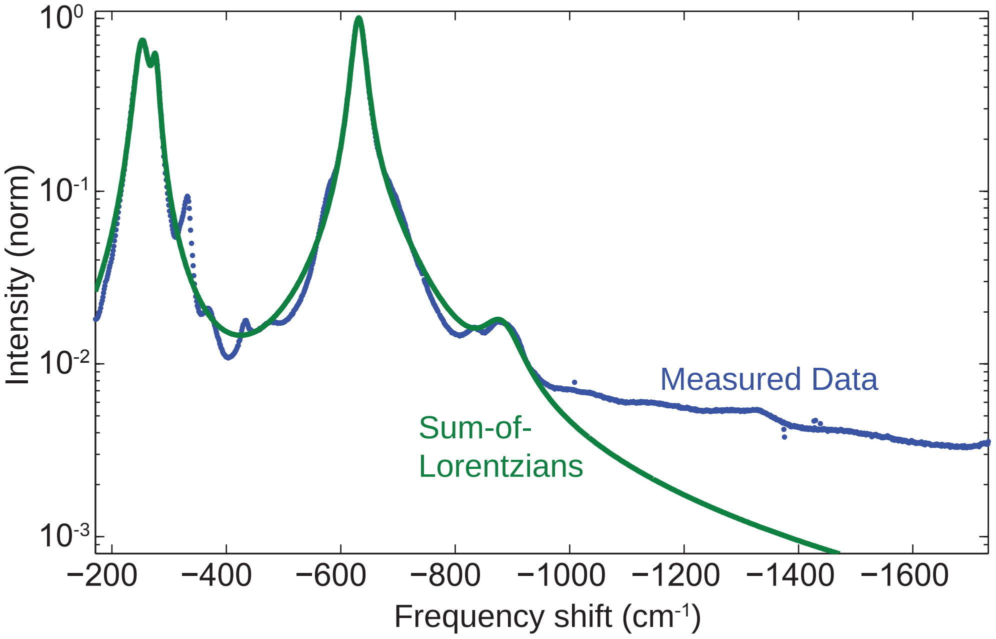

Figure 4.14: Measured Raman spectrum of congruent X-cut LiNbO$_3$ in the $x(zz)\bar{x}$ configuration, and a fit to a sum of Lorentzians as in Eq. (4.14), where the fit parameters are provided in [90].

accuracy) were subtracted. Raman measurements are most frequently shown on linear scales because Raman spectroscopists have been primarily interested in the peak locations. The logarithmic scaling aids in a visual understanding of the unexpectedly slow rate at which the spectrum rolls of at large frequency shifts.

The spectral response of an individual Raman scattering mode is well described by a Lorentzian distribution [12]. It is generally assumed that materials with many Raman-active phonons such as crystals can be well-fit by a sum of Lorentzians [86]. We have fit the complex Raman susceptibility inferred from the measured spectrum via the Kramers-Kronig relation to such a sum of Lorentzians

$$\chi_R(\Delta f) = \sum_{j=0}^{N_L} \frac{a_j}{f_j^2 - (\Delta f)^2 + 2i\gamma_j \Delta f} \tag{4.14}$$

where a table of fit parameters can be found in our publication [91]. In addition to the peaks referenced in [91], we insert the peak at 885 cm^{-1} “by hand” as the fitting routines did not converge properly when it was included. In the vicinity of the peaks, for frequency shifts smaller than approximately $\Delta f < 1000$ cm^{-1}, the superposition of Lorentzians accurately describes the Raman scattering behavior. However, for large frequency shifts $\Delta f > 1000$ cm^{-1}, the measured spectrum $S(\Delta f)$ exceeds the Lorentzian predicition significantly, in an effect we have termed a high-frequency "Raman pedestal," in analogy with the QPM pedestal described in Sec. 4.1.

We next sought to determine the origin of the Raman pedestal. To the best of our knowledge, this large-shift pedestal has not been analyzed elsewhere in the literature on $LiNbO_3$. We initially suspected it was due to the high defect concentration of congruently-melting $LiNbO_3$. When grown from a melt, $LiNbO_3$ does not contain a 1:1 stoichiometric ratio of Li:Nb, but rather has a concentration ratio $[Li]/([Li] + [Nb]) = 0.485$. This non-stoichiometry results in a high degree of crystal disorder due to the large number of point defects [92]. By comparing a congruent crystal to one with stoichiometric composition, it is therefore possible to test this hypothesis. Since stoichiometric $LiNbO_3$ is not readily available, we compared congruent-composition $LiTaO_3$ against stoichiometric $LiTaO_3$. The stoichiometric $LiTaO_3$ showed a similar shelf as congruent $LiTaO_3$, suggesting that disorder is not important to the existence of the shelf. The effects of stoichiometric versus congruent composition were found to be Raman line-narrowing, which has been described in the literature [93, 94], without the addition of a pedestal.

We also suspected the pedestal may be due to the proton exchange process. As discussed in Chapter 3, proton exchange removes Li^+ ions and replaces them with H^+ ions, raising the refractive index for e-polarized light. The Raman scattering strength of $H^+:LiNbO_3$ has been found to be substantially diminished, which partially explains the so-called "dead layer" near the surface of a PE waveguide in which $\chi^{(2)}$ vanishes [89]. We characterized both unannealed and annealed PE planar waveguides formed on both X- and Z-cut substrates, as well as RPE planar waveguides on Z-cut substrates. While we have not endeavored to obtain a detailed picture of the effects of proton doping on Raman behavior, we did not see any qualitative differences in the large-frequency-shift behavior that would indicate that proton exchange is the cause of the Raman pedestal.

In the absence of independent confirmation of the Raman pedestal by direct spectroscopic measurement, measurements of noise behavior in a quantum frequency conversion device can provide indirect insight on this effect. The theory of noise generation by spontaneous Raman scattering is described in the next section and an experiment studying the noise behavior of a long-wavelength-pumped upconversion single-photon detector for the 1.55-μm band is described in Sec 5.3.

4.2.2 Raman noise in QFC devices

Here, we seek to describe the physics of spontaneous Raman scattering in a waveguide geometry that can be used to predict the spectral dependence of noise in a quantum frequency converter in which the strong pump is undergoing Raman scattering. Describing the Raman scattering process using a formalism that includes a Raman susceptibility χ_R has been presented in [12]. We modify that presentation slightly to include the effects an interaction involving only a single spatial mode at each frequency in a more restrictive geometry. An equation for the evolution of photon field envelopes (defined as in Chapter 2) with a laser frequency ω_0 and scattered frequency ω_s, where $\Delta\omega = \omega_s - \omega_0$, is:

$$\frac{\mathrm{d}a_s}{\mathrm{d}z} = -i\frac{3\omega_s Z_0 \chi_R(\Delta\omega)}{4n_s n_L c} P_0 \Theta_R h(\Delta\omega) a_s, \tag{4.15}$$

where we have written the evolution equation in terms of the pump power $P_0 = \hbar\omega_0|a_0|^2$, the Raman overlap integral

$$\Theta_R = \iint |u_0(x,y)|^2 |u_s(x,y)|^2 \,\mathrm{d}x\,\mathrm{d}y, \tag{4.16}$$

and $h(\Delta\omega)$ is a factor that describes the occupation of the relevant phonon modes and has different forms for Stokes and anti-Stokes scattering.

A proper quantum mechanical treatment of Raman scattering (in which both the light field and vibrations are quantized) is required to deduce the form of $h(\Delta\omega)$ and will not be presented here [95]. The quantity $h(\Delta\omega)$ takes into account the Raman signals by summing across all the vibrational energy levels of the oscillating modes in the system. For Stokes and anti-Stokes scattering, respectively, we find

$$h(\Delta\omega < 0) = 1 + \langle n_v(|\Delta\omega|)\rangle \tag{4.17a}$$

$$h(\Delta\omega > 0) = \langle n_v(|\Delta\omega|)\rangle \tag{4.17b}$$

where the quantity $\langle n_v(|\Delta\omega|)\rangle$ is the average excitation of a harmonic oscillator and is obtained via the Boltzmann distribution as

$$\langle n_v(|\Delta\omega|)\rangle = \frac{1}{e^{\hbar|\Delta\omega|/kT} - 1} \tag{4.18}$$

where T is the temperature of the system.

To calculate the spontaneous scattering rate, we define $N_s = |a_s|^2$ and notice

$$\frac{\mathrm{d}N_s}{\mathrm{d}z} = a_s^* \frac{\mathrm{d}a_s}{\mathrm{d}z} + a_s \frac{\mathrm{d}a_s^*}{\mathrm{d}z}. \tag{4.19}$$

Combining Eq. (4.15) and (4.19), and inserting an "extra photon" in the usual way to describe spontaneous emission processes, we are led to a photon-number evolution equation

$$\frac{\mathrm{d}N_s}{\mathrm{d}z} = \frac{3\omega_s Z_0}{2n_s n_0 c}\chi_{R,i}(\Delta\omega)h(\Delta\omega)P_0\Theta_R(N_s + 1), \tag{4.20}$$

where $\chi_{R,i}$ is the imaginary component of the full complex Raman susceptibility χ_R. To calculate the spontaneous scattering rate, we assume $N_s(0) \ll 1$ and find, after propagation through a device of length L, a noise-photon spectral density

$$\frac{\mathrm{d}N_s}{\mathrm{d}\lambda} = \frac{6\pi^2 c Z_0 P_0 h(\Delta\omega)\Theta_R \chi_{R,i}(\Delta\omega)L}{\lambda_s^3 n_s n_0}. \tag{4.21}$$

Evaluating the spontaneous scattering rate $\mathrm{d}N_s\,/\,\mathrm{d}\lambda$ as a function of $\Delta\omega$ for a pump power $P_p = 100$ mW (assuming a pump wavelength $\lambda_s = 1.55$ μm) and a device length $L = 5$ cm gives the results shown in Fig. 4.15. The curves in Fig. 4.15 are calculated using the measured Raman spectra described in Sec. 4.2.1 for large frequency shifts. We were unable to measure the Raman scattering signal for frequency shifts smaller than approximately 200 cm^{-1} due to the limitations of the notch filter used in the

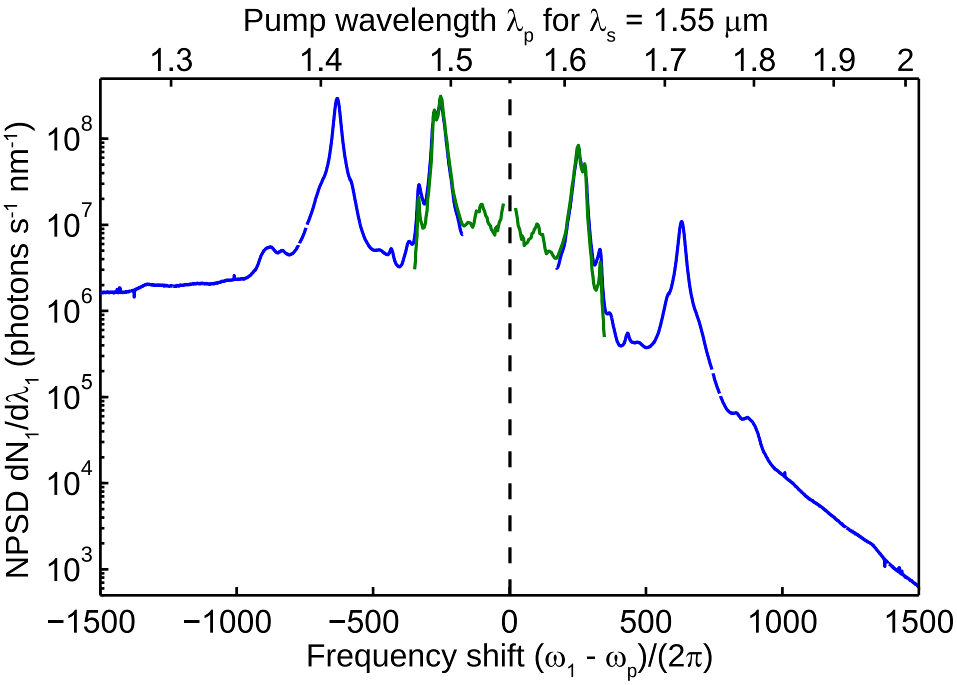

Figure 4.15: Spontaneous Raman scattering noise photon spectral density calculated from measured Raman spectrum, plotted against signal–pump frequency shift $\Delta\omega = \omega_1 - \omega_p$ and equivalently against the pump wavelength λ_p used for an input signal wavelength λ_1 in an upconverter. Results calculated from our Raman spectroscopy measurements are plotted in blue, and the low-frequency-shift data plotted in green are taken from Ref. [96].

Raman microscope. The low-frequency-shift data of Fig. 4.15, plotted in green, have been copied from the work of Surovtsev *et al.* and have been adjusted to give the same Raman signal for the 252-cm^{-1} peak [96].

The data of Fig. 4.15 clearly show major difference between Stokes ($\Delta\omega < 0$) and anti-Stokes ($\Delta\omega > 0$) scattering. As the pump frequency becomes substantially lower than the signal (corresponding to $\Delta\omega$ increasing), or correspondingly a very long pump wavelength, anti-Stokes Raman scattering decreases dramatically. The effects of anti-Stokes Raman scattering on an upconversion single-photon detector for 1.55-μm-band signals will be discussed in Chapter 5.

4.3 Design implications

In the previous two sections we have discussed the two primary noise sources in quantum frequency conversion devices. To the best of our knowledge, no other spontaneous scattering processes have been found to play a major role in the noise performance of QFC devices. Typical QPM-grating disorder parameters $\bar{\sigma}_l/l \approx 10\%$ yield NPSDs that are in general too high for useful QFC systems. This fact alone basically eliminates the possibility of using pump wavelengths λ_p shorter than the input signal λ_1. The analysis of SRS from the previous section shows that Raman scattering is a major noise source (in the Stokes configuration) even for pump–signal frequency differences well past the main Raman peak at 632 cm^{-1}. Anti-Stokes scattering is found to be a significant noise source for $0 < \Delta\omega/2\pi \lesssim 1000$ cm^{-1}. However, due to its dependence on the Boltzmann ratio, anti-Stokes scattering is reduced significantly for large positive $\Delta\omega$.

Thus, in most situations, very low noise performance will only be achieved when $\Delta\omega \gtrsim 1500$ cm^{-1}. Such a system, for downconversion of single-photons from quantum dots, will be described in Chapter 6. Another approach for achieving low-noise performance, however, is optical filtering. In most circumstances, an input signal will be spectrally narrow compared to either the acceptance bandwidth of the converter or any "naïve" optical filtering at the output. We describe one experiment in Sec. 7.2 in which, through using an optical filter substantially narrower than the upconversion acceptance bandwidth, the noise can be reduced significantly (by a factor of about 50) compared with the naïve filtering case.

We also note that for spontaneous scattering processes, the signal-to-noise ratio is generally improved with longer devices. As the conversion efficiency of a device scales as L^2 while the generation of noise photons scales as L, this behavior is understood quite simply. We have not explored the use of devices longer than approximately 6.7-cm, roughly the maximum chip length available by processing 76-mm (3") wafers. In future work, the improved efficiency from fabricating on 4" wafers may enable further reduction of noise.

Chapter 5

Upconversion-assisted single-photon detectors

Single-photon detectors are important in a variety of applications, ranging from biochemistry to sensing to communications. This chapter presents work on applications of quantum frequency converters towards improving single-photon detectors based on avalanche photodiodes (APDs). Our work on a long-wavelength pump source for upconversion detectors (based on a monolithic PPLN optical parametric oscillator (OPO)) was published in [97], and the performance of a 1.55-μm-band upconversion detector was published in [67].

5.1 Single-photon detection with avalanche photodiodes

The objective of a single-photon detector (SPD) is to produce a macroscopic electrical pulse upon the absorption of a single optical photon. Photons of visible or near-IR frequency have energies in the range of 10^{-19} J (0.1 aJ), so the devices must be extremely sensitive to incoming optical radiation. A recent review due to Hadfield describes the state-of-the art for SPDs across a wide range of device technologies [22].

The three most important performance parameters of single photon detectors are the photon detection efficiency (PDE) η_ν, the dark-count rate (DCR) D, and the timing jitter Δt. The PDE is simply the probability that an incoming single photon will register an output pulse, which is a function of the wavelength of the incoming photon. The DCR is the rate at which the detector produces output pulses when it is known that there are no incident photons. The timing jitter describes the spread of arrival times of the electrical pulses for a train of well-timed optical pulses. Additionally, the spectral range of a SPD is of critical importance as well, as it determines which wavelengths can be used in system applications. Two other important parameters, which we will not discuss here, are the ability to resolve photon number (which can be important for linear-optical quantum computation [98]), and the dead time τ_D (which will be discussed in Chapter 7) which determines the maximal flux of incident photons before the detector saturates.

The first widely used SPDs were based on photomultiplier tubes, which are still the primary detectors used for the UV spectral range. The most established detectors for the visible and near-IR are based on semiconductor avalanche photodiodes. Additional emerging detector technologies are based on either superconducting nanowires [99] or superconducting transition-edge sensors [100], but both of these technologies require cryogens and are viewed to be somewhat impractical for field use in, for example, quantum key distribution systems. Here, we focus on detection with APDs.

Avalanche photodiode SPDs consist of a semiconductor p–n (or p–i–n) junction reverse-biased above the breakdown voltage, in so-called “Geiger mode” operation. Photocarriers produced by the absorption of a photon undergo avalanche gain triggering macroscopic breakdown of the junction. Following the avalanche, the current must be stopped either through the use of active or passive quenching schemes [101, 102]. There are two commercial device types based on Si, which are referred to as “thick-junction” or “thin-junction” types. The thick-junction detectors are optimized for the highest PDE and have a thick active region, which results in a large timing jitter due to variability in the carrier extraction time depending on where in the junction the absorption event took place [103]. The performance of these detectors with respect to recent reports on InGaAs APDs is summarized in Table 5.1.

The primary drawback with InGaAs APDs is the effect of afterpulsing. After the

Table 5.1: Summary of avalanche photodiode single-photon detector performance for both the Si and InGaAs material systems.

	Si (thick)	Si (thin)	InGaAs (Self-differencing [104])	InGaAs (Free-running [105])
Peak PDE (%)	70	49	10	4.5
Spectral range (μm)	0.4–1.0	0.4–0.8	1.1–1.6	1.1-1.6
Dark-count rate (s^{-1})	100	20	1.6×10^4	5×10^4
Timing jitter Δt (ps)	400	35	55	450
Max rate τ_D^{-1} (MHz)	10	10	100	1.1

registration of an avalanche event, some portion of the photocarriers occupy intraband trap states, and the decay of these trap states can excite additional avalanches [106]. The primary way around this effect is to gate the detector; that is, to bias in Geiger mode only for a short duration (typically 0.5 to 10 ns), followed by turning off the detector such that afterpulses cannot undergo avalanche gain. Researchers have developed sophisticated electronic gating and quenching schemes, including sine-wave biasing [107] and self-differencing [104] which enable high clock rates and improved performance over the initial generation of devices. As material quality has improved, free-running InGaAs APDs have been developed, but, as is seen in Table 5.1, the DCR is still very high.

The idea of upconversion detection is that if a single photon with an energy lower than the Si bandgap (wavelength longer than 1 μm) can be upconverted with high efficiency to an energy larger than the Si bandgap, one could then combine the efficient upconverter with a Si APD for improved single-photon detection. A summary of experimental achievements in upconversion SP detection has been given in Chapter 2.

5.2 Long-wavelength pump source based on monolithic PPLN OPO

Upconversion single-photon detection is only a viable technology if the upconversion can be done with little added noise. Therefore, as discussed in Chapter 4, a pump

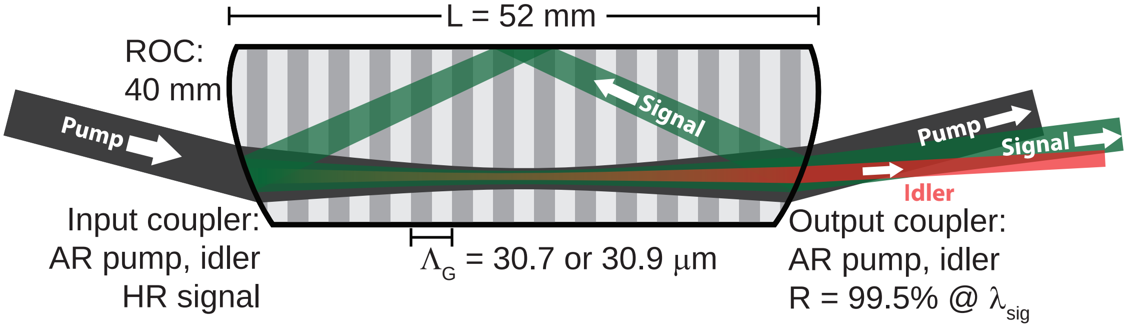

Figure 5.1: Schematic diagram of monolithic PPLN OPO used for long-wavelength-pumped 1.5-μm upconversion single photon detector. The OPO was pumped at 1064 nm by a Yb:fiber oscillator and amplifier.

wavelength λ_p substantially longer than the input signal wavelength λ_1 must be used. For input signals in the 1.55-μm band, this therefore means a pump wavelength $\lambda_p > 1.8$ μm, which is in a spectral region where commercial laser sources with the desired properties (tunable, single-frequency, output power up to 1 W) are not available.

We therefore developed a pump source for long-wavelength-pumped quantum frequency converters based on a monolithic PPLN optical parametric oscillator (OPO) [97]. In our OPO, the path of the resonant signal wave is entirely within the PPLN QPM grating [108]. This approach has several advantages including mechanical and thermal stability, simplicity of operation and alignment, and the possibility of low losses since the monolithic resonator has no lossy internal interfaces, and, importantly for mid-IR operation, has no (possibly absorptive) air path. This monolithic configuration was accomplished by applying an angled spherical polish and a highly reflective (HR) coating to two of the facets of the PPLN crystal, and using total internal reflection on one side of the crystal to form a closed resonant path [108], see Fig. (5.1). To ensure that the resonator axis was within the 1-mm-thick crystal aperture, the angles of each curved facet was tested optically during the OPO fabrication process via a reflection measurement with a HeNe laser.

In our OPO, the mirror curvature $R = 40$ mm, and the crystal has dimensions 52×5×1 mm. The PPLN crystals were poled by Crystal Technology, Inc., with a

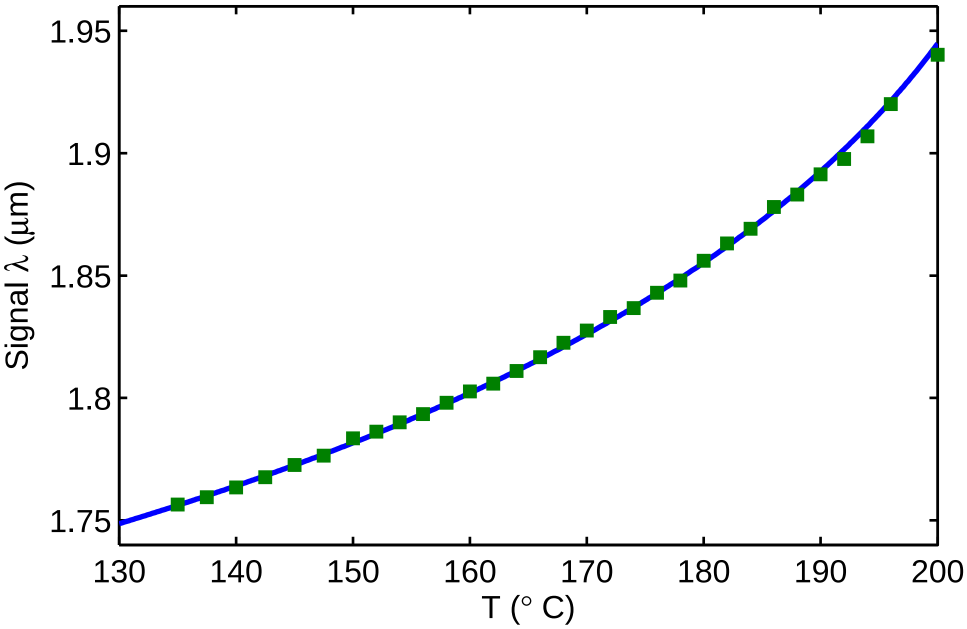

Figure 5.2: Monolithic OPO signal wavelength versus temperature (squares) and fit to $LiNbO_3$ Sellmeier equation [109].

QPM period of $\Lambda_G = 30.9$ μm, and were fabricated into resonators by the Ginzton Lab Crystal Shop. We resonate the short-wave signal, which is tuned around 1.8 μm. The coating for the curved input crystal facet is highly reflective (HR) between 1.7 and 2.0 μm (reflectance $R > 99.9\%$), highly transmissive (HT) between 2.4 and 2.9 μm ($R < 5\%$), and has $R \approx 5\%$ at 1.064 μm. The coating for the output facet has $R \approx 99.5\%$ between 1.7 and 1.9 μm, $R < 5\%$ between 2.4 and 2.9 μm, and $R \approx 5\%$ at 1.064 μm. The focusing parameter is defined as $\xi_j = L/(k_j w_{j0}^2)$ ($j \in \{i, s, p\}$), where L is the QPM grating length, $k_j = 2\pi n_j/\lambda_j$ is the wave-vector at wavelength λ_j , and w_{j0} is the $1/e^2$ intensity radius of wave j at the beam waist. We focused the pump to slightly looser than confocal ($\xi_p \approx 0.9$), while the cold-cavity signal mode defined by the geometry of the PPLN crystal is focused slightly tighter than confocal ($\xi_s \approx 1.3$).

A complete description of the measurements of the performance of the monolithic OPO has been given in [97]. The OPO had a threshold pump power of approximately 1 W, and at a maximum pump power of 7.0 W, we observed a signal output power of 0.98 W with a pump depletion of 80%. Here, we provide data on the tuning of the OPO signal wavelength λ_s versus the device temperature T. Our results are shown in Fig. 5.2 (squares) along with a fit to the dispersion relation of $LiNbO_3$ (solid) [109]. The fit includes a +3° C oven temperature offset to match theory. By tuning the device temperature from 135 to 200° C, the signal wavelength tuned from 1.76 to 1.94 μm. We used a Michelson-interferometer-based wavelength meter and optical spectrum analyzer, which gave an instrument-limited linewidth of 0.04 nm (3.66 GHz). This linewidth is approximately 2.7 times the free-spectral range of the OPO cavity (1.34 GHz). However, we are confident that the OPO runs in a single longitudinal mode at pump powers near threshold. Single-mode operation can be inferred from the high signal depletion we measured in the upconversion detector described in the next section; if multiple longitudinal modes were oscillating, mode beating would cause the observed depletion to reach a maximum value of approximately 5 dB [110], whereas we observed a signal depletion of 41 dB.

We note the device design was suboptimal in that the cavity was somewhat undercoupled compared to the losses. Based on our estimate of the absorption losses, the available pump power of 8 W, and 90% pump depletion, an output coupler of around 4% would lead to optimal signal output power of approximately 3.4 W. Due to the undercoupling, we observed several additional effects which caused changes to the signal power and its spectrum. These effects included an optical parametric amplification process involving a backwards-propagating THz-frequency wave, as well as stimulated Raman scattering of the intracavity signal. These effects (discussed in detail in [97], in addition to an intrinsic modulation instability of singly resonant OPOs [111], resulted in our needing to pump the OPO close to threshold ($< 1.5\times$) in order for the OPO to run stably in a single line.

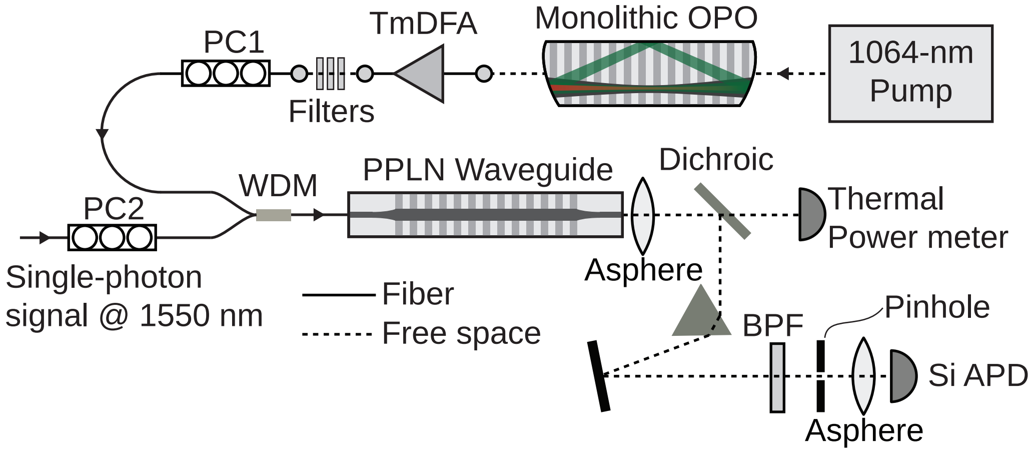
TmDFA
Monolithic OPO
PC1
1064-nm Pump
Filters
PPLN Waveguide
Dichroic
WDM
PC2
Thermal Power meter
Single-photon signal @ 1550 nm
Fiber
Free space
Asphere
Pinhole
BPF
Si APD
Asphere

Figure 5.3: Experimental setup for demonstration of long-wavelength-pumped upconversion single-photon detection. The single-photon-level signal from a tunable C-band ECDL is combined with the long-wavelength pump in an off-chip WDM coupler. The upconverted signal is outcoupled into free space, is filtered using a dichroic mirror (DM), prism, and band-pass filter (BPF), and focused onto a Si APD.

5.3 Long-wavelength-pumped upconversion detector at 1.55 μm

We developed an upconversion single-photon detector for the 1.5-μm telecommunications band based on an RPE PPLN waveguide. In this section, we first describe the device and its classical-signal characterization, followed by a summary of the upconversion detector system performance and observed noise properties. The system and its performance have been published in [67].

5.3.1 Experimental setup and characterization

The experimental setup for our long-wavelength-pumped upconversion detector is shown in Fig. 5.3. We fabricated RPE PPLN waveguides designed for sum-frequency generation of an 1850-nm pump and 1550-nm signal. The waveguides had total length $L = 52$ mm, and were fabricated with a poling period $\Lambda_G = 18.4$ or 18.8 μm. The waveguides had at their inputs spatial-mode filters designed to match the mode size of SMF-28 optical fiber, and were fiber-pigtailed with coupling losses of approximately

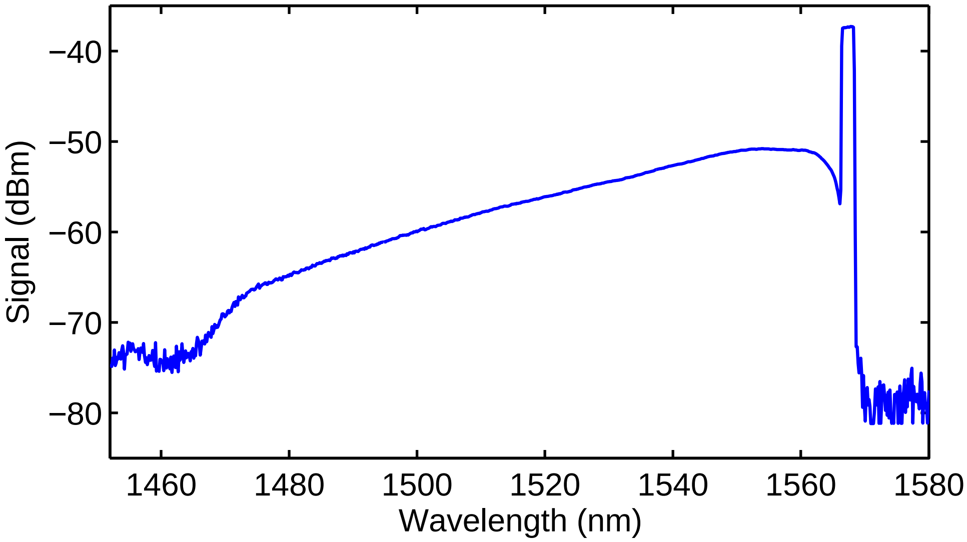

Figure 5.4: TmDFA noise spectrum between 1450 and 1580 nm, measured with an optical spectrum analyzer with a resolution bandwidth of 2 nm, showing the TmDFA pump line at 1567 nm and shelf of spontaneous emission down to approximately 1470 nm.

0.8 dB. We measured propagation losses below 0.2 dB cm^{-1} using the Fabry-Perot technique (see Sec. 3.3). The waveguide facets were flat-polished and antireflection coated to eliminate interference effects and improve the sum-frequency (SF) throughput. The waveguides were held in a temperature-controlled oven.

The tunable pump source we used for this experiment was based on the monolithic PPLN optical parametric oscillator described in the previous section. For stability, we operated the OPO close to threshold, and used the narrow linewidth signal wave to seed a Tm-doped fiber amplifier (TmDFA, IPG Photonics) which could produce up to 800 mW of output power. Before inserting the long-pass filters into the pump path, a strong noise signal overwhelmed the upconversion of the signal light, saturating the Si APD. We investigated the noise spectrum of the TmDFA by separating the long- and short-wavelength components using a C/L-band micro-optic WDM and coupling the C-band components into an optical spectrum analyzer. The TmDFA noise spectrum is shown in Fig. 5.4 for a 3-mW seed at 1800 nm and output power of 700 mW. The TmDFA is pumped by an Er:fiber laser at 1567 nm [112], but a shelf of spontaneous emission noise is observed at all wavelengths down to approximately 1470 nm. Another popular pump scheme for Tm lasers is to pump at 790 nm; a subsequent cross-relaxation process enables the generation of two laser photons for each pump photon. Investigation of cross-relaxation Tm lasers also shows C-band spontaneous emission [113]. For low-noise upconversion, the pump light and spontaneous emission must be filtered. Previous work on upconversion using Tm laser systems used fiber-optic WDMs as filters [32]. Here, we use a series of three free-space long-pass filters placed into a fiber bench to achieve the very high extinction (> 100 dB) needed to eliminate noise due to SFG of noise photons due to pump processes with the strong long-wavelength pump. With our devices tuned to a phasematched wavelength of 1555 nm, the phasematching acceptance bandwidth of the upconverter is itself a very effective filter of the 1567-nm TmDFA pump; we observe 50 dB rejection of upconversion of the 1567-nm noise photons versus 1555 nm signal photons, which is consistent with a prediction based on a domain-disorder-induced QPM pedestal [75].

The 1550-nm-band signal was produced by a tunable external-cavity diode laser and a series of calibrated attenuators. As PPLN RPE waveguides support only TM-polarized modes, polarization controllers were used to rotate the polarization of both the signal and pump beams. If necessary, polarization-independent upconversion detectors as in [114] could be built in the future. The long-wavelength pump and single-photon-level signal were combined off-chip in a micro-optic C/L-band WDM (Oplink) found to have low insertion loss for both the signal and pump wavelengths. For measurements of the detection efficiency, the signal level was set to 10^6 photons s^{-1} at the entrance of the WDM. The upconverted SF radiation at ω_2 was collected by an aspheric lens ($f = 8$ mm). The pump and signal were separated from the SF by a dichroic mirror and the pump power was monitored using a thermal power meter. The upconverted output was further filtered using a Brewster-angle prism and 50-nm-bandwidth optical bandpass filter to reject parasitic second harmonic radiation of the strong pump. The SF light was focused onto a Si single-photon-counting module (Perkin-Elmer SPCM-AQR-13). The transmission of the optical system between the waveguide output facet and the SPCM was 92%.

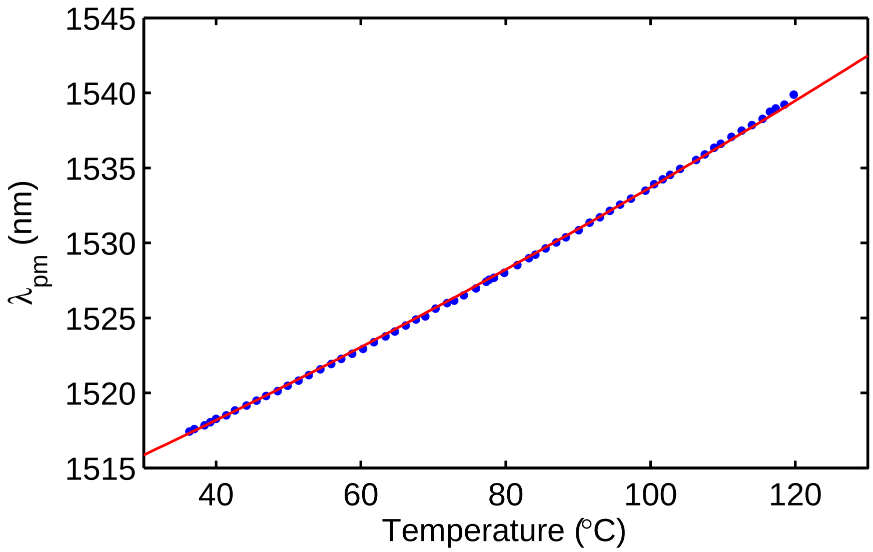

Figure 5.5: Measured signal-wavelength tuning (dots) and calculation from $LiNbO_3$ Sellmeier coefficients (solid), where $\lambda_p = 1800.0$ nm and $\Lambda_G = 18.4$ μm.

We first characterized the phasematching of the upconversion waveguides. The pump wavelength λ_p was fixed at 1800 nm and the signal wavelength was swept. For the device used in subsequent experiments with $\Lambda_G = 18.8$ μm, we observed a phasematching FWHM of 0.57 nm, which matches the expected width calculated from the $LiNbO_3$ dispersion relations [109] and the 47-mm QPM grating length. We also measured the temperature tuning of the phasematching, which is shown in Fig. 5.5. Experimental data for a device with $\Lambda_G = 18.4$ μm are represented as dots and the solid curve is a theoretical calculation based on a temperature-dependent Sellmeier relation for $LiNbO_3$ [109]. The phasematching temperature tuning rate for $\lambda_p = 1800$ nm was 0.27 nm/°C.

We measured the conversion efficiency of the waveguide as a function of both pump power P_p and signal wavelength λ_1 for a constant classical-level input signal power of 20 μW; the results are shown in Fig. 5.6(a). We reach a maximum internal conversion efficiency η of 86% which is consistent with our observed propagation losses of 0.17 dB cm^{-1} at λ_1 and a value of 0.1 dB cm^{-1} at λ_2 and our observed 41 dB (99.99%) signal depletion. Measurements at 24 pump powers between 0 and 350 mW

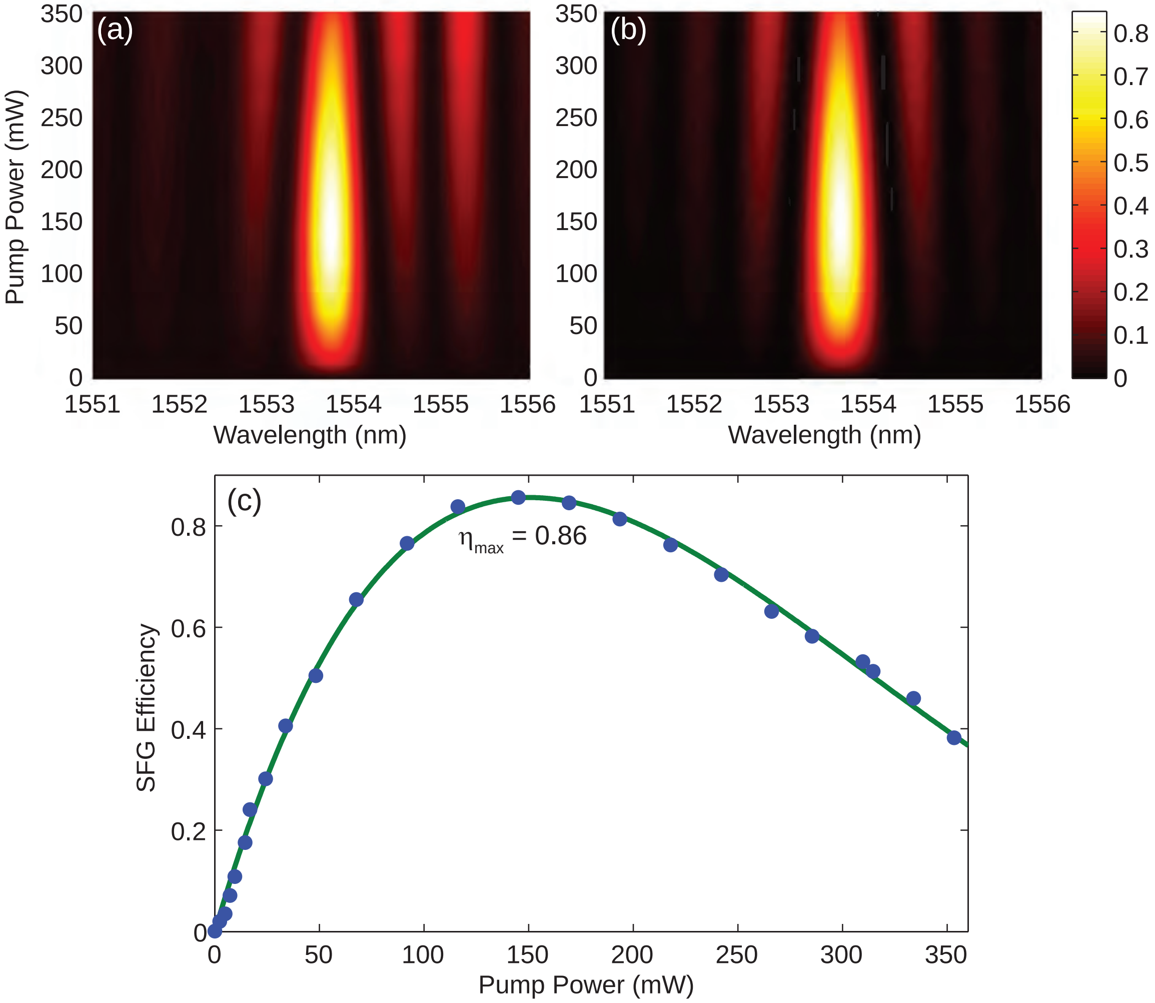

Figure 5.6: (a) Experimentally observed and (b) numerically predicted conversion efficiency versus pump power and signal wavelength. Simulation parameters: α_1 (α_2) = 0.17 (0.1) dB cm^{-1}, and $P_{\max}$ = 151 mW; (c) internal conversion efficiency of PPLN waveguide ($\lambda_1 = 1554$ nm, $\lambda_2 = 834$ nm).

have been interpolated to provide a smooth plot. Figure 5.6(b) shows a theoretical prediction of the internal conversion efficiency calculated by numerically integrating the coupled-wave equations for SFG (as in Chapter 2) with our experimental parameters. There is good agreement of the major features and the observed theoretical and experimental conversion efficiencies match very well. Figure 5.6(c) shows a slice of the two-dimensional data at the QPM peak. The data (squares) are well fit by Eq. (2.19), with $\eta_{\text{nor}} = 68\%\ \text{W}^{-1}\ \text{cm}^{-2}$ and thus $P_{\max} = 151$ mW.

5.3.2 Single-photon performance

We next characterized the performance of the detection system by attenuating the signal laser to a level of 10^6 photons s^{-1} at the input of the WDM using a series of calibrated fiber-optic attenuators. After blocking the pump noise with long-pass filters, we could measure the photon detection efficiency (PDE) and noise count rate (NCR) of our upconversion detector. Measurements were made using several pump wavelengths between 1796 and 1859 nm. A plot of the PDE (left axes) and NCR (right axes) versus pump power for a pump wavelength $\lambda_p = 1810$ nm is shown in Fig. 5.7. At $P_p = P_{\max} = 151$ mW we attain a maximum PDE of 37%. The measured conversion efficiency matches our expected conversion efficiency by combining the losses of each component, as shown in Table 5.2. While the SPCM datasheet quotes an expected PDE of 55% at 834 nm, we find that a value of 58% is needed to explain our observed system detection efficiency. With technologically feasible improvements to the setup and waveguide, and a detector with PDE $\eta_\nu = 58\%$, we should be able to obtain an internal conversion efficiency of 94% and a maximum PDE of 48%.

As seen in Fig. 5.7, there are still appreciable noise counts (approximately 7×10^3 counts/s) for $\lambda_p = 1810$ nm and $P_p = P_{\max}$. This result contrasts with earlier work involving an 1810-nm-pumped upconversion detector [32]. In [32], there was insufficient pump power (only 60 mW was coupled into the waveguide) to reach $P_{\max}$, and, perhaps more importantly, the SFG output was passed through a monochromator before being routed to the SPCM, significantly narrowing the spectrum of detected photons. We estimate the bandwidth of our output filtering system to be approximately

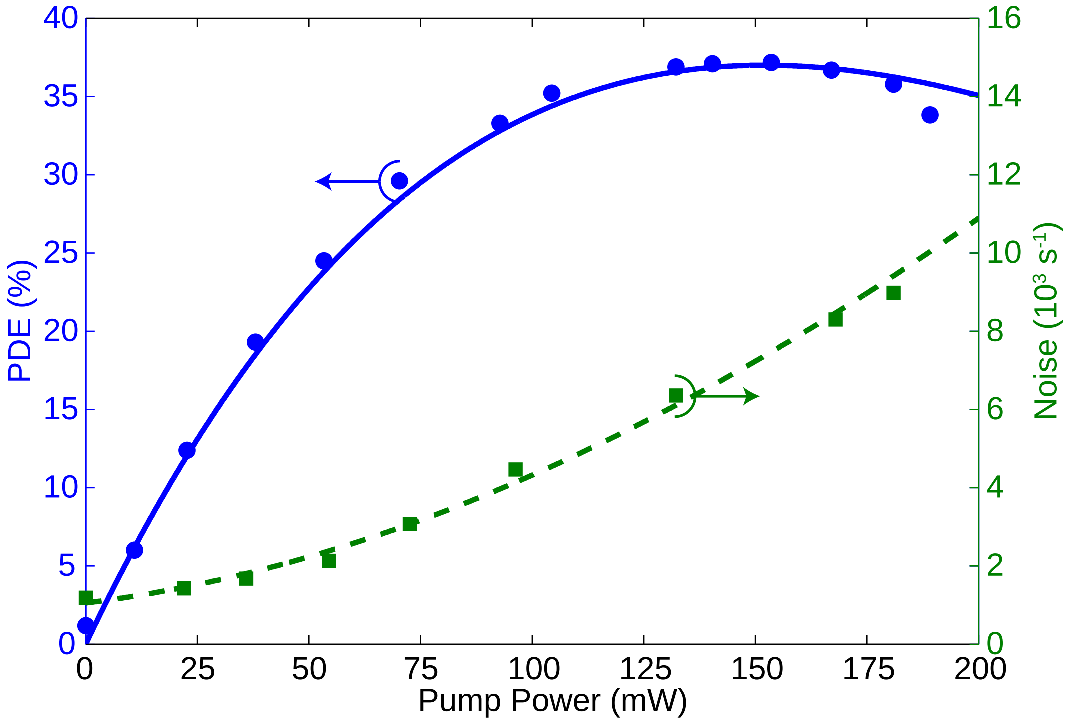

Figure 5.7: Photon detection efficiency (PDE, circles) and noise count rate (squares) of upconversion SPD with $\lambda_p = 1.81$ μm. Solid blue is a fit to PDE $= \eta_{\max} \sin^2\left(\pi/2\sqrt{P_p/P_{\max}}\right)$, where $\eta_{\max} = 37\%$ and $P_{\max} = 151$ mW. The noise count rate at peak PDE is approximately 7×10^3 counts/s.

20 nm. This was narrow enough to reject any pump second-harmonic generation, but not narrow enough to filter the upconverted signal (with linewidth likely well below 1 GHz) from any upconverted SRS photons (which will fill the 74-GHz (0.57-nm) upconversion acceptance bandwidth).

In Sec. 4.2, we discussed noise in QFC devices due to spontaneous Raman scattering (SRS). We varied the pump wavelength λ_p between 1796 and 1859 nm, while keeping the device temperature constant at $T = 30$ °C. As a result, the signal wavelength tuned from $\lambda_1 = 1557$ to 1511 nm. For each pump–signal frequency difference $\Delta f = (\omega_1 - \omega_p)/2\pi$, we measured the PDE and NCR of the SPD as a function of P_p. Fig. 5.8 shows a plot of the NCR at $P_p = P_{\max}$ for each Δf. We observe a significant decrease in the NCR as the frequency difference Δf grows. For the largest frequency

Table 5.2: Loss and transmission of upconversion detector components. The column with feasible transmission values is based on idealized optical components and improved waveguides with pigtailing losses of 0.5 dB and propagation losses of 0.1 dB cm^{-1}.

Component	Loss (dB)	Transmission	Feasible T
Wavelength combiner	0.45	0.97	0.99
Fiber pigtailing	0.8	0.83	0.9
Conversion efficiency	0.66	0.86	0.94
Optical system	0.36	0.92	0.99
SPCM PDE	2.4	0.58	η_ν
	Total:	0.37	$0.83\eta_\nu$

separation $\Delta f = 1241\ \text{cm}^{-1}$, our noise count rate was approximately 1000 counts/s. In Fig. 5.8, the intrinsic DCR of the SPD used in this experiment, 500 counts/s, was subtracted, and as such, the experimental data represent only the noise counts due to spontaneous scattering or other technical noise sources such as stray light.

The solid curve in Fig. 5.8 is a calculation of the expected NCR due to spontaneous Raman scattering rate for this system. The agreement of experimental and theoretical results is quite strong. The calculation uses the Raman susceptibility (imaginary component) $\chi_{R,i}$ given in [91], uses a Raman effective area $A_{\text{eff,R}} = 20\ \mu\text{m}^2$ (calculated using the modal fields from RPE waveguide simulations and assumed to be constant over the spectral range shown in Fig. 5.8, valid to within 5%), and uses a pump power $P_p = P_{\max} = 151$ mW. The only unknown in the calculation was the effective conversion efficiency of the Raman noise photons. The value used in the calculation in Fig. 5.8 was 72%. This value is higher than the expected conversion efficiency, which was calculated to be approximately 40–50% by a semiclassical simulation of upconversion of noise photons generated in a distributed fashion across the device. This is perhaps unsurprising, as it is known that spontaneous Raman scattering in the input fiber is also a contributing source of noise photons for upconversion detectors [30].

The noise performance of the 1.5-μm SPD could be improved using two major techniques. The first technique is the reduction of the device temperature. As discussed in Sec. 4.2, anti-Stokes Raman scattering requires thermally excited phonons

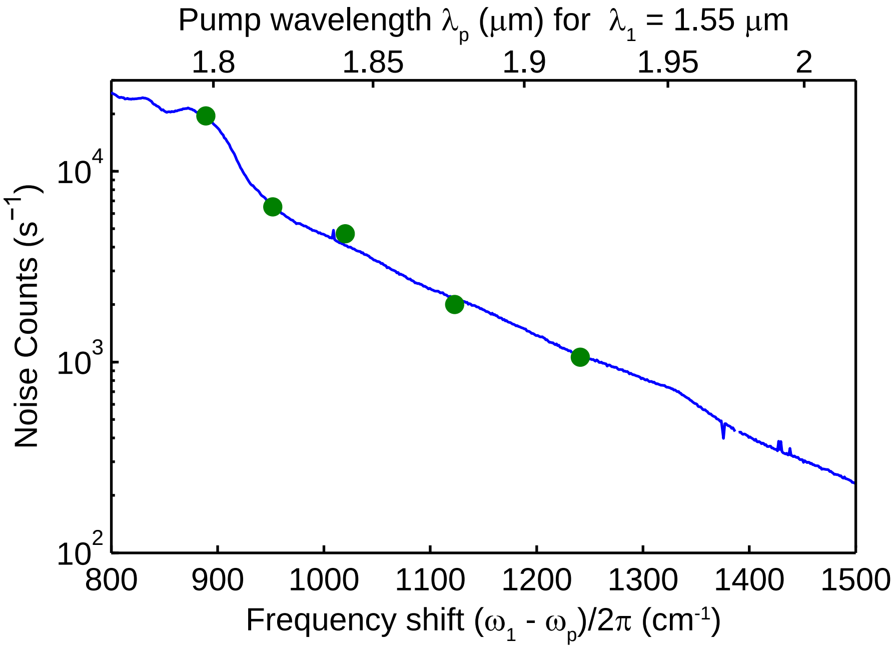

Figure 5.8: Noise count rate of 1.5-μm upconversion SPD versus pump–signal frequency difference $(\omega_1 - \omega_p)/2\pi$ and, equivalently, pump wavelength λ_p needed for a 1.55-μm signal (dots). The blue curve is a calculation of the expected noise-count rate based on known $LiNbO_3$ material properties (see Sec. 4.2) and system parameters.

to be present in the substrate. The Boltzmann factor $\exp(-\hbar\Delta\omega/kT)$ describing this thermal population decreases as T is reduced. For this experiment, the device operated at a temperature of 30° C. With a reduction of the device temperature to $-50°$ C, the noise count rate would be reduced by a factor of 8, to a level roughly equivalent to specified DCRs on high quality thick-junction Si APDs.

The second technique by which the noise could be further reduced is spectral filtering. We note that in our experiment no special effort was made to spectrally filter the upconverted signal beyond rejection of parasitic pump SHG. In an earlier experiment demonstrating low-noise upconversion detection pumped at 1810 nm, noise performance near the DCR of the SPD was achieved by filtering the upconverted light using a monochromator, at significant expense to the system throughput [32]. In most applications, the signal of interest will have substantially smaller bandwidth than the acceptance bandwidth of the upconverter (74 GHz (0.57 nm) for 5-cm-long

RPE PPLN waveguides at 1.55 μm). Because upconverted SRS noise will fill the acceptance bandwidth while the signal will presumably be narrowband, the noise can be significantly reduced by spectral filtering. High-diffraction-efficiency holographic gratings with minimal losses have been used as post-upconversion filters in a recent publication [42]. In Chapter 7, we will discuss the use of a volume Bragg grating filter, which was able to reduce the noise in a 1.5-μm-pumped upconversion SPD for signals at 1.3 μm to a level of approximately 500 counts/s, which is to our knowledge the lowest value reported for these wavelengths.

5.4 Upconversion detection of 1-μm radiation

It is expected that for very large pump-signal frequency differences Δf the noise-count rate should decrease due to the lower thermal occupation ratio for Raman phonons. We demonstrated a low-noise upconversion single-photon detector for the 1-μm spectral region through the use of a 1.5-μm-band pump.

Single-photon detectors for the 1-μm spectral band are in an awkward position between the regimes of applicability of direct detection via either Si or InGaAs APDs. However, they are important for several applications. Although they would have natural applicability in remote sensing (due to the prevalence of 1-μm lasers for these systems), we constructed a 1-μm upconversion detector for use in an experiment designed to demonstrate the feasibility of P neutral-donor bound excitons in Si as a platform for quantum computation [115].

Our 1-μm upconversion SPD was based on a 6.7-cm-long RPE PPLN waveguide with a poling period $\Lambda_G = 10.22$ μm. The primary spectral range of interest was near 1080 nm, but by a combination of temperature tuning (between 30 and 120° C) and pump wavelength tuning (between 1.53 and 1.57 μm) we demonstrated spectral coverage between 1053 and 1087 nm. The device achieved a maximum depletion of approximately 20 dB, most likely limited by higher-order spatial mode content at λ_1 as no directional coupler was used at the device input. Propagation losses at 1.55 μm were measured to be 0.12 dB/cm. The maximum internal conversion efficiency was 81%, at a pump power $P_p = P_{\max} \approx 50$ mW. $P_{\max}$ was substantially lower than

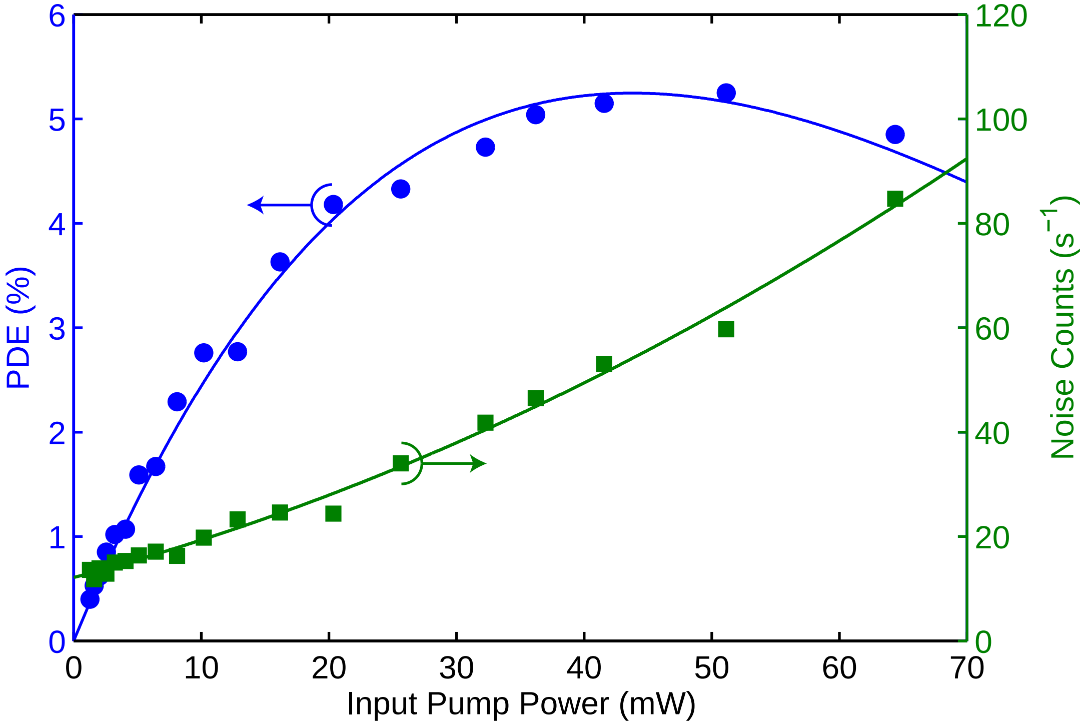

Figure 5.9: Measured system photon detection efficiency (circles) and noise count rate (squares) for upconversion SPD with $\lambda_p = 1.54$ μm and $\lambda_1 = 1078$ nm, showing very low noise counts due to a large pump–signal frequency difference.

for the 1.5-μm upconversion detector discussed above due to both the longer device length and the scaling of the normalized efficiency discussed in Chapter 2 with optical frequencies.

We constructed an upconversion SPD using a similar setup to that shown in Fig. 5.3, where in this case the C-band pump radiation was produced by a tunable telecom-band ECDL and an Erbium-doped fiber amplifier (EDFA). The EDFA had spectral components of its emission in the range of 1.0 to 1.1 μm which initially dominated the noise performance of the system. A tunable band-pass filter (bandwidth 0.25 nm) and two fiber-optic WDMs were used to remove the 1-μm-band spectral components of the EDFA emission before combining the pump with the signal radiation in an off-chip WDM. The target radiation at $\lambda_2 \approx 630$ nm was filtered and routed to a Si APD for detection.

System performance measurements were made with two commercial single-photon detectors. Preliminary measurements were done with a Perkin-Elmer SPCM-AQR14 detector (PDE at $\lambda_2 = 630$ nm: 70%, $D = 200$ counts/s), and we observed a system detection efficiency of 23%, with a total NCR (including detector DCR) of 500 counts/s. For an ultra-low-NCR, we also used a thin-junction Si APD (id Quantique id100: PDE at $\lambda_2 \approx 20\%$, $D = 20$ counts/s). Our measured PDE and NCR are shown in Fig. 5.9, along with a fit to the usual $\sin^2(\cdot)$ relation for the PDE. At $P_p = P_{\max} = 50$ mW, we observed a maximum system detection efficiency of 5.2% and a NCR of 50 counts/s. The main contributions to the low system PDE were the input coupling loss of 1.1 dB ($T = 0.77$), output collection and filtering losses of 1.4 dB ($T = 0.73$), the quoted photon detection efficiency of the APD of 20%, and Fresnel losses of 0.7 dB ($T = 0.86$) due to the uncoated waveguide facet. System improvements, and the use of the MPD (PDM series) Si APD with 40% detection efficiency at 630 nm would result in a system PDE of 27%. The results of this section demonstrate that with judicious choice of pump wavelength λ_p with respect to the input signal λ_1, upconversion detection (and QFC in general) can be done with extremely low added noise, even with no special attempts at output filtering. In the next chapter, we describe a long-wavelength-pumped downconverter for the interface of a solid-state single-photon emitter at 910 nm with the 1.5-μm telecom band.

Chapter 6

Downconversion of single photons from quantum dots

Sources of single photons have numerous applications in quantum optics and quantum information. The best-developed single-photon (SP) sources emit at wavelengths in the visible or near-visible spectral region, while many applications, particularly in quantum communications, would benefit from sources in the 1.3- or 1.55 μm telecommunications bands. In this chapter we review the physics of quantum dots and describe their use as single-photon sources and spin qubits. We then describe an experiment in which single-photons emitted from an InAs quantum dot at $\lambda_2 \approx 910$ nm are downconverted to $\lambda_1 = 1.56$ μm via interaction with a strong pump at $\lambda_p = 2.16$ μm in a PPLN waveguide. For the first time, to our knowledge, we are able to downconvert single photons from a quantum emitter to the 1.5-μm telecommunications band while preserving the single photon character and demonstrating coherent control of the stationary quantum two-level system.

6.1 Quantum dot single-photon sources

The earliest single-photon emitters at optical frequencies were based on heralded single photons: first from atomic cascades [116] and later by SPDC [117]. A true triggered (rather than heralded) SP source would be due to the excitation of a single atom or atom-like system with a single valence electron. The first demonstration of a triggered SP source including a measurement of the photon correlations $G^{(2)}(\tau)$ was in 1999 [118] and was based on the fluorescence of an isolated single molecule at a temperature of 1.8 K.

Quantum dots are islands of narrow-bandgap semiconductor embedded in a larger-bandgap semiconductor matrix, an energy schematic of which is shown in Fig. 6.1. In the InAs/GaAs material system, if a layer of InAs is grown by molecular beam epitaxy (MBE, [119]) on a GaAs substrate, due to the lattice mismatch between InAs and GaAs, after the growth of a conformal wetting layer of approximately 2-nm thickness, the InAs forms islands with diameters between 20 and 40 nm and heights of between 4 and 7 nm, depending on the growth conditions [120]. If the growth flux is low and the growth is stopped soon after the wetting layer forms, the quantum dots (QDs) can be kept to a low area density of less than 1 QD/μm^2; the low QD density allows the possibility of isolating single dots in a confocal microscope setup. An attractive potential results in the confinement of electrons and holes in these quantum dots and results in quantized energy levels (as in the canonical "particle-in-a-box" potential): the bound states of electrons and holes can then be calculated as the eigensolutions to Schrödinger's equation. An attractive feature of InAs/GaAs quantum dots is that there appear to be realistic possibilities for the construction of quantum repeaters based on qubits consisting of either a single electron spin [5] or single hole spin [121] manipulated by ultrafast optical techniques.

The full details of the physics of the level structure of quantum dots and its optical transitions are beyond the scope of this dissertation, but have been studied in detail and can be reviewed in Santori's recent monograph [120]. For our purposes, it will suffice to describe a quantum dot as an idealized quantum two-level system, as shown in Fig. 6.1. The ground state $|0\rangle$ consists of a single electron in the conduction band. There exists an optical transition into the excited state, which consists of an additional exciton (electron–hole pair). For the quantum dot we studied, the energy difference between $|0\rangle$ and $|1\rangle$ was $E_1 - E_0 = \hbar\omega_2 \approx 1.3$ eV, corresponding to a transition wavelength $\lambda_2 \approx 910$ nm.

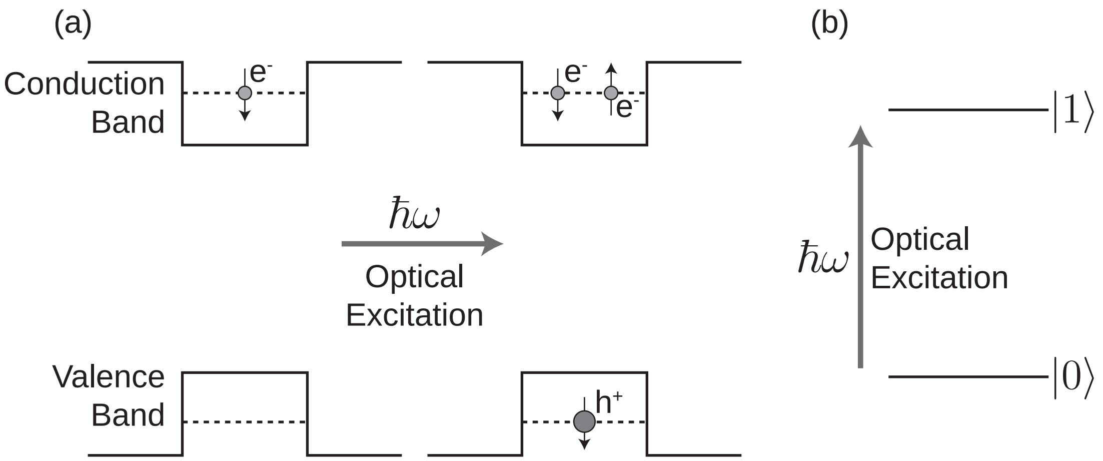

Figure 6.1: (a) Band structure of a quantum dot in its ground and excited states; (b) Two-level picture of same, showing optical transition at $\lambda_2 \approx 910$ nm.

There are several approaches to exciting quantum dots for SP emission. The initial approach taken historically was to use incoherent excitation by a femtosecond Ti:Sapphire laser above the GaAs bandgap at liquid helium temperatures (approximately 780 nm) [122, 123]. This method of excitation has the advantage that carrier generation is very efficient but can tend to result in unwanted excitations of other nearby dots or of higher-energy excited states of the QD. A potentially cleaner approach is to use an excitation pulse on resonance with the desired emission line [124]. To facilitate spatially filtering the quantum dot emission from the strong laser excitation, the excitation pulse was incident from a steep angle. High extinction can also be achieved using crossed polarizers. A third approach has been termed quasi-resonant excitation, in which, as in resonant excitation, one can select one quantum dot out of a sea of dots, but in which the excitation is done via a higher-level excited state (not shown in Fig. 6.1, and not yet well characterized) so that the excitation pulse can be spectrally filtered from the quantum dot emission [125].

For initial characterization of the quantum dot, we used quasi-resonant excitation at 895 nm. To determine whether the emission is from a single emitter or an ensemble, the standard technique is to measure an intensity autocorrelation $g^{(2)}(\tau)$ in a Hanbury Brown–Twiss intensity interferometer [126], shown schematically in Fig. 6.2(a). The

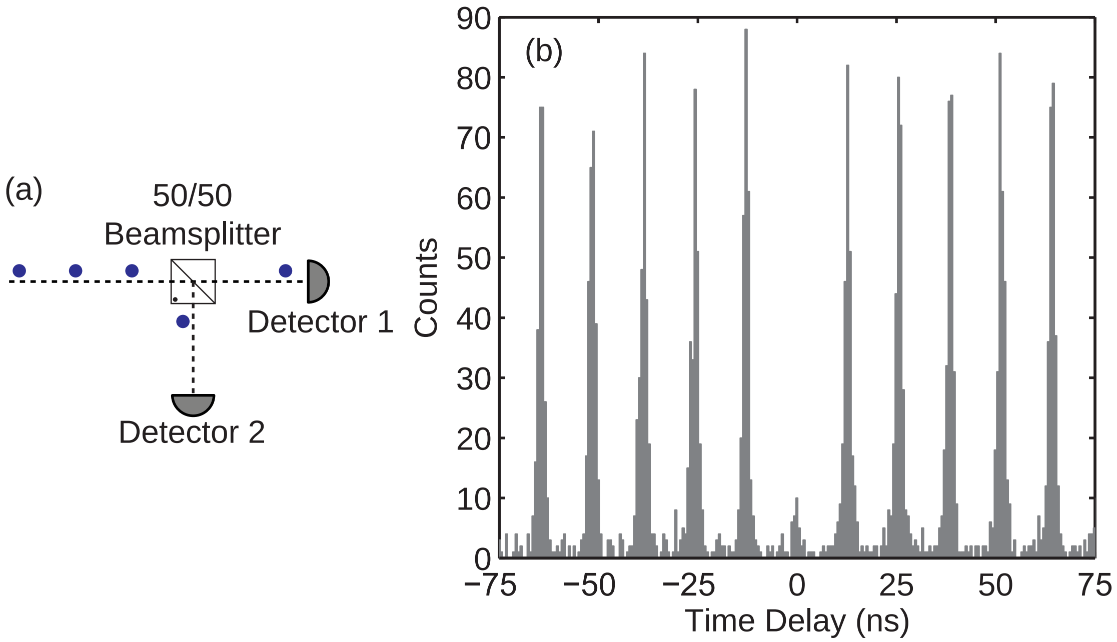

Figure 6.2: (a) Measurement of photon statistics using a beamsplitter and two detectors; (b) intensity autocorrelation $g^{(2)}(\tau)$ of emission from the quantum dot used in the downconversion experiment.

QD is excited with a repetition period of $\tau_R = 13$ ns. If it emits a stream of single photons, one should never observe coincidences between two detectors placed on the output ports of a 50/50 beamsplitter. The measured coincidence data for the quantum dot used in this experiment is shown in Fig. 6.2(b), in which we see a very small peak at $\tau = 0$ when compared with the surrounding "accidental" peaks corresponding to photons emitted from different excitation events. From computing the central peak area and comparing it to the average areas of the accidental peaks, we compute a value $g^{(2)}(0) = 0.13$.

6.2 Classical characterization of the downconversion system

In contrast to the work described in the previous chapter on upconversion, in this experiment we make use of an additional feature of nonlinear optical interactions: they can be used to rapidly gate the detection of a certain event with higher time resolution than would be achievable by direct detection. This concept is effectively the same as that used to measure femtosecond optical phenomena (by optical gating) when detectors with femtosecond response times are not currently technologically feasible [127]. In this system, when the quantum dot is placed in a magnetic field $B = 6$ T, the spin of the electron precesses with a period $T = 30$ ps [5]. If one hopes to temporally resolve events on the time scale of this precession, it is not possible to use conventional single-photon detectors, as these have timing jitters of typically $\Delta t = 50$ ps or more. However, the gating of the single photon emitted by the quantum dot with a short optical pulse can be done with time resolutions of a few picoseconds or better, limited only by group-velocity dispersion effects.

A system-level schematic diagram of the experiment is shown in Fig. 6.3. The quantum dot is excited on resonance either with a 2-ps pulse from the Ti:Sapphire laser shown in the diagram or with a 100-ps pulse from a second Ti:Sapphire laser in which the repetition rate f_R has been locked to the first through active control. The clock signal $f_R = 76$ MHz from the 2-ps mode-locked Ti:Sapphire laser serves as the master clock for the experiment.

To drive the pulsed frequency downconversion process, a short-pulse source at $\lambda_p \approx 2.2$-μm source was needed. We derived this source from the master Ti:Sapphire 2-ps oscillator through the use of a DFG process in a 5-cm-long bulk PPLN (or MgO:PPLN) crystal. Approximately 300 mW of average power at 910 nm was mixed with a C-band signal to generate ps-long pulses at 2.2 μm. In initial experiments, the C-band source consisted of a cw signal from an ECDL which was amplified using an EDFA. At its maximum drive current, the EDFA produced a cw output power of approximately 2 W, and we generated a 2.2-μm signal with a peak power of approximately 16 W. To obtain higher peak power at λ_p, we also utilized a strategy

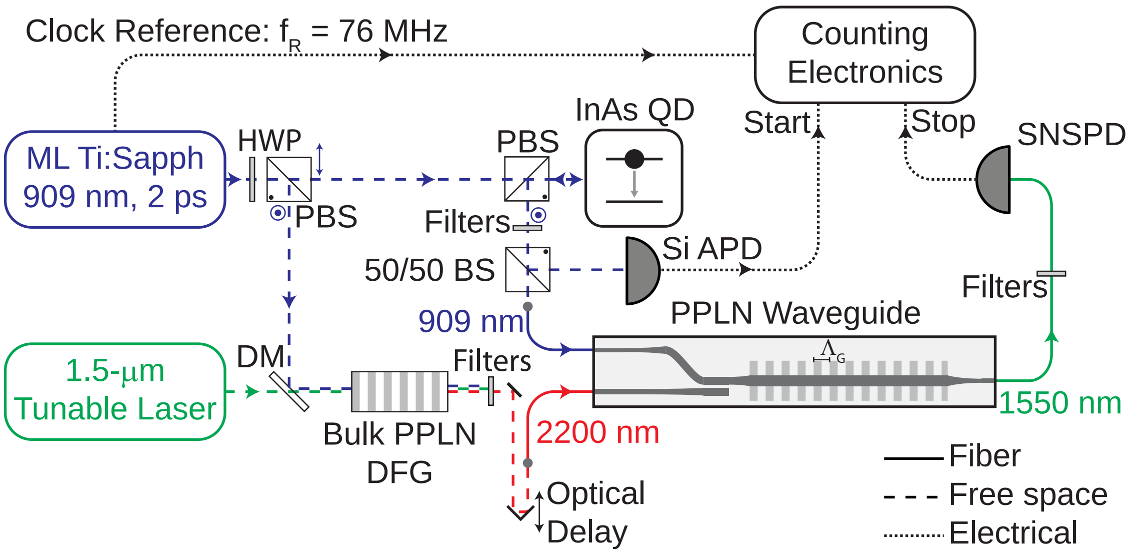
Clock Reference: f_R = 76 MHz
Counting Electronics
ML Ti:Sapph 909 nm, 2 ps
HWP
PBS
PBS
InAs QD
Start
Stop
SNSPD
Filters
50/50 BS
Si APD
Filters
909 nm
PPLN Waveguide
Λ_G
1.5-µm Tunable Laser
DM
Filters
Bulk PPLN DFG
2200 nm
1550 nm
Optical Delay
Fiber
Free space
Electrical

Figure 6.3: Experimental setup for downconversion of single photons from quantum dots. Abbreviations: HWP, half-wave plate; PBS, polarizing beam splitter; SNSPD, superconducting nanowire single-photon detector.

where the EDFA seed signal was pulsed at f_R with a short optical pulse width. This modulation was achieved by using the Ti:Sapphire electrical clock signal to synchronize a pulse-pattern generator (PPG). The 10-GHz PPG produced 300-ps electrical pulses which were used to drive an electro-optic intensity modulator. The modulated optical signal was then first amplified in a low-power EDFA (preamplifier) designed with a low input saturation power of -23 dBm. The output of the preamplifier had an average power of approximately 10 mW and was used to seed the the same power amplifier as had been used with cw C-band light. The pulsed seed enabled substantially higher peak powers in the C-band, and therefore produced much higher peak powers at 2.2 μm, as also shown in Fig. 6.4.

The crystals used in the bulk DFG source had a length of $L = 5$ cm. This length is substantially longer than the group-velocity walkoff length between the input signals $L_{\text{GVM}} = \tau_0/\delta\nu_{12} = 1.07$ cm, where $\tau_0 = 2$ ps is the Ti:Sapphire pulsewidth and $\delta\nu_{ij} = u_i^{-1} - u_2^{-j}$, where u_i is the group velocity at λ_i with $i \in \{p, 1, 2\}$. As such, the pulsewidth of the generated pulse at 2.2 μm is determined by the group velocity

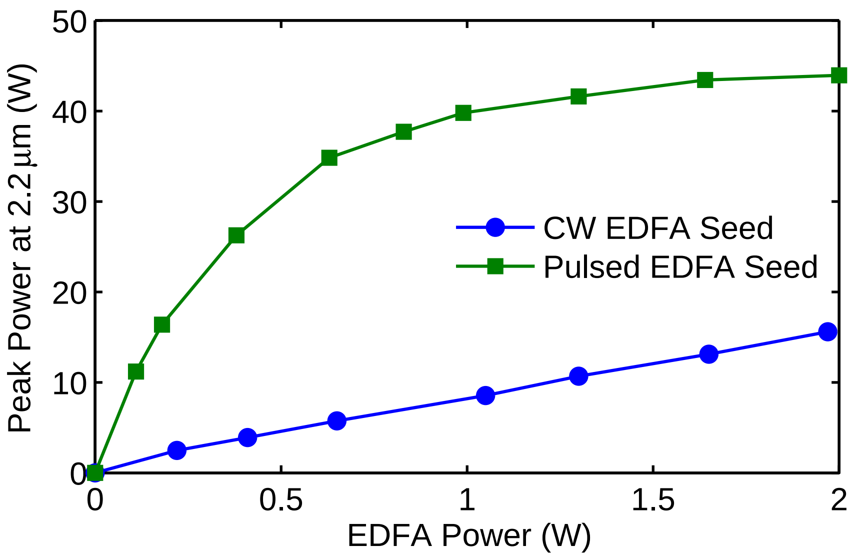

Figure 6.4: Bulk DFG results for generation of pump radiation at $\lambda_p \approx 2.2$ μm. For the "Pulsed EDFA Seed" case, the radiation from the ECDL was modulated with a pulse width of 300 ps to increase the peak power extracted from the EDFA.

walkoff, and has been numerically simulated to be 8.6 ps full-width at $1/e^2$-intensity maximum using a split-step Fourier simulation technique [128]. The fact that the time resolution of the experiment can be determined by the pulsewidth of the 2.2-μm gating pulse provides a convenient control variable. We have procured MgO:PPLN crystals with QPM gratings of three different lengths (1 cm, 3 cm, and 5 cm) positioned adjacently on the same 5-cm substrates to allow control over the time resolution.

Again referencing Fig. 6.3, the generated 2.2-μm short pulses are sent through a variable optical delay line and then coupled into optical fiber. In the quantum dot path, the single-photon emission is collected with a polarization perpendicular to the input excitation to enable polarization filtering of the strong resonant excitation. After spectral filtering using a set of diffraction gratings and filters, the single-photon emission at $\lambda_2 \approx 910$ nm is fiber coupled using HI-780 fiber, with approximately 60% coupling efficiency.

Owing to the complexity of combining two very dissimilar wavelengths in the fundamental spatial mode of a single waveguide, the waveguide design used in this experiment incorporated a directional coupler. Light from the quantum dot at λ_2 and from the pulsed source at $\lambda_p = 2.2$ μm enter the device from separate fibers into two separate waveguides. The two fibers are terminated in a silicon V-groove array and are pigtailed to the chip input. The QD light at λ_2 goes through an adiabatic taper and an S-bend to bring it into proximity with the waveguide carrying the pump light at λ_p where they enter the two input ports of a directional coupler. The directional coupler was designed such that the pump light was coupled over to the adjacent waveguide while the coupling for the quantum dot light was low (parameters: waveguide channel width: 5.4 μm, waveguide center-to-center spacing: 10 μm, directional coupler length: 0.95 mm). The combined pump and signal light then entered the QPM mixing region, which was poled with $\Lambda_G = 21.9$ μm and had length $L_Q = 4$ cm. At the output of the mixing region, the converted light at $\lambda_1 = 1550$ nm was sent through another adiabatic taper and mode filter and coupled into an optical fiber (SMF-28) pigtailed to the exit facet of the waveguide. Input coupling and propagation losses at 910 nm were observed to be 1.5 dB, and the output coupling loss at 1550 nm was also 1.5 dB. The observed coupling loss and waveguide propagation loss at 2.2 μm was approximately 7 dB. There is an OH^- absorption feature due to a vibration-libration resonance at a wavelength of 2250 nm [129]. The intentional proton doping to create the waveguide enhances this absorption. It is suspected that the short-wavelength tail of this absorption feature is responsible for the relatively high losses observed when compared with the NIR quantum dot emission which is very far detuned from the absorption resonance.

We characterized temporal resolution of the conversion by performing a DFG cross-correlation in the PPLN waveguide. Classical pulses from the 2-ps Ti:Sapphire laser with peak powers of a few mW were sent into the waveguide along with the 2.2-μm pump pulses and we measured the generated DFG signal at 1550 nm as a function of the 2.2-μm pulse delay. Our results are shown in Fig. 6.5, along with a simulation based on a split-step Fourier method. From this data, we observe that for 2-ps Ti:Sapphire pump pulses, the approximate conversion time window is 6–10 ps.

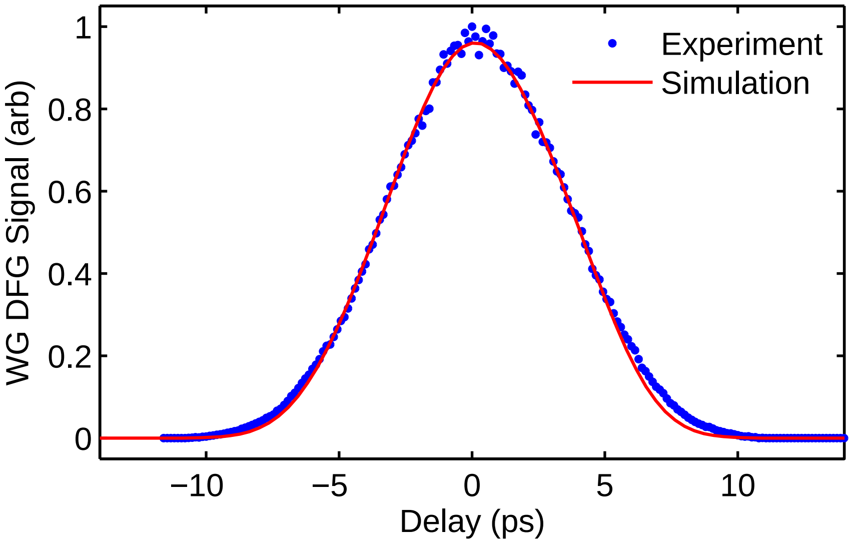

Figure 6.5: Measured DFG radiation at $\lambda_1 = 1550$ nm as a function of delay time between 2.2-μm pump pulse and 910-nm probe pulse (dots) and split-step Fourier simulation (solid).

6.3 Single-photon experiments

Following classical-signal-level characterization of the conversion processes, we attempted single-photon downconversion experiments. Again referring to Fig. 6.3, we utilized a superconducting nanowire single-photon detector (SNSPD) to detect the down-converted single photons. The detector was packaged with a SMF-28 fiber optic input and was housed in a ^{3}He cryostat. The detector was operated at a temperature of approximately 2 K with a voltage bias of 3.3 V [130]. The SNSPD had a detection efficiency of approximately 14% and a dark-count rate of approximately 40 counts/s.

We briefly comment on the filtering techniques used after the waveguide to separate the outgoing downconverted signal from other unwanted spectral components of radiation. One difficulty of using SNSPDs is that they are sensitive to effectively all wavelengths of light shorter than the mid-infrared. There are multiple intrinsic and technical noise sources that must be filtered. At the output of the waveguide, we used a fiber-optic circulator and a fiber Bragg grating (FBG) with a reflection bandwidth of approximately 2 nm to attempt to eliminate all but the converted quantum-dot single photons. The loss of this setup was approximately 1.5 dB (dominated by the circulator) and the extinction ratio was approximately 60 dB, limited by the directivity of the circulator. Some amount of both pump light at $\lambda_p = 2.2\ \mu\text{m}$ along with its second harmonic at 1100 nm were therefore present at the output port of the circulator. To filter this radiation further, we employed two strategies: tight-radius bending of the optical fiber to remove the long-wavelength pump via radiation losses and a 1350-nm long-pass filter on a Si substrate inserted into a fiber U-bench to remove both the parasitic second harmonic light and any unconverted 910 light from the quantum dot setup. The loss of the U-bench and long-pass filter was approximately 1.5 dB. We observed a saturation of the conversion efficiency at a 2.2-μm peak pump power of approximately 3 W in the input fiber. With these filtering mechanisms in place, at this power level we observed noise count rates due to spontaneous scattering or other leakage processes below 1 count/s. We note that if the narrowband FBG filter was removed, a significant noise count rate (in the range of approximately 100 counts/s) was observed, which we suspect are due to broadband spontaneous anti-Stokes Raman scattering.

Throughout this experiment, we perform measurements using the time-correlated single-photon counting technique (TCSPC). In TCSPC, the arrival time of the electrical pulse from a single-photon detector is compared to a regular trigger signal, in our case, from the clock output of the Ti:Sapphire master oscillator. Over many events, a histogram of arrival times is formed, resulting in a time-ensemble measurement of a temporal waveform containing less than one photon per clock cycle on average.

We estimate the incident photon rate entering the PPLN waveguide from the quantum dot at a level of approximately 6×10^4 photons/s. Using a TCSPC measurement, we characterized the spontaneous emission decay time of the quantum dot emission and found it to be well-described by a single exponential with an approximately 600 ps time constant. We then turned on the conversion pulse, which sampled an approximately 10-ps time window of the quantum dot emission. Experimental results of the pulsed conversion of the quantum dot signal as a function of the time delay between the quantum dot excitation pulse and the conversion pump pulse are shown in Fig. 6.6. At early times, we observe a relatively rapid rise in the converted

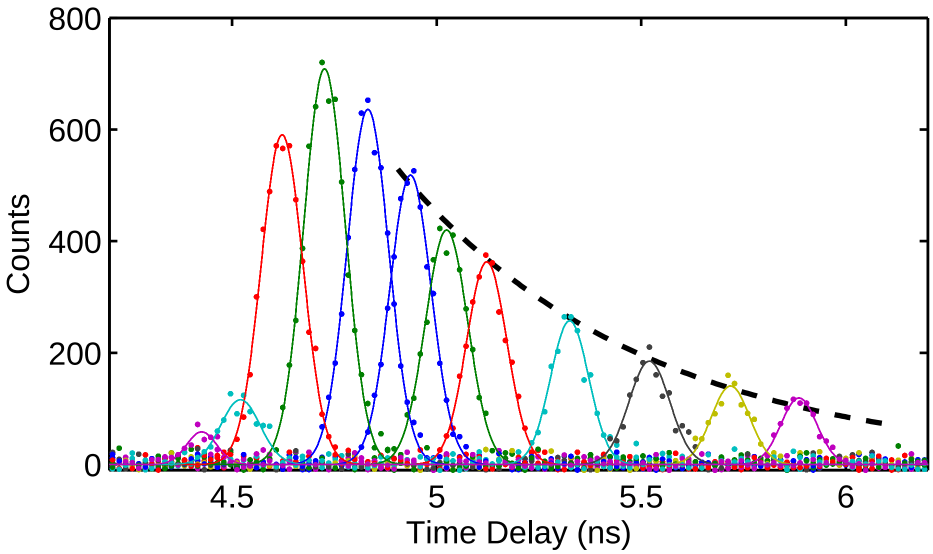

Figure 6.6: Measured net photon counts at 1550 nm as the radiation from the quantum dot is downconverted and the delay between the quantum dot excitation and the conversion pump pulse is varied. The temporally uncorrelated dark counts of the SNSPD have been subtracted.

counts as the quantum dot is excited by a 100-ps-long excitation pulse. At later times, we see that the converted light exhibits a tail of emission, corresponding to the 600-ps spontaneous emission lifetime of the quantum dot. The dark-count level of the SNSPD (counts which are uncorrelated in time) in Fig. 6.6 has been subtracted, and the measurement at each time delay was integrated for five minutes. The solid curves represent Gaussian fits to the data at each time delay, and all have temporal widths in the range of 100 ps, the SNSPD timing jitter. The dashed solid curve is an exponential fit to the peaks of the count distributions for each time delay, and has a time constant of 600 ps. The signal count rate at the emission peak (at a delay of 4.7 ps), integrated over the Gaussian instrument response of the SNSPD, is approximately 20 counts/s. This count rate is consistent with the measured rate of single photons into the HI-780 input fiber of approximately 6×10^4 photons/s, a temporal overlap factor of approximately 1.7%, and the loss sources already delineated.

The measurement described above of tracing out the temporal shape of the emitted waveform from the sample, while exhibiting the exponential spontaneous emission tail,

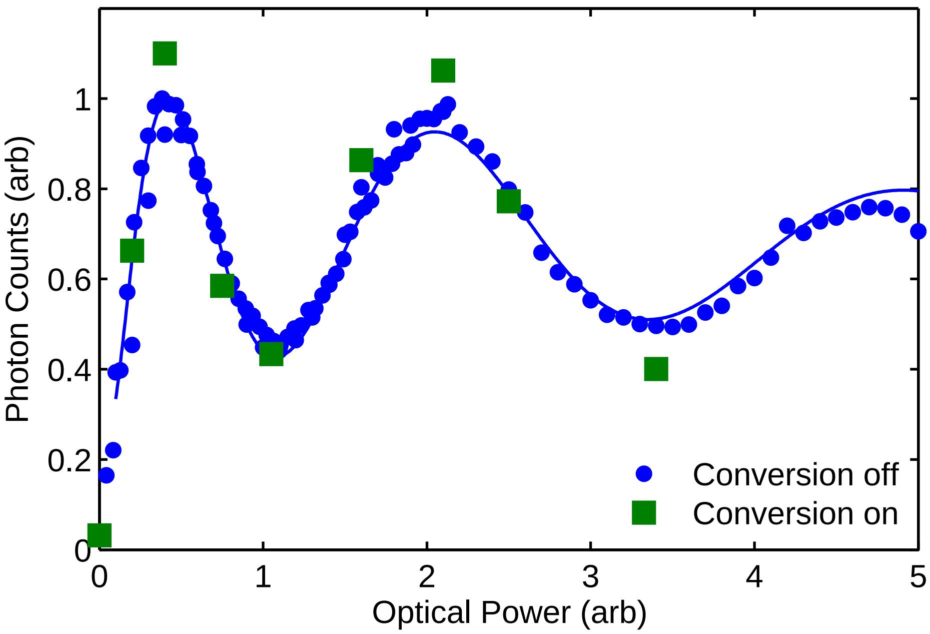

Figure 6.7: Measured photon counts at 910 nm (blue dots) or downconverted to 1550 nm (green squares) as a function of excitation power, showing Rabi oscillations.

does not demonstrate the coherent manipulation of a quantum two level system. To demonstrate this, we did a Rabi oscillation experiment, whereby the photon count rate was measured as a function of the power of the optical excitation. If (referring to Fig. 6.1) the quantum dot starts in state $|0\rangle$, then as the excitation field $\tilde{E}(t) = E_A(t)e^{i\omega_2 t}$ (where we have defined $E_A(t)$ as the slowly-varying field envelope) is varied the state is rotated to a superposition state:

$$|\psi\rangle = \cos\left(\frac{\theta}{2}\right)|0\rangle + \sin\left(\frac{\theta}{2}\right)|1\rangle \tag{6.1}$$

where the rotation angle

$$\theta = \kappa \int_{-\infty}^{t} E_A(t')\, \mathrm{d}t' \tag{6.2}$$

where the coupling constant $\kappa = 2\mu/\hbar$, where μ is the dipole moment of the system [131]. From Eq. (6.2), we note that the rotation angle is expected to be proportional to $\sqrt{P}$. If, at the end of the coherent manipulation via the resonant pulse $\tilde{E}(t)$, the system is in state $|\psi\rangle$ given by Eq. (6.1), we will measure the projection $|\langle\psi|1\rangle|^2 = \sin^2(\theta/2)$ because after the pulse is turned off the upper state will spontaneously decay via the emission of a single photon, which can then be measured.

Our experimental results are shown in Fig. 6.7. The blue dots are the recorded photon counts of 910-nm photons emitted from the quantum dot without downconversion. As we can see, they rise from a low value when the excitation power is very low and undergo a series of oscillations as the state has been coherently manipulated through rotations of $m\pi$, where the maxima correspond to m odd and the minima correspond to m even. The solid blue curve in Fig. 6.7 is a fit to an empirical relation of the form:

$$C(P) = C_0 + aP^b + Ae^{-P/\alpha}\sin^2\left(\frac{\pi}{2}\sqrt{\frac{P}{P_0}}\right) \tag{6.3}$$

where we have included a DC offset due to dark or leakage counts, a background level rising as a power law, and an exponentially damped oscillatory term. We then turned on the conversion pump at a fixed time delay and measured the converted counts as a function of the quantum dot excitation power. The results, scaled to the same vertical scale, as the non-converted quantum dot light, are shown as green squares. We see the same oscillations in the count rate as the excitation power is varied, confirming that the downconverter is preserving quantum properties of the source.

An important aspect to prove that the quantum frequency downconverter maintains the quantum state of the light emitted from the quantum dot is the investigation of photon statistics. This experimental task proved to be challenging as the low count rates (dominated by the low temporal overlap of the conversion pulse with the quantum dot spontaneous emission waveform) necessitated very long integrations of several hours. Again referring to the experimental setup in Fig. 6.3, we now seek to measure correlations in detected events between the Si APD which is sampling the emitted quantum dot before the waveguide and the converted photons at 1550 nm measured following downconversion.

We used the temporal resolution of the detection setup to eliminate the calculation of coincidence counts from the Si APD and the SNSPD at times that do not correspond to the proper phase of the clock cycle for when the converted photons appear.

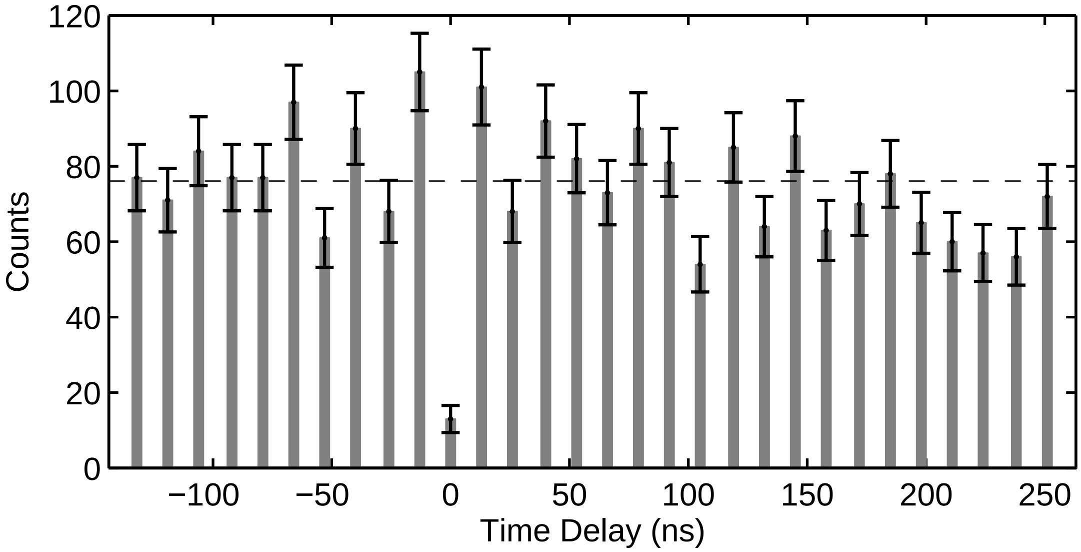

Figure 6.8: Measured coincidence counts as a function of time delay between downconverted photons counted on the SNSPD and non-converted photons measured before the waveguide on a Si APD. We observe an antibunching dip corresponding to a value $g^{(2)}(0) = 0.17$, showing preservation of the single-photon character of the quantum dot emission after downconversion.

Our coincidence data is shown in Fig. 6.8. At zero time delay, we observe a dip in the coincidences corresponding to antibunched statistics. Computing the area of the dip and comparing with the surrounding accidental peaks gives a value $g^{(2)}(0) = 0.17$, which is only slightly higher than the value observed with quasi-resonant excitation and no downconversion: 0.13. We should note that neither here nor in the non-converted $g^{(2)}(\tau)$ measurement shown in Fig. 6.2(b) has any background subtraction been done. Any detector dark counts appearing inside the time window of the SNSPD in which coincidences may be registered will add to the noise. If these dark counts were subtracted we believe that the measured $g^{(2)}(\tau)$ would probably be somewhat improved when compared with the nonconverted data of Fig. 6.2. This improvement would be due to the fact that the conversion process effectively provides filtering in both frequency (due to the limited acceptance bandwidth of the downconverter of approximately 0.2 nm) and the strong temporal filtering due to the pulsed conversion process, where no temporal filtering was done in the experiment without conversion.

6.4 Summary

To summarize the work described in this chapter, we have developed a waveguide mixer and short-pulsed 2.2-μm pump source for efficient, temporally resolved downconversion of single photons from InAs/GaAs quantum dots into the telecommunications band. We have confirmed the quantum nature of the emitter through a Rabi oscillation experiment, whereby the oscillatory behavior observed in the count rate as a function of excitation power was also observed upon downconversion of the photons. We have also confirmed the single-photon character of the emission by measuring antibunching of the counts in a cross-correlation experiment. The use of a very long-wavelength pump source enabled low-noise frequency conversion: our measured noise count rates (counts due to the presence of the 2.2-μm pump) were estimated to be approximately 1 count per second.

To the best of our knowledge, this experiment represents the first demonstration of the downconversion of a stationary quantum emitter to the 1.5 μm telecommunications band. There have been two recent demonstrations of downconversion to the 1.3-μm telecom band. The first experiment was a component of a quantum memory based on trapped ^{87}Rb atoms where the downconversion was achieved via four-wave mixing in cold Rb vapor [132]. The second experiment was a recent demonstration of the downconversion of quantum dot single photons at $\lambda_2 = 710$ nm to $\lambda_1 = 1310$ nm using a strong pump at 1550 nm [133]. However, the quantum dots used in this experiment were based on InP/GaInP and there have been no demonstrations of spin control in this system, but these quantum dots are suitable for electrically triggered single-photon generation [134]. There has also been recent work on a 1.5-μm telecom-band single-photon stource based on InAs/InP quantum dots [135], but there have been no attempts at spin control of quantum dots with C-band transitions.

For the experiments described in this chapter, the use of a pulsed pump for the downconversion process was not necessary or even perhaps advisable if demonstration of low-noise downconversion was the only goal. The ultimate goal of this experiment, however, was the demonstration of entanglement between the quantum dot electron spin and the polarization of the emitted photon. For a quantum dot in a magnetic field, the Zeeman effect lifts the energy degeneracy of the two spin states of the electron, which we denote as $|\uparrow\rangle$ and $|\downarrow\rangle$, where the energy difference corresponds to a frequency $\delta_e = (E_\uparrow - E_\downarrow)/\hbar \approx 2\pi \times 30$ GHz. Therefore, the entangled state can be written

$$|\Psi\rangle = \frac{1}{\sqrt{2}}\left(|\uparrow\rangle \otimes |iH;\omega_2 + \delta_e\rangle + |\downarrow\rangle \otimes |V;\omega_2\rangle\right) \tag{6.4}$$

From Eq. (6.4), we see that there is entanglement not only between the photon polarization and the spin state, but also the photon frequency and spin state. Therefore, the photon frequency provides "which-path" information about the state of the spin, and therefore, would destroy the entanglement unless the frequency information can be erased. In a pioneering spin-photon entanglement experiment, it was realized that a time-resolved detection (with time resolution $\Delta t \ll 1/\delta_e$ provides such a a quantum eraser [4]. This erasure was possible in the experiment of Togan and coworkers because in the NV-center system the energy splitting (in that system, provided by strain rather than Zeeman splitting) was very low (approximately 300 MHz) which meant that standard single-photon detectors provided sufficient time resolution to achieve the quantum erasure effect. In our experiment, however, where $\delta_e \approx 2\pi \times 30$ GHz, a time resolution of approximately 30 ps is needed, which is lower than is available with commercial single-photon detectors. Hence, we employ the pulsed frequency conversion technique.

We have recently verified the entanglement between the quantum dot spin state and the downconverted telecom-band photon [136]. Combining spin-photon entanglement with a two-photon interference experiment should enable entanglement generation between remote quantum dot spins. The fact that the spin–spin entanglement will be mediated by telecom band single photons could potentially enable entangled states of stationary qubits at distances of tens of km, compared to the relatively modest distances of approximately 1 m thus far achieved in the entanglement between two trapped ions [137].

Chapter 7

Advanced quantum frequency conversion devices

In this chapter, we move past devices for one-step frequency up- and downconversion and address some novel device designs that can bring additional functionality to single-photon frequency conversion systems. Broadly speaking, we can use similar device engineering techniques as are found in classical optical signal processing systems [9] and refocus them for the quantum realm. The primary applications we address are to enable low-noise frequency conversion between widely disparate frequencies, and to enable detection and processing of high-data-rate modulated signals.

7.1 Cascaded quantum frequency conversion and applications

In this section, we will describe aspects of the theory and design constraints of incorporating two QPM gratings within a single waveguide for cascaded conversion. With such a device we achieved quasi-phasematching of two SFG processes, enabling 87% conversion efficiency of a signal from 1550 nm to 570 nm [65]. Sec. 7.1.2 describes an application for a high-speed SPD with a total system timing jitter of 66.9 ps. Sec. 7.1.3 presents potential applications for downconversion of single-photon sources

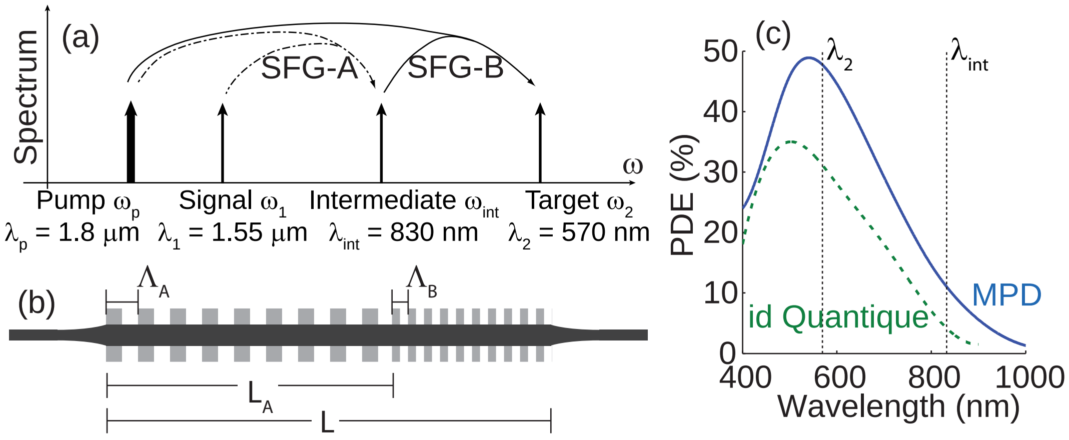
(a)
Spectrum
SFG-A
SFG-B
ω
Pump ω_p
λ_p = 1.8 μm
Signal ω_1
λ_1 = 1.55 μm
Intermediate ω_{int}
λ_{int} = 830 nm
Target ω_2
λ_2 = 570 nm
(b)
Λ_A
Λ_B
L_A
L
(c)
λ_2
λ_{int}
PDE (%)
50
40
30
20
10
0
400
600
800
1000
Wavelength (nm)
MPD
id Quantique

Figure 7.1: Schematics of (a) frequencies involved with and (b) PPLN waveguide design for two-stage upconversion for low-timing-jitter single-photon detection; (c) PDE of commercial low-jitter Si SPDs versus wavelength, manufactured by MPD and id Quantique.

in the visible spectral range to the 1.55 μm telecom band [48].

7.1.1 Cascaded conversion theory and device design

First, we briefly develop the theory of a cascaded frequency conversion device. We consider here the case of cascaded SFG, which has been demonstrated and will be described in the next section. We consider a device for the upconversion of a signal at ω_1 to ω_2 via a two-stage upconversion process using a single optical pump at ω_p, a schematic of which is shown in Fig. 7.1(a). However, the description is generic and could equally well be applied to cascaded DFG, an application of which will be described in Sec. 7.1.3. Here, the input signal at ω_1 is first summed with a long-wavelength pump at ω_p to produce radiation at $\omega_{\text{int}} = \omega_1 + \omega_p$ in a process we term SFG-A. A second SFG process (SFG-B, here, within the same PPLN waveguide) is then used to sum the light at ω_{int} with the same pump to produce the target radiation at $\omega_2 = \omega_{\text{int}} + \omega_p = \omega_1 + 2\omega_p$.

We consider a QPM grating with Fourier components at $K_A = \Delta k_A = k_{\text{int}} - k_1 - k_p$ and $K_B = \Delta k_B = k_2 - k_{\text{int}} - k_p$. The amplitudes of each frequency component, which we refer to as $g_A(z)$ and $g_B(z)$, may vary along the propagation distance z

of the device. Ideally, they obey the constraint $|g_A(z)|^2 + |g_B(z)|^2 = 1$, which is a manifestation of Parseval's identity for the Fourier transform of a nonlinear coefficient $d(z)$ whose magnitude (but not necessarily whose phase) is independent of z. A two-component QPM grating could be fabricated using, e.g., a phase-modulated structure[1] [138] or an optical superlattice approach [139].

The coupled amplitude equations for normalized field envelopes in a two-stage frequency conversion process, in the limit of an undepleted pump and negligible propagation loss, are given by

$$\frac{\mathrm{d}a_2}{\mathrm{d}z} = -i\gamma_B g_B(z) a_{\text{int}} e^{i\Delta k_B z}, \tag{7.1a}$$
$$\frac{\mathrm{d}a_{\text{int}}}{\mathrm{d}z} = -i\gamma_B g_B(z) a_2 e^{-i\Delta k_B z} - i\gamma_A g_A(z) a_1 e^{i\Delta k_A z}, \tag{7.1b}$$
$$\frac{\mathrm{d}a_1}{\mathrm{d}z} = -i\gamma_A g_A(z) a_{\text{int}} e^{-i\Delta k_A z}, \tag{7.1c}$$

where $\gamma_j = \sqrt{\eta_{\text{nor},j} P_p}$, where $\eta_{\text{nor},j}$ is the normalized conversion efficiency of process $j \in \{\text{A, B}\}$, and $[|a_k(z)|^2]$ = photons/second [67]. Analytical solutions of Eqs. (7.1) are possible for either an abrupt transition where $g_A(z) = 1$ for $0 < z < L_A$ or where the Fourier amplitudes are constant with z: $g_A(z) = g_0$ and $g_B(z) = (1 - g_0^2)^{1/2}$. We focus here on the case of sequential gratings, the simplest structure to design and fabricate. Assuming incident radiation only at ω_1, and perfect QPM for both SFG processes, the conversion efficiency η_2 (η_{int}) to frequency ω_2 (ω_{int}) are given as

$$\eta_2 = \frac{N_2(L)}{N_1(0)} = \sin^2[\gamma_A L_A] \sin^2[\gamma_B (L - L_A)] \tag{7.2a}$$
$$\eta_{\text{int}} = \frac{N_{\text{int}}(L)}{N_1(0)} = \sin^2[\gamma_A L_A] \cos^2[\gamma_B (L - L_A)], \tag{7.2b}$$

from which we see that complete conversion from ω_1 to ω_2 is possible only when $\gamma_A L_A = \gamma_B (L - L_A) = \pi/2$. This constraint sets the optimal grating transition location $L_A/L = \gamma_B/(\gamma_A + \gamma_B)$.

Although the fabricated devices described in the following section have used the

---

[1] A detailed discussion of phase-modulated QPM design is given in Sec. 7.2.

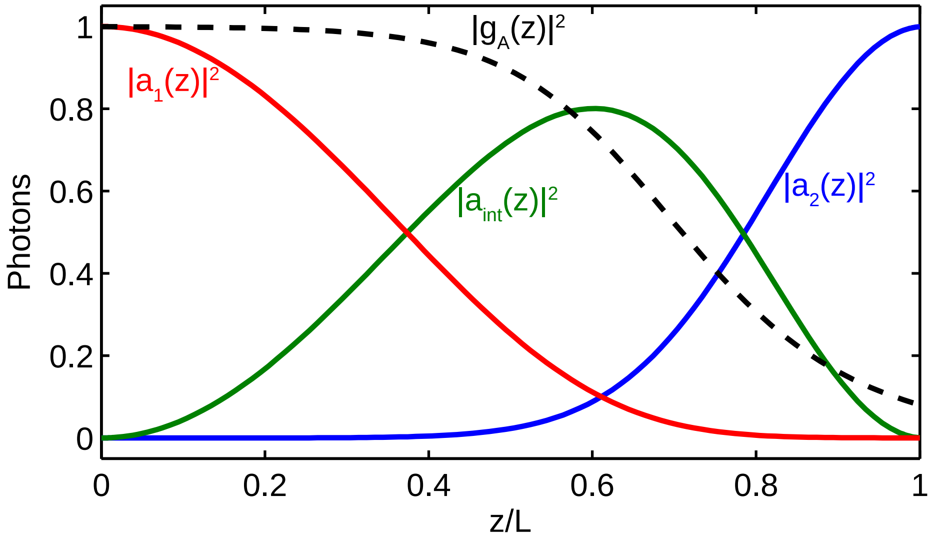

Figure 7.2: Photon-flux evolution in a two-component grating optimized for efficient cascaded upconversion.

sequential grating approach solved in Eqs. (7.2), it is interesting to consider more sophisticated QPM designs in which $g_A(z)$ and $g_B(z)$ are spatially varying. A useful model function that can be used to smoothly interpolate between the sequential- and simultaneous-grating approaches is given as:

$$g_A(z) = 2^{-\alpha}\left[1 - \tanh\left(\frac{z - L_A}{W}\right)\right]^{\alpha}. \tag{7.3}$$

With the parameters $\alpha = 0.33$ and $W = 0.183L$, we find that complete conversion is achieved at a pump power 22.1% lower than for sequential gratings and 28.9% lower than for simultaneous gratings. The photon flux evolution and grating weight $|g_A(z)|^2$ for an optimized grating is shown in Fig. 7.2. In future work we may pursue a more sophisticated grating design, as any reduction of $P_{\max}$ also yields a reduction in noise. We have not proven that Eq. (7.3) produces a global minimum $P_{\max}$, so further reductions in $P_{\max}$ may be possible.

7.1.2 Cascaded upconversion for high-speed single-photon detection

The SPD figure-of-merit $H = \eta_\nu/(D\,\Delta t)$ for the upconversion detector described in Chapter 5 was limited by the large value of $\Delta t \approx 400$ ps of the thick-junction APD used in the experiment. A thick-junction APD was used because the thin-junction devices are optimized for blueshifted wavelengths, as shown in Fig. 7.1(c). To upconvert a signal to a near-peak wavelength (close to 600 nm) in a single step would result in the use of a short-wavelength pump, which results in high noise: Thew *et al.* observed a noise count rate of 3×10^5 counts/s in an early experiment pumped at 980 nm [33]. To bypass this problem we use the cascaded frequency conversion approach. A long wavelength pump at ω_p is summed with the input signal at ω_1 to produce radiation at $\omega_{\text{int}} = \omega_1 + \omega_p$. A second SFG process (SFG-B) is used to sum the light at ω_{int} with the same pump to produce the target radiation at $\omega_2 = \omega_{\text{int}} + \omega_p = \omega_1 + 2\omega_p$. For an input signal at $\lambda_1 = 1.55$ μm and $\lambda_p = 1.8$ μm, $\lambda_{\text{int}} \approx 830$ nm and $\lambda_2 \approx 570$ nm. This two-step process produces target radiation near the peak PDE for low-jitter APDs.

We fabricated a two-step upconverter based on the sequential QPM grating approach described above. The waveguide had total length $L = 5.2$ cm, and incorporated mode filters and adiabatic tapers to spatially mode-match the input of the waveguide to SMF-28 optical fiber. The waveguide was fiber-pigtailed with coupling loss of 0.5 dB, and had propagation loss of 0.12 dB cm^{-1}. The schematic of our experiment is shown in Fig. 7.3. Pump light at 1801 nm from a monolithic PPLN optical parametric oscillator [97], amplified with a Tm-doped fiber amplifier, was combined with a 1.55-μm signal using a fiber-optic WDM. The waveguide had QPM periods $\Lambda_A = 18.55$ μm and $\Lambda_B = 8.25$ μm, with $L_A/L = 0.64$. For initial characterization of the devices, the signal source was a cw tunable external-cavity diode laser.

We first characterized the conversion efficiency of the device versus signal wavelength and temperature. In order to achieve efficient conversion, both SFG-A and SFG-B must be tuned near their QPM peaks. This tuning was done by noticing that SFG-A and SFG-B temperature-tune at slightly different rates. Fig 7.4(a) shows the

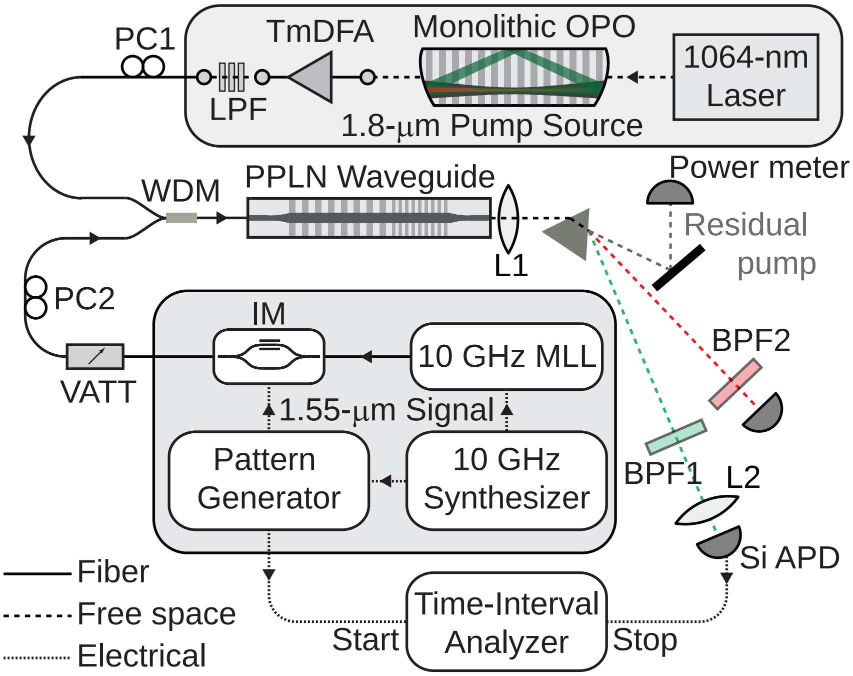
PC1
TmDFA
Monolithic OPO
1064-nm Laser
LPF
1.8-µm Pump Source
WDM
PPLN Waveguide
Power meter
Residual pump
L1
PC2
IM
10 GHz MLL
VATT
1.55-µm Signal
BPF2
Pattern Generator
10 GHz Synthesizer
BPF1
L2
Si APD
Fiber
Free space
Electrical
Time-Interval Analyzer
Start
Stop

Figure 7.3: Experimental setup for cascaded upconversion of single photons. Abbreviations: PC, polarization controller; LPF, long-pass filter; VATT, variable optical attenuator; MLL, mode-locked laser; BPF, band-pass filter.

experimental results: for a pump wavelength $\lambda_p = 1801.3$ nm, quasi-phasematching for both SFG processes was observed for $\lambda_1 = 1548.2$ nm and $T = 76°$ C.

We next measured the conversion efficiency of a weak classical input signal at ω_1. When SFG-A and SFG-B are both tuned to their QPM peaks, the conversion efficiencies η_2 and η_{int} are plotted in Fig. 7.5, along with a fit to Eq. (7.2). Experimental values of the conversion efficiency are defined with respect to the signal power at the input of the waveguide. The efficiency for the cascaded process is limited by the observed propagation loss and by a slightly non-optimal value of L_A for the device.

We demonstrated an application of this device for high clock-rate single-photon detection of a pulsed light source. A pulsed 1550-nm signal was generated using a 10-GHz actively mode-locked laser with pulse length of 10 ps, and using an electro-optic intensity modulator to downsample the pulse train to 1 GHz. This signal

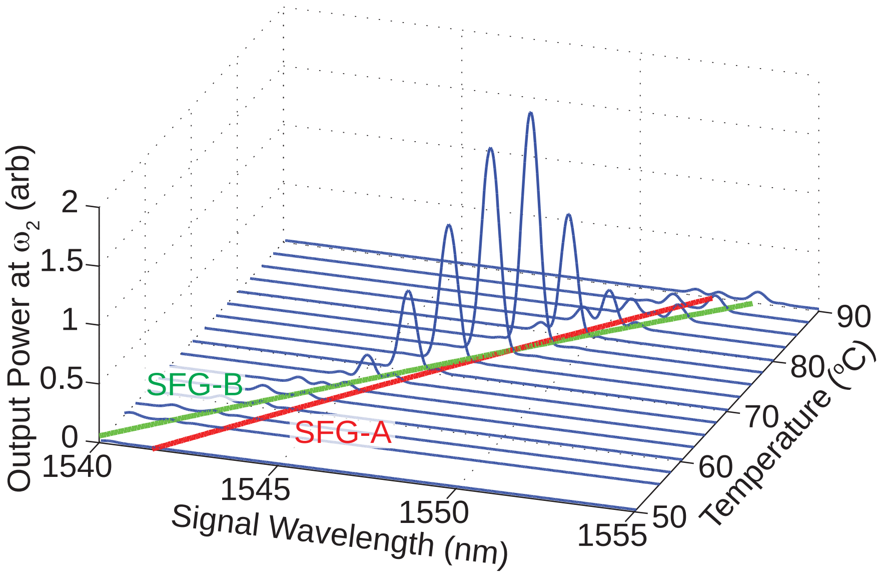

Figure 7.4: Measured cascaded SFG at $\lambda_2 = 570$ nm as a function of signal wavelength λ_1 and device temperature T, showing dual QPM at $\lambda_1 = 1548.2$ nm and $T = 76°$ C. Green and red curves are the individual QPM trajectories for SFG-A and SFG-B respectively; the efficiency of the two-step process is maximized where these curves intersect.

was attenuated to a level of 0.01 photons per pulse and upconverted using the two-step upconversion waveguide described above. The output signal at ω_2 was detected using a Si APD (id Quantique id100). Measurements were performed with $P_p =$ 100 mW, corresponding to a background dark-count rate of approximately 850 counts s^{-1} which was attributed to two-step upconversion of noise photons generated by anti-Stokes spontaneous Raman scattering of the 1.8-μm pump [67]. Time-correlated single-photon counting measurements were carried out using a time-interval analyzer (TIA) started by the clock output of the pattern generator and stopped by the APD output electrical pulses. Our results are plotted in Fig. 7.6: we observe a FWHM timing jitter of 66.9 ps, which is close to the 50-ps specification provided by the manufacturer. Additional sources of timing uncertainty are due to jitter within the TIA of approximately 25 ps, and noise in the triggering electronics. We do not suspect the introduction of additional timing jitter by the upconversion process.

To conclude this section, we have demonstrated 87% conversion efficiency of a

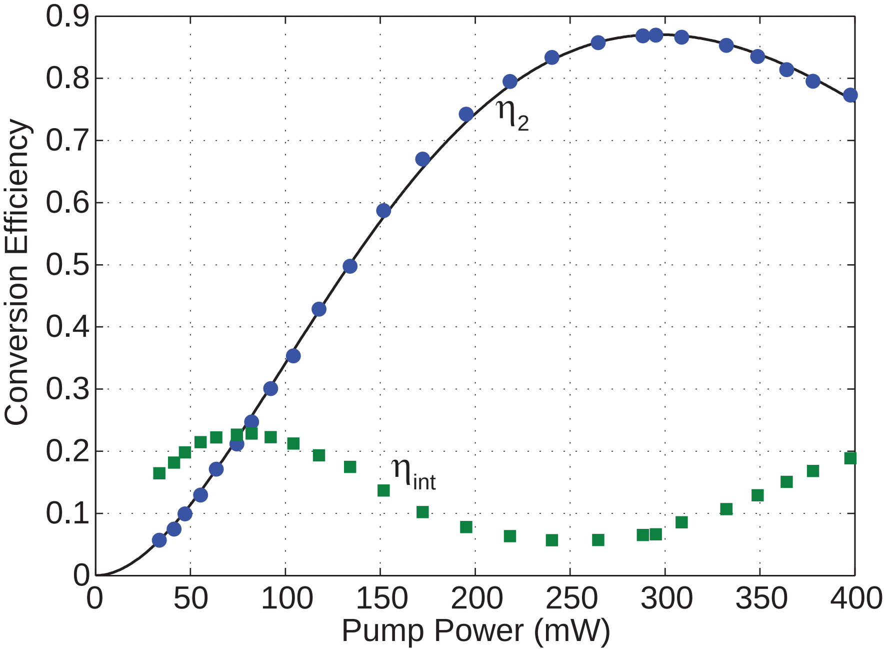

Figure 7.5: Measured internal conversion efficiencies η_2 and η_{int} versus pump power P_p and fit to Eq. (7.2).

telecom-band signal to the green spectral region via a two-step upconversion process using a single 1.8-μm pump. Using a picosecond pulsed single-photon-level signal we have demonstrated single-photon detection timing resolution below 70 ps, which may enable higher-data-rate quantum communications and quantum key distribution. If, using a narrow band filter such as a volume Bragg grating (described in Sec. 7.2), and the state-of-the-art PDM series Si SPAD, we could achieve 1.55 μm single-photon detection with system efficiencies of up to 35% at noise count levels below 100 s^{-1} and timing jitter below 40 ps, potentially enabling QKD with modulation rates of greater than 10 GHz over distances longer than 250 km.

7.1.3 Two-step downconversion of quantum light sources

In Chapter 6, we discussed frequency conversion devices for downconverting single-photons from InAs/InGaAs quantum dots from their emission wavelength near $\lambda_2 =$ 900 nm to a target wavelength λ_1 in the telecommunications band near 1550 nm. By

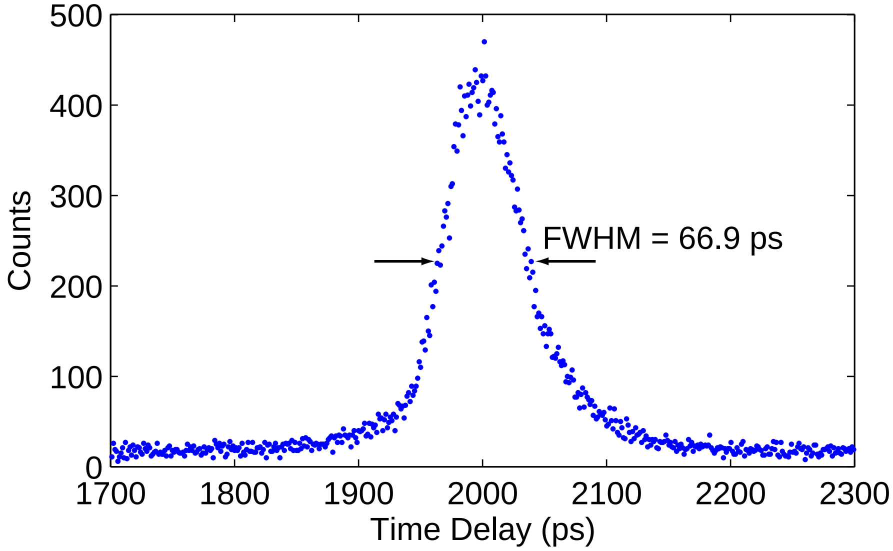

Figure 7.6: Timing histogram of 10-ps-pulsed 1.55-μm signal using two-step upconverter and id100 Si APD, showing system timing jitter of 66.9 ps.

energy conservation, this process requires a strong pump wave at $\omega_p = \omega_2 - \omega_1$, which yields $\lambda_p = 2.15$ μm. If one wishes to use a pump frequency $\omega_p < \omega_1$, one is therefore limited to input signal frequencies $\omega_2 < 2\omega_1$.

A great deal of research is being devoted to quantum emitters at frequencies in the visible and near-visible that do not satisfy this constraint. One notable example is the diamond nitrogen-vacancy (NV) color center, an intrinsic diamond impurity which when localized is a single quantum system [140]. There has been significant progress in fabricating nanostructures to enhance the radiative properties of NV centers [141, 142], as well as demonstrations of spin-photon entanglement [4] and coherent control of single spins [143]. Less well-developed but still promising defect centers include silicon-vacancy as well as Cr defect centers, all of which operate near 700 nm [140]. However, if one seeks to couple these sources to the telecommunications infrastructure, it requires a more sophisticated frequency conversion scheme.

To this end, we propose the use of a cascaded downconversion scheme, first discussed in [48], and illustrated schematically in Fig. 7.7(a). When the input signal is at a frequency $\omega_2 > 2\omega_1$, we consider a downconversion process in which a single

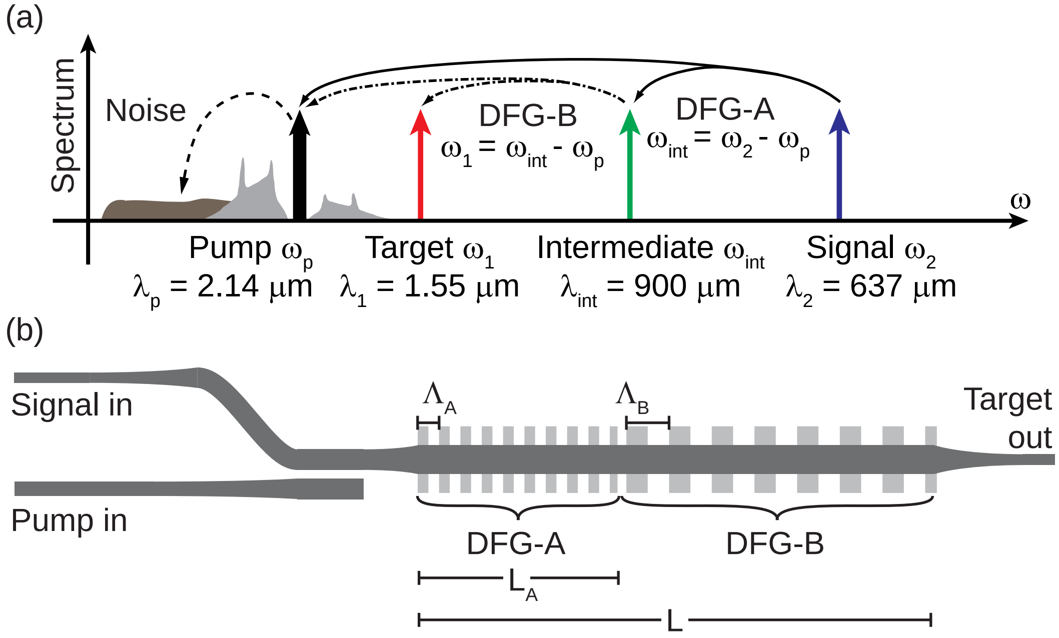
(a)
Spectrum
Noise
DFG-B
ω1 = ωint - ωp
DFG-A
ωint = ω2 - ωp
ω
Pump ωp
λp = 2.14 μm
Target ω1
λ1 = 1.55 μm
Intermediate ωint
λint = 900 μm
Signal ω2
λ2 = 637 μm
(b)
Signal in
Pump in
ΛA
ΛB
Target out
DFG-A
DFG-B
LA
L

Figure 7.7: (a) Schematic of frequencies involved in two-stage downconversion of single photons from a diamond NV center to the 1.5-μm telecom band; (b) schematic device design for two-stage downconversion.

pump at ω_p is used to convert the input signal to the target via an intermediate field at ω_{int}. From Fig. 7.7, we therefore have $\omega_p = (\omega_2 - \omega_1)/2$ and $\omega_{\text{int}} = (\omega_1 + \omega_2)/2$. A schematic PPLN waveguide for this process is shown in Fig. 7.7(b). The device will use an integrated directional coupler as discussed in Chapter 6 to combine the long-wavelength pump and short-wavelength single photons into the fundamental spatial mode of the mixing waveguide, where two sequential DFG processes will convert the signal photons at 637 nm to target photons at 1550 nm.

While diamond NV centers are touted as potential room-temperature qubits, the photon emission from NV centers is not ideal for frequency conversion applications. Even at cryogenic temperatures, NV-center emission is dominated by a phonon sideband with a width of approximately 100 nm centered around 700 nm. Zero-phonon emission occurs at a wavelength of 637 nm (for NV$^-$) and 570 nm (for NV^0) but even at 10 K the zero-phonon emission fraction is approximately 3% [141]. At cryogenic temperatures, the linewidths of the zero-phonon lines (ZPLs) are very narrow, suitable for frequency conversion, but near room temperature they broaden to several nm, reducing their overlap with the acceptance bandwidth of a down-conversion device. Nevertheless, the fabrication of photonic nanostructures in single-crystal diamond has enabled a strong Purcell enhancement of the spontaneous emission rate [142], with up to 70% of the emitted photons in the ZPL. These recent developments make the implementation of a cascaded frequency downconverter very promising.

7.2 Multichannel and time-frequency converters

In Sec. 7.1.2 we discussed the use of cascaded frequency upconversion to enable detection by low-timing-jitter APDs. Here, we explore the utility of using multiple pumps, either pulsed or cw, to upconvert an optical signal. Experiments in this section have been done in collaboration with Paulina Kuo and Xiao Tang of the Information Technology Laboratory at NIST [144].

7.2.1 Multichannel upconversion and applications

We consider a waveguide in which the following SFG processes can be simultaneously quasi-phasematched:

$$\omega_0 + \omega_{p1} = \omega_1 \tag{7.4a}$$

$$\omega_0 + \omega_{p2} = \omega_2 \tag{7.4b}$$

$$\vdots$$

$$\omega_0 + \omega_{pN} = \omega_N, \tag{7.4c}$$

where, as in Fig. 7.8, we imagine that a single-photon signal at ω_0 is undergoing simultaneous sum-frequency generation with N strong pumps at frequencies ω_{p1} to ω_{pN}. Considering now the simplest (non-trivial) case of $N = 2$, the coupled wave

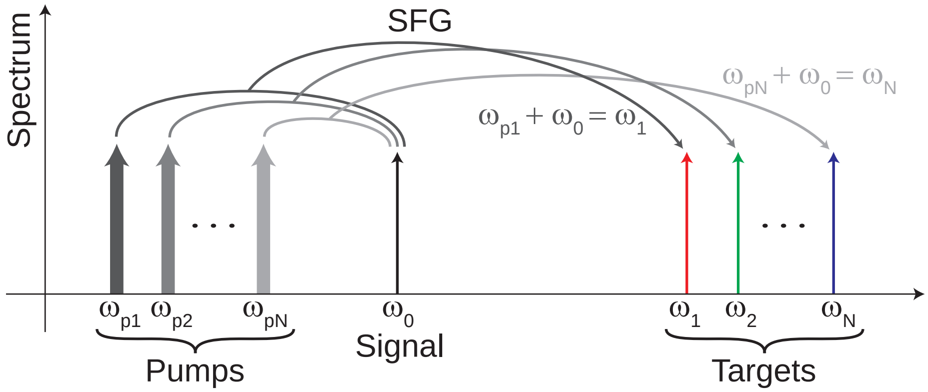
SFG
Spectrum
$\omega_{pN} + \omega_0 = \omega_N$
$\omega_{p1} + \omega_0 = \omega_1$
. . .
. . .
ω_{p1}
ω_{p2}
ω_{pN}
ω_0
Signal
Pumps
ω_1
ω_2
ω_N
Targets

Figure 7.8: Schematic of frequencies involved in multichannel upconversion.

equations for the photon fields (normalized as in Chapter 2), are written:

$$\frac{\mathrm{d}a_0}{\mathrm{d}z} = -\gamma_1 a_2 - \gamma_2 a_3 \tag{7.5a}$$

$$\frac{\mathrm{d}a_1}{\mathrm{d}z} = \gamma_1 a_1 \tag{7.5b}$$

$$\frac{\mathrm{d}a_2}{\mathrm{d}z} = \gamma_2 a_1 \tag{7.5c}$$

where the $\gamma_j = \sqrt{\kappa P_{pj}}$. The pumps at ω_{p1} and ω_{p2} are assumed to be undepleted (valid for the weak input signals we consider), the processes are both phasematched (which can be achieved using a phase-modulated QPM grating described below), and the propagation losses are negligible.

We seek to solve the Eqs. (7.5a) and determine the input-output relation for the photon annihilation operators at the output of the device. We start by taking the second derivative

$$\frac{\mathrm{d}^2 a_0}{\mathrm{d}z^2} = -(\gamma_1^2 + \gamma_2^2) a_0. \tag{7.6}$$

Substituting $\Gamma = (\gamma_1^2 + \gamma_2^2)^{1/2}$, this equation is solved to yield

$$a_0(z) = A \cos \Gamma z + B \sin \Gamma z. \tag{7.7}$$

We proceed to solve the remaining two equations and put in the initial conditions

$a_0(0)$, $a_1(0)$, and $a_2(0)$ to yield the input-output ($z = L$) relation. Defining normalized coupling constants $\bar{\gamma}_j = \gamma_j/\Gamma$, we find:

$$a_0(L) = a_0(0)\cos\Gamma L - \left[\bar{\gamma}_1 a_1(0) + \bar{\gamma}_2 a_2(0)\right]\sin\Gamma L, \tag{7.8a}$$

$$a_1(L) = \bar{\gamma}_1 a_0(0)\sin\Gamma L + a_1(0)\left(\bar{\gamma}_1^2\cos\Gamma L + \bar{\gamma}_2^2\right) + \bar{\gamma}_1\bar{\gamma}_2 a_2(0)\left(\cos\Gamma L - 1\right), \tag{7.8b}$$

$$a_2(L) = \bar{\gamma}_2 a_0(0)\sin\Gamma L + a_2(0)\left(\bar{\gamma}_2^2\cos\Gamma L + \bar{\gamma}_1^2\right) + \bar{\gamma}_1\bar{\gamma}_2 a_1(0)\left(\cos\Gamma L - 1\right). \tag{7.8c}$$

The input-output relations of Eq. (7.8a) can be easily generalized where we note that for N pumps, $\Gamma = (\sum_j \gamma_j^2)^{1/2}$, where $\sum_j \bar{\gamma}_j^2 = 1$. For an N-pump system, we can create probabilistic mixtures of photons at the target frequencies ω_1 to ω_N.

QPM design and device characterstics

To fabricate a multichannel upconversion device, we employed the QPM phase-modulation technique developed by Asobe and coworkers [138]. The phase modulation technique is one of several techniques that have been developed in order to engineer the phasematching profile of a device. In this technique, one applies a superstructure to the QPM grating by modulating the phase of the QPM pattern using a phase modulation function $\phi(z)$ that is periodic in z with period Λ_{ph}. The phase modulation consist of shifting position of a domain boundary z_n with respect to its nominal location $z_{n,0}$ of a periodic grating. In this formalism, the modulation phase $\phi(z_n) = 2\pi(z_n - z_{n,0})/\Lambda_G$. Via Fourier analysis, it can be shown that one obtains QPM peaks when the relation

$$\Delta k' = 2\pi\left(\frac{1}{\Lambda_G} + \frac{m}{\Lambda_{\text{ph}}}\right) \tag{7.9}$$

is satisfied for integer m. To choose the appropriate phase modulation function $\phi(z)$ we minimize a trial function given as

$$T = \sum_{m\in S}\left(\eta_m - \eta_m^{\text{targ}}\right)^2 \tag{7.10}$$

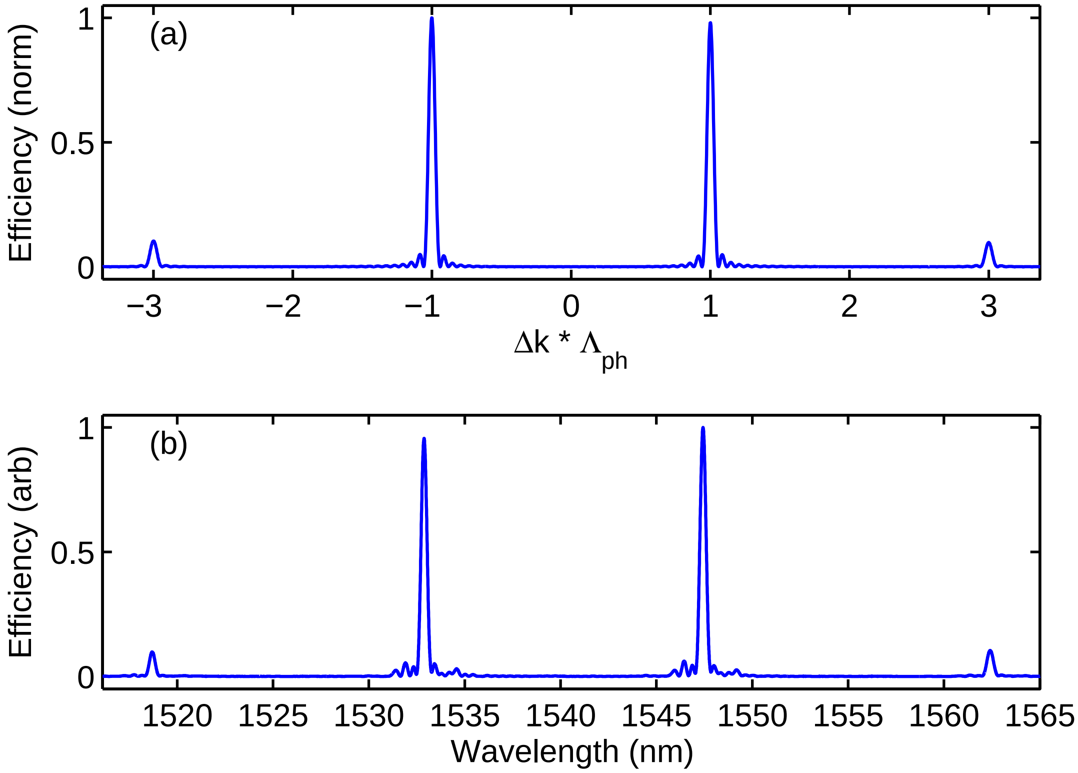

Figure 7.9: (a) Theoretical and (b) measured SFG efficiency for phase-modulated SFG device for $\lambda_0 = 1319$ nm.

where the sum is over integer m in the set S containing the desired QPM peak locations, η_m is the computed efficiency for a particular $\phi(z)$, and η_m^{targ} is the desired efficiency. For the two channel device we fabricated, $S = \{-1, 1\}$, $\eta_{m=\pm 1}^{\text{targ}} = 0.5$, and $\eta_m^{\text{targ}} = 0$ for all other m. The use of a simplex convex optimization algorithm (the `fminsearch` function in Matlab) was successful at optimizing $\phi(z)$ for several different functional parametrizations (e.g. Fourier series and power series). The simple two-channel structure did not require such a complex optimization technique, but will enable the design of more complex devices (including asymmetric about $m = 0$, and unequal peak-height) structures with more channels [145]. A calculated QPM tuning curve is shown in Fig. 7.9(a).

The channel separation (which we define as the wavelength difference between the two QPM peaks for $m = \pm 1$) is controlled via a choice of the phase modulation

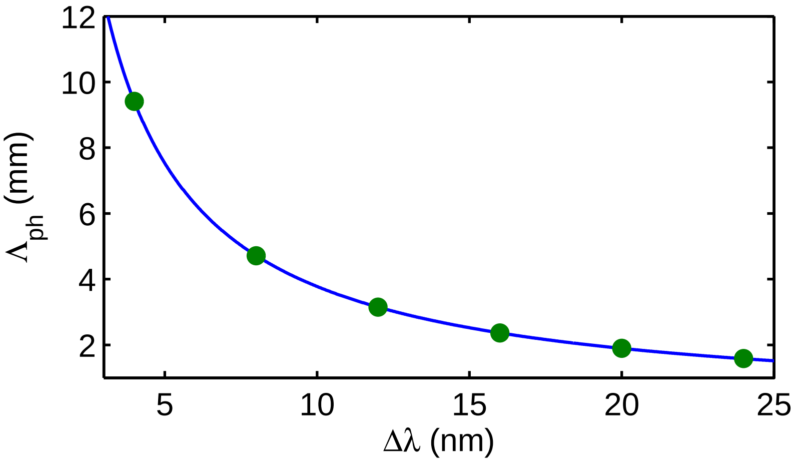

Figure 7.10: Required phase modulation period Λ_{ph} for SFG between two pumps with wavelengths spaced by $\Delta\lambda$ around 1550 nm and a 1310-nm signal (circles) with power law $\Lambda_{\mathrm{ph}} = a(\Delta\lambda)^{-1}$ fit.

period. The required phase-modulation period for a two-channel device is found by rearranging Eq. (7.9)

$$\frac{1}{\Lambda_{\mathrm{ph}}} = \frac{\Delta k'(\Delta\lambda)}{2\pi} - \frac{1}{\Lambda_G}. \tag{7.11}$$

We plot the result of Eq. (7.11) in Fig. 7.10. The $\Delta k'$ values were computed using the simulated dispersion data for RPE waveguides with 1.85 μm proton exchange depth (circles), and are found to be fit accurately by a power law $\Lambda_{\mathrm{ph}} = a(\Delta\lambda)^{-1}$, with $a = 37.4$ mm/nm. For our devices we chose target channel separations of 5, 10, and 15 nm, which implied phase modulation periods of 7.1, 3.94, and 2.56 mm.

We fabricated two-channel upconversion RPE PPLN waveguides for SFG between a 1.3 μm signal and two 1.55-μm-band pumps using the techniques discussed in Chapter 3. The devices were antireflection coated (Foreal, Inc.) for wavelengths of 1310 and 1550 at the input between $\mathrm{LiNbO_3}$ and optical fiber, and for 1310, 1550, and 710 nm at the output between $\mathrm{LiNbO_3}$ and air. The devices were fiber pigtailed as well, and were measured to have total optical throughput of -1.3 dB at 1550 nm and -2.4 dB at 1319 nm.

For preliminary experiments described below, we chose a device with $\Delta\lambda = 15$ nm. A QPM tuning curve is shown in Fig. 7.9(b), where we can see excellent agreement

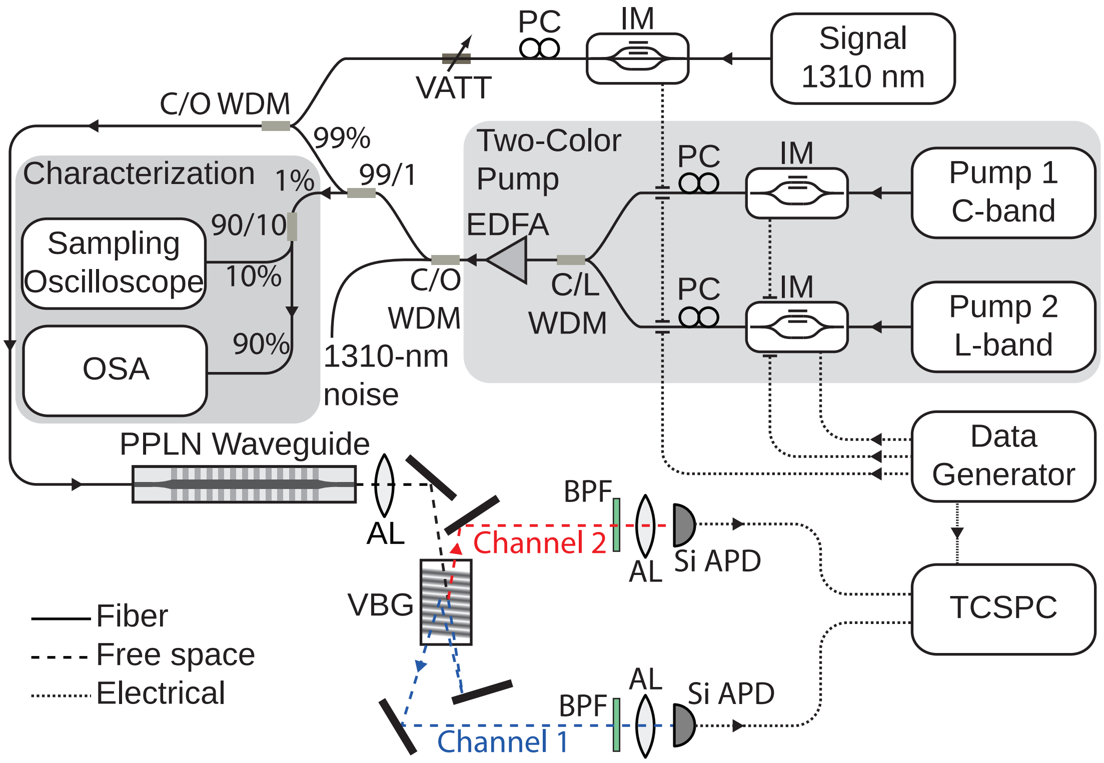
PC
IM
Signal
1310 nm
VATT
C/O WDM
99%
99/1
1%
Characterization
90/10
Sampling
Oscilloscope
10%
OSA
90%
Two-Color
Pump
EDFA
C/O
WDM
C/L
WDM
1310-nm
noise
PC
IM
Pump 1
C-band
PC
IM
Pump 2
L-band
Data
Generator
PPLN Waveguide
AL
BPF
Channel 2
AL
Si APD
VBG
TCSPC
Fiber
Free space
Electrical
AL
Si APD
BPF
Channel 1

Figure 7.11: Experimental setup for multichannel upconversion system.

with theory. The device has two QPM channels with phasematching of 1532.88 and 1547.43 nm.

We incorporated the waveguide into an upconversion single-photon detector, a schematic of which is shown in Fig. 7.11. To pump both upconversion channels simultaneously, two pump lasers were used. As will be described in Sec. 7.2.2, the pumps were modulated using electro-optic intensity modulators (IM). The two pumps were combined using a C/L-band WDM and were amplified using an EDFA. Optical noise in the 1.3 μm band coming from the EDFA was filtered using a series of three 1550/1310-nm WDMs. After passing through a tap coupler, the combined dual-channel pump was then combined with the single-photon level signal at 1.3 μm with another 1550/1310 WDM, and the combined pump and signal radiation was incident on the fiber pigtail. Polarization controllers were used for both pumps and the signal to align the input light to the TM polarization of the waveguide.

Following the waveguide, an aspheric lens (AL) coated was used to collimate the output radiation from the waveguide. To separate the outgoing pump light and filter the two upconverted channels at λ_1 and λ_2, we used a reflective volume Bragg grating (OptiGrate, Inc.). The reflective VBG acts as a narrowband filter ($\Delta\lambda < 0.05$ nm) where the reflected band depends on the angle of incidence. The VBG was aligned such that the long-wavelength channel at λ_2 had high reflectivity back through the input facet. The upconverted light at λ_1 passed through the VBG and was directed back in using a mirror at a slight angle so that high reflection was achieved back through the VBG. The two upconverted channels were then directed to two Perkin-Elmer SPCMs, where a 20-nm bandpass filter at the entrance of the SPCMs blocked any stray light or parasitic pump second harmonic radiation[2]. Not shown in Fig. 7.11 are reimaging systems for each channel used to adjust the spot size incident on the aspheric lenses before the APDs. The VBG performance depends critically on the focusing of the incident beam (the reflectance is maximized for a perfectly collimated beam) and we thus needed an additional focusing degree of freedom when compared with the upconversion detectors discussed in Chapter 5.

We next measured the system PDE and NCR of each channel, separately. The results are shown in Fig. 7.12, with fits of the PDE to $\eta_{\text{tot}}(P_p) = \eta_0 \sin^2(\pi/2\sqrt{P_p/P_{\text{max}}})$. We find a maximum PDE of 32% for channel 2 and 25% for channel 1. The PDE for channel 1 is lower due the additional optical path needed as it is the channel transmitted through the VBG. A major improvement of these results when compared with earlier 1.3 μm-band upconversion detectors is the very low noise count rate–here, just barely above the intrinsic dark count rate of the SPCMs, compared with greater than 10^4 counts/s in a previous experiment with a PPLN waveguide [30]. This reduction in the noise is due to the very narrowband reflectance of the VBGs. In this system, the noise is primarily due to upconverted anti-Stokes Raman photons generated by the strong pump, which fill the acceptance bandwidth of the upconverter. Here, the

---

[2] An unintended consequence of the phase-modulated QPM design was the appearance of several parasitic accidental QPM peaks for SHG of the pump radiation. We chose the operating wavelengths such that these peaks were avoided, but even away from these peaks there were still up to a few tens of microwatts of generated second harmonic radiation when pumping with approximately 100 mW of pump light.

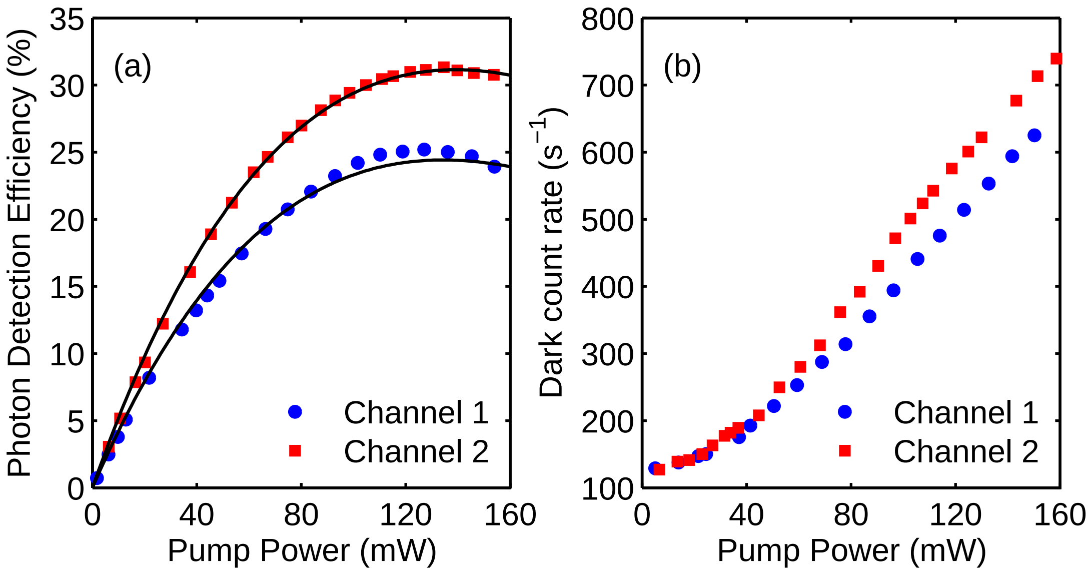

Figure 7.12: Measured two-channel upconversion detector (a) PDE, and (b) noise count rate.

VBG provides a filter narrower than the acceptance bandwidth such that most of the noise photons are eliminated.

Applications as a frequency-shifting variable beam splitter

When both pump frequencies are active at the same time, the dual-channel upconverter followed by spectral filtering acts as a frequency shifting variable beamsplitter. Beamsplitters have several uses in quantum optics; we demonstrated the use of the dual-channel upconverter for two purposes: (1) the splitting of high-count-rate signals to enable single-photon count rates above the dead-time-limited value of a single detector, and (2) the measurement of the second-order correlation function $g^{(2)}(\tau)$ of both coherent and quasi-thermal light sources.

As discussed in Sec. 5.1, the maximum count rate of an APD is determined by the detector dead time τ_D as $R_{\max} = \tau_D^{-1}$. As the incident photon rate R_{inc} begins to approach $R_{\max}$ the detector begins to saturate at this maximum count rate (the details of the saturation depend on the statistics of the input light). We consider a single photon at ω_0 incident at the input of the device. When the pump powers P_{p1}

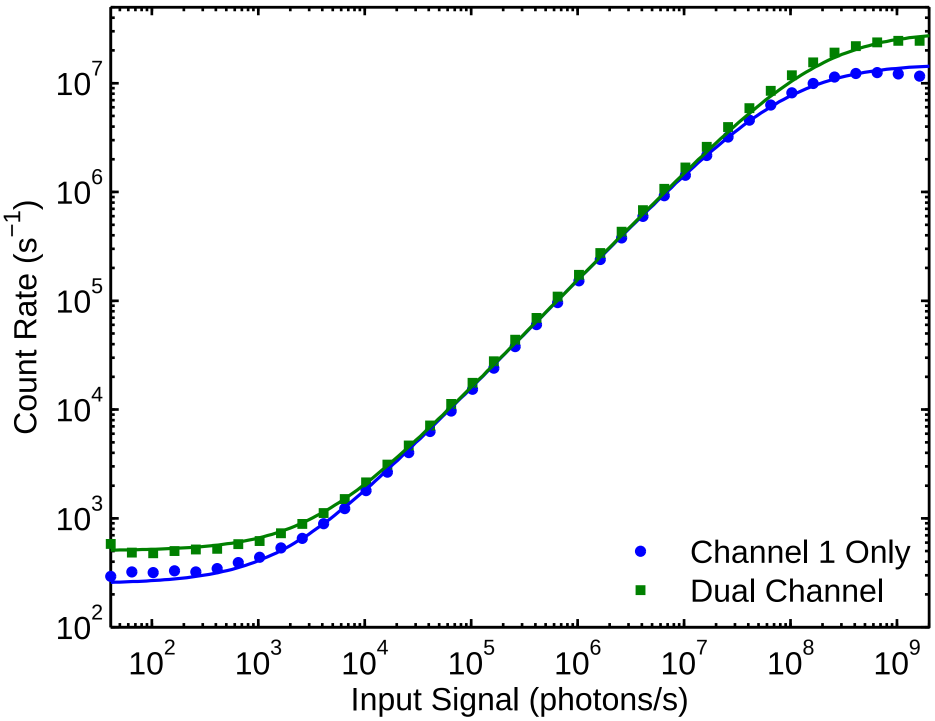

Figure 7.13: Measured count rate R versus input signal photon flux R_{inc} for a single-channel (blue circles) or dual-channel (green squares) device, where we observe a saturation rate of $2R_{\text{max}}$ for the two-channel detector. The solid curves are simulated counting statistics for coherent light.

and P_{p2} are chosen such that $\Gamma L = \pi/2$ and $\bar{\gamma}_1 = \bar{\gamma}_2$, we find, with 50% probability that photon is converted to ω_1 or ω_2. Therefore, much like a classical beamsplitter, the dual-channel upconverter will probabilistically divide the incident 1.3-μm signal to the two upconverted channels where the signal can be detected by two APDs.

We have measured the saturation of a Perkin-Elmer SPCM by varying R_{inc} and measuring the count rate R of a single detector. The input signal R_{inc} at $\lambda_0 = 1302$ nm was controlled via a programmable optical attenuator from a level of 41 photons/s to 2×10^9 photons/s. With only pump 1 turned on, we measured the count rate R_j on both channels $j \in \{1, 2\}$: the count rate R_1 is shown as blue circles in Fig. 7.13. The solid blue curve is a simulation of the expected counting statistics of coherent light (with Poissonian photon arrival statistics) assuming a detector dark count rate

$D = 250\ \mathrm{s}^{-1}$ and a dead time of 67 ns. By comparing the rates R_1 and R_2 with only pump 1 turned on, we measured a channel-to-channel crosstalk of -44 dB, which is likely due to a combination of amplified spontaneous emission (ASE) from the EDFA and imperfect isolation of the VBG channels.

With both pumps turned on, we measured the summed count rate $R_s = R_1 + R_2$ after equalizing the count rates on each detector, and at the same overall conversion efficiency as in the pump-1-only case. The observed R_s versus R_{inc} is plotted as green squares in Fig. 7.13, along with an analogous simulation of the counting statistics. We see that at low R_{inc}, the dual-channel case has a DCR of approximately $2D$, and saturates at high $R_s = 2R_{\max}$. From this result, we can extrapolate that for an N-pump upconverter, the system count rate R_s would saturate at $NR_{\max}$ at the expense of a DCR of ND.

A common application of beamsplitters in quantum optics is to split a signal to two detectors such that the second-order correlation function $g^{(2)}(\tau)$ of a light source can be measured (see Chapter 6 for discussion). We have used the dual-channel converter as an upconverting beamsplitter and have measured the $g^{(2)}(\tau)$ of both a coherent source and a pseudothermal source. In the measurement, we used the time-tagging mode of a time-correlated single-photon counting (TCSPC) system (PicoHarp 300E) to record the arrival times of photons at APD1 and APD2 where the pump powers P_{p1} and P_{p2} were chosen to equalize the two count rates. The $g^{(2)}(\tau)$ was then calculated offline upon completion of a 1-minute integration at approximately 5×10^4 counts/s/channel. The results for the coherent source are shown in Fig. 7.14. As expected, due to the Poissonian arrival statistics of the photons from a laser, $g^{(2)}(\tau) = 1$ for all τ.

It has been shown that by passing a laser beam through (or reflecting a laser beam off) a moving diffuser, one can create pseudothermal light source with a variable correlation time [146, 147]. We formed a pseudothermal source by coupling the signal laser into free space and collecting the scattered light off a rotating ground-glass diffuser. By changing the geometry of the collection or the rotation speed of the diffuser different coherence times $\Delta\tau$ can be realized. Our results for the pseudothermal source are shown in Fig. 7.14(b), where we see a bunching peak with a FWHM

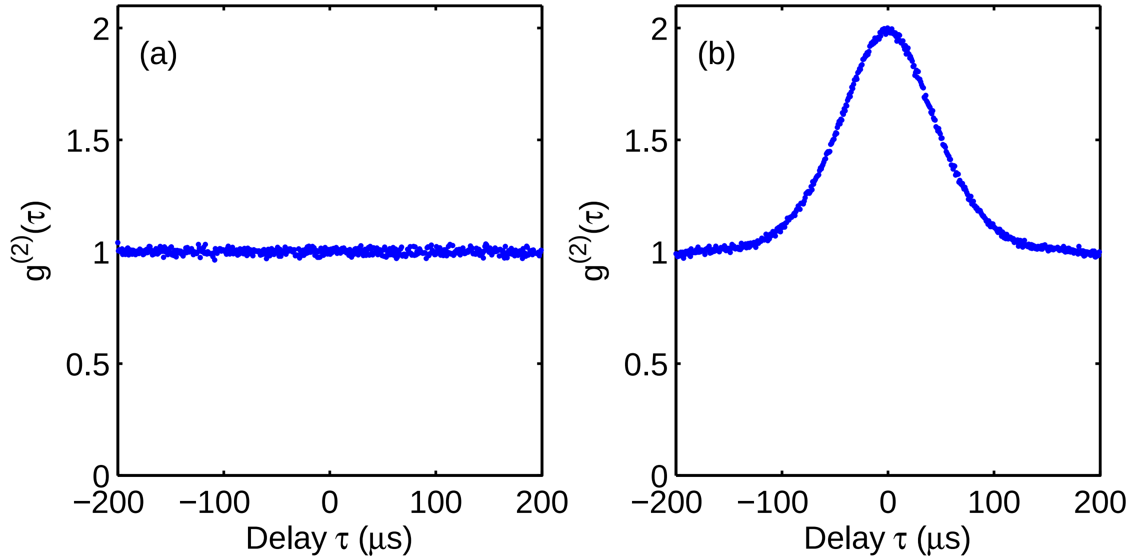

Figure 7.14: Measured second-order correlation functions $g^{(2)}(\tau)$ of (a) coherent and (b) quasi-thermal light sources using dual-channel upconverter.

width of 98 μs.

The results obtained by measuring a $g^{(2)}(\tau)$ using a dual-channel upconverter are presumably no different than would be obtained via a standard technique using a classical beam-splitter. One benefit is the ability to easily and rapidly change the "splitting ratio" via control over the pumping ratios $\bar{\gamma}_1$ and $\bar{\gamma}_2$. That we have observed the possibility of probabilistically upconverting to one state or another has interesting consequences when we imagine manipulating nonclassical states of light with this device. If a single photon at ω_0 is incident on the device, we can write the input state as

$$\begin{aligned}|\psi\rangle_{\text{in}} &= |100\rangle = |1\rangle_{\omega_0} \otimes |0\rangle_{\omega_1} \otimes |0\rangle_{\omega_2} \\ &= a_0(0)^\dagger |000\rangle. \end{aligned} \tag{7.12}$$

After propagating through the dual-channel device, using the results calculated in Eq. (7.8a) we find that the output state

$$|\psi\rangle_{\text{out}} = a_0(L)^\dagger |\psi_{\text{in}}\rangle = \bar{\gamma}_1 |010\rangle + e^{i\phi_{\text{rel}}} \bar{\gamma} |001\rangle \tag{7.13}$$

which implies that the photon has been converted to a superposition state of two different frequencies. If the relative phase ϕ_{rel} between the two pumps can be controlled, coherent superpositions of the photon can be created in λ_1 and λ_2, which could be a novel qubit in quantum information processing systems.

7.2.2 Upconversion with multi-wavelength sampling

In the previous section we discussed applications of a multichannel converter with the pump sources on simultaneously. In that demonstration, the splitting of an input signal to multiple output ports happened stochastically. If, however, the pumps were turned on and off via external modulators controlled by a pattern generator, one can deterministically control the output channel via, for example, switching the pumps on and off sequentially. An upconversion detector using multi-wavelength sampling techniques has recently been demonstrated by Ma and coworkers at NIST [148].

The primary motivation for a multi-wavelength sampling upconversion detector is to enable the detection of single-photon-level signals modulated at rates higher than the timing jitter Δt of a given detector would allow. The timing jitter sets the maximum clock rate for a QKD system, and with APD single-photon detectors the long tails of the timing response (see Fig. 7.16(a)) would lead to high intersymbol interference when a system is clocked at rates above $f_c \approx 1/\Delta t \approx 1$ GHz. The use of N switched distinctly colored pumps enables the subdivision of this 1-ns bin into N sub-bins, enabling a time-division demultiplexing of a signal that can now be clocked at $N f_c$.

Our experimental setup is diagrammed schematically in Fig. 7.11. A pulse-pattern generator (PPG, Tektronix DTG-5274) drives electro-optic intensity modulators (IM) for the signal and each pump. The timing diagram for the experiment is shown Fig. 7.15. After combining the two pumps and signal in the waveguide, the resulting dual-channel SFG products are separated and filtered by the VBG and routed to two Si APDs (Perkin Elmer SPCM-AQR14). The wide channel separation would make possible a filtering scheme either using a holographic diffraction grating (as in [148], but with significantly shorter optical path required), or a Brewster prism. One

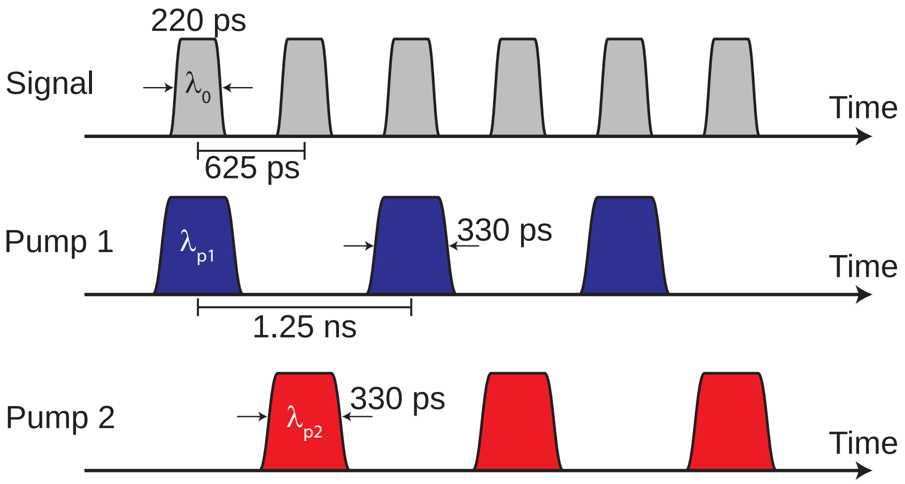

Figure 7.15: Timing diagram for detection of high-clock-rate signals via multi-wavelength sampling.

difficulty about working with the large channel separation is that the shape of the EDFA gain spectrum must be carefully considered to balance the conversion efficiency between the two channels.

We first measured the timing jitter of the APD used in the experiment, by modulating the signal into a short pulse every 10 clock cycles, and using the pulsed pump to upconvert it. Our data is shown in Fig. 7.16(a) as green dots, where we observe a FWHM jitter of 380 ps, and FW1%M timing jitter of 1.05 ns. The primary impediment to using this detector for quantum communication schemes is the long timing jitter tail, which is due to carrier diffusion effects [149]. Using a single pump modulated at the same rate as the signal (1.6 GHz), we recorded a timing histogram which is shown as the black dots in Fig. 7.16(a). The background level of approximately 10^{-3} normalized counts is due to residual pump and signal transmission due to imperfect extinction of the EOMs. Due to the detector timing jitter, a photon arriving within one clock cycle will have a large probability of producing an electrical pulse that will register in an adjacent time bin, which will result in errors in the quantum communication protocol. We can calculate this error probability by comparing the probability of assigning a count to the wrong time bin to the count statistics for a single pulse. For the case of detecting a 1.6-GHz-modulated signal with a single

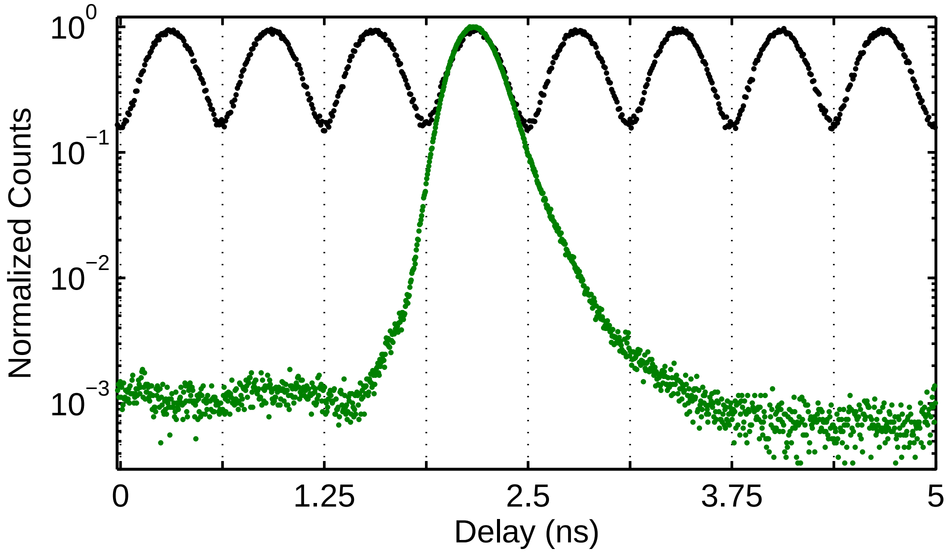

(a) Measured counting histograms for an isolated 1302-nm pulse (green dots) showing a long tail which results in high intersymbol interference for a 1.6-GHz clock signal measured using only one channel (black dots).

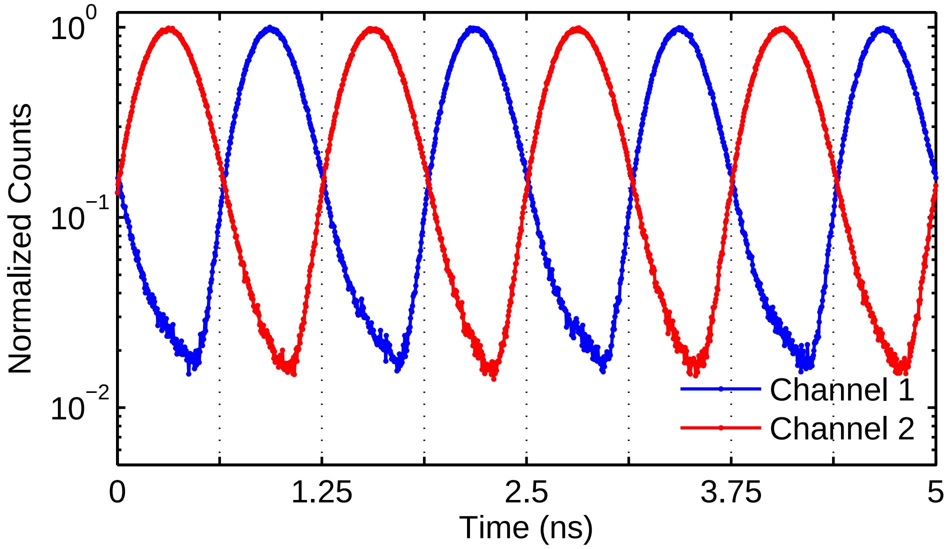

(b) Measured counting histograms for a 1.6-GHz clock signal using a dual-channel alternating pump scheme, showing significantly improved intersymbol interference compared with a single-channel detection scheme.

Figure 7.16: Timing performance of dual-channel upconversion detector.

detector, we find an error probability $P_e = 5.7\%$.

We next implemented a modulation scheme like that shown in Fig. 7.15. A 1302-nm clock signal at 1.6 GHz was upconverted via an alternating pump such that each detector is only receiving pulses at a rate of 0.8 GHz. We recorded timing histograms for both detectors, the results of which are shown in Fig. 7.16(b). We now observe that due to the effects of downsampling, the error rate is reduced by more than an order of magnitude: we calculate a P_e of 0.38% (0.41%) for Channel 1 (Channel 2). As in [148], we have also used the system to detect complex pulse sequences.

7.2.3 Future work

We have described the use of a dual-channel upconverter for the purposes of either creating frequency superpositions or detecting high-clock-rate modulated signals for communications. Our experimental efforts have focused on a two-channel upconverter made via phase-modulated QPM techniques. Such techniques are easily adaptable to more channels [145], and, as discussed in [148], with N pumps one can increase the system clock rate to $N/\Delta t$.

A difficulty when considering increasing the number of channels in a multichannel upconversion system is that one needs ever more lasers and modulators to expand the system. A more modular approach may be possible based on optical pulse shaping techniques that have been heavily exploited for arbitrary waveform generation, among other application [150]. In this technique, a high-bandwidth pulse train (e.g. femtosecond pulses from a modelocked laser) are manipulated in the Fourier domain. If the modelocked laser pulses have been carrier-envelope-phase (CEP) stabilized [151], then one can envision the creation of the frequency-entangled states with stable phase relationships between the different components of the superposition.

The multi-wavelength sampling upconverter can in some senses be viewed as a discrete analogue of a time-frequency converter. In a time-frequency converter, each temporal slice of an input signal is linearly mapped to a specific frequency. This mapping corresponds to the imposition of a quadratic phase in time, which is the space-time analog of a lens and is the central component of temporal imaging systems

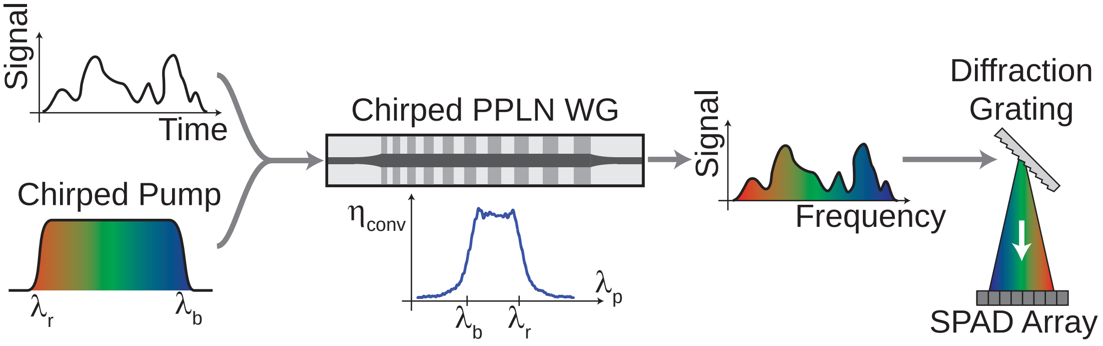

Figure 7.17: Schematic of a single-photon time-frequency converter utilizing SFG of an input signal with a chirped pump pulse in a chirped QPM grating.

[152]. Temporal imaging systems have most often been used to magnify an ultrafast waveform in time, such that it can be recorded with a photodiode and standard oscilloscope; temporal imaging systems with magnifications of up to 450× have been reported [153].

We propose a single-photon time-frequency converter, a schematic of which can be seen in Fig. 7.17. A chirped pump (created, e.g. by dispersing a femtosecond pulse in a length of optical fiber) is combined with an weak input signal with rapid temporal features. A SFG interaction in a chirped waveguide (with QPM bandwidth broad enough to support the entire chirped pump) maps the temporal features of the input signal onto frequency. The chief difference between this system and ordinary temporal imaging systems is the use of a diffractive optic and detector array to detect the upconverted signal. This configuration allows one to map each array element onto a particular slice in time, such that even if each detector element has a timing jitter large compared to the temporal features of the signal, the features can be recorded statistically by recording many shots. SPAD arrays with as many as 128×128 elements have been reported [154]. We believe this system will enable quantum communications systems to begin to approach the data rates of classical communications systems: the main impediment of detector timing jitter is overcome by the effective time-to-space conversion provided by this system.

Chapter 8

Conclusion

8.1 Summary of contributions

The main theme of this dissertation has been the development, application, and analysis of devices and systems for frequency conversion of single-photon signals. Here I shall give an overview of the main contributions of the work described in this dissertation, as well as a few projects to which I have contributed that are not covered in this dissertation.

The analysis of noise processes in quantum frequency converters was a principal subject of the work described. As discussed in Chapter 4, there are two primary noise sources in QFC devices. The first source is spontaneous parametric fluorescence, whereby a pump photon splits into a signal–idler pair in which the signal photon overlaps spectrally with either the acceptance bandwidth of the converter or the detection window. In [48], we showed that random duty-cycle errors in RPE PPLN waveguides substantially increases the rate of parametric fluorescence. Fabrication tolerances were derived, and it was shown that for typical experimental configurations, random duty-cycle errors must be kept to a level $\sigma_l/l < 1\%$ in order to achieve low-noise performance. Parametric fluorescence noise was measured in two ways, both directly in the 1.5-μm band by a InGaAs APD, and via upconversion. In [75], we also described a measurement of random duty-cycle errors in PPLN devices via direct imaging, and obtained a result ($\sigma_l/l \approx 8\%$) that was consistent with a measurement of the QPM pedestal via a careful measurement of SHG in a waveguide.

The second noise source in QFC devices is spontaneous Raman scattering. In Sec. 4.2, we presented an analysis of spontaneous Raman scattering in $LiNbO_3$ samples and waveguides. The Raman spectrum of $LiNbO_3$ was found to decay much more slowly at high frequency shifts than would be expected based on a sum of Lorentzians, and these measurements were confirmed by noise measurements in an upconversion detector [67]. However, a synthesis of the analyses of both noise sources indicates that choosing a pump wavelength substantially longer than the signal wavelength (or equivalently, $\omega_p < \omega_1$) is highly effective at reducing the impact of these noise processes.

The primary technological interest of QFC has been upconversion single-photon detection. Single-photon detectors for the 1.5-μm telecom band based on InGaAs APDs suffer severe drawbacks when compared with Si APDs for visible and near-visible light. Upconversion of 1.5-μm signals allows detection using Si, but preliminary implementations have exhibited noise count rates well above 10^5 counts/s due to spontaneous scattering [29, 30]. In Chapter 5 and in [67], we demosntrated lower-noise single-photon detection using a long-wavelength pump at $\lambda_p \sim 1850$ nm. Our system exhibited greater than 99.99% depletion efficiency, 86% net internal conversion efficiency and a system detection efficiency of 37%, with noise counts as low as 10^3 counts/s. The spectral dependence of the noise count rate was found to be consistent with noise-photon generation by spontaneous anti-Stokes Raman scattering. We also demonstrated, in Sec. 5.4, an ultra-low-noise upconversion single-photon detector for signals in the 1.08-μm band, which are important for proposed quantum information processing schemes based on neutral donors in Si. This detector used a 1.55-μm-band pump and achieved internal conversion efficiencies of 81% and very low noise count rates of approximately 30 counts/s, due to to the very large frequency difference between the signal and pump.

While it had been realized in the first papers on QFC that quantum-state down-conversion was possible, these devices were not developed until much more recently. Most candidate systems for implementing quantum network nodes operate with optical transitions in the visible or near-visible spectral range, therefore requiring a frequency conversion technique to enable long-haul quantum communications based on transmission through optical fiber at 1.5 μm. A particularly promising quantum node candidate consists of an electron spin in an InAs/GaAs self-assembled quantum dot. In Chapter 6 we developed a donwconversion quantum interface, whereby the single photons emitted from the quantum dot at $\lambda_2 = 910$ nm were mixed with a strong pump at $\lambda_p = 2.2$ μm to produce a target field at $\lambda_1 = \left(\lambda_2^{-1} - \lambda_p^{-1}\right)^{-1} = 1.56$ μm. We generated a ps-pulsed 2.2-μm source based on DFG in a bulk PPLN crystal, and combined the 2.2-μm pulses with the quantum-dot single photons in an RPE PPLN waveguide for downconversion. The resulting single photons at 1.56-μm were detected using a superconducting single-photon detector. The use of picosecond conversion pulses shaped the single-photon emission, as observed by time-resolved measurements. Due to the large frequency difference between the pump and target frequencies in this experiment, noise counts were kept to a level below approximately 1 count/s. A measurement of the intensity cross-correlation of the downconverted signal showed a near perfect preservation of the single-photon character of the quantum dot emission. Additionally, we showed that the downconversion interface was compatible with coherent control of the quantum dot spin via the observation of Rabi oscillations. These characteristics enabled, to our knowledge for the first time, generation and verification of entanglement between the solid-state matter qubit (the quantum dot spin) and a telecom-band single photon, in results not described in this dissertation. We believe that the downconversion technique provides a route towards long-distance quantum communications based on quantum dots.

Chapter 7 described two novel device concepts moving past the one-step up- and downconversion of photons usually considered to be the limitations of quantum frequency conversion. Since with RPE PPLN waveguides it is possible to achieve near-unity conversion efficiency with relatively modest pump powers of ~ 100 mW, it is also possible to incorporate two conversion steps within the same waveguide, using two QPM gratings, to achieve larger frequency excursions while still maintaining low-noise operation. In the first demonstration of this concept [65], we used a 1.8-μm pump to upconvert a 1.55-μm input signal to the green spectral range in a two-stage conversion process, which enabled efficient, low-noise, and low-timing jitter detection of a pulsed 1.5-μm signal through the use of a thin-junction Si APD single-photon detector. We also proposed the use of a cascaded frequency converter as a technique for downconverting single photons from NV centers in diamond (at a wavelength of $\lambda_2 = 637$ nm) to the 1.5 μm telecom band through a two-stage downconversion technique. As low-noise frequency conversion is only possible with long-wavelength pumping, it is impossible to achieve low-noise conversion when $\omega_2 > 2\omega_1$ in a single step. The use of cascaded frequency conversion eliminates this constraint, enabling possible uses of this technique even for extremely large frequency translations, for example between UV photons emitted from trapped-ion qubits and the 1.5-μm telecom band.

The second device concept was multichannel frequency conversion. In this configuration, multiple pumps can be used to either probabilistically or deterministically convert an input signal to one of several output frequencies. As discussed in Sec. 7.2, we demonstrated the concept with a two-channel upconverter for converting 1.3-μm single-photon signals to two wavelengths near 710 nm. Combining the two channel converter with alternating pumps and a spectral filter at the output, we demonstrated a multi-wavelength sampling experiment whereby the timing-jitter-induced maximum clock rate of a single-photon communication system could be bypassed by the effective time-to-space conversion provided by the multichannel device. Additionally, we used a volume Bragg grating to filter the upconverted emission. The narrow bandwidth (0.04 nm) of the VBG compared with the acceptance bandwidth of the device (0.3 nm) enabled a strong suppression of noise counts due to anti-Stokes Raman scattering: we measured a noise count rate of approximately 500 counts/s [144], a factor of 30 lower than previously observed with these wavelengths [30]. We also proposed a technique to extend the discrete-time time-to-space converter to continuous time, potentially enabling very high-bandwidth quantum communications through time-division multiplexing or pulse-position modulation.

My initial projects in the Fejer group were focused on modeling a synchronously pumped OPO for terahertz generation. A ps-pulsed 1064-nm laser pumped a type-II PPLN crystal producing signal and idler beams spaced by the desired THz frequency. The signal and idler then interacted to produce the THz radiation in an QPM GaAs crystal placed inside the OPO cavity. The modeling involved both $\chi^{(2)}$ and $\chi^{(3)}$ nonlinear effects, dispersion, cavity phase, and multiple wave-mixing. The measured properties of the intracavity pulses were found to agree well with the model, and enabled a more detailed understanding of possible improvements to the THz generation efficiency [155]. I additionally assisted in the modeling and experimental demonstration of supercontinuum generation in QPM waveguides [90, 91], further details of which can be found in the dissertation of Chris Phillips [156].

8.2 Outlook and future directions

The results obtained during the course of this research suggest a number of potential future directions. As quantum communication techniques become more sophisticaed as the field develops, one imagines that the same sorts of functionality that $\chi^{(2)}$ mixers bring to classical communications systems will find analogous applications in the quantum realm. These classical techniques have been reviewed in [9], and here we outline a few exciting future opportunities.

As the fabrication model for APE and, subsequently, RPE waveguides developed, it becamse possible to build complex integrated optical circuits with wavelength conversion functionality. Linear-optics quantum computing [98], which has to date been attempted largely using bulk optics with limited approaches to large-scale scalable information processing, could make use of such integrated functionality in which not only the interferometer but the photon source (based on SPDC) could be integrated onto the same chip [157]. The ability to do high-efficiency fiber coupling with RPE waveguides also facilitates outcoupling to the needed single-photon detectors.

The possibilities outlined in the general idea of quantum waveform conversion offer intriguing possibilities when combined with the quantum dot single photon source [158]. Quantum dot photons are long ($\sim$ ns) on communications timescales: mixing the single-photon with a chirped pump to increase its bandwidth, followed by compression using dispersion, can create shorter single-photon wavepackets which could then be used to increase the transmission bandwidth of quantum communications systems.

Lastly, all the work described in this dissertation has been done in the $LiNbO_3$ material system. QPM devices based on orientation-patterned (OP) zincblende semiconductors have made tremendous progress in recent years [159] . In addition to the high nonlinearity of orientation patterned semiconductors, a critical point is that they lack birefriengence. As such, birefringent phasematching is impossible in semiconductors, but the lack of birefringence opens up intriguing possibilities for polarization-diverse entangled-photon generation and quantum frequency conversion if QPM is possible. As a classical example, optical parametric oscillation with a depolarized pump has been demonstrated [160]. It would surely be interesting to study the polarization properties of spontaneous parametric downconversion from OP semiconductor devices. With the recent development of OP-GaP [161], such applications now become feasible at customary wavelengths for quantum optics in the visible and near-infrared where good single-photon detectors exist.

Additionally, as ferroelectrics can only achieve QPM for one polarization at a time, polarization diversity has typically been achieved by using two crystals back-to-back [36]. With semiconductor-based QFC devices, both polarizations can be converted within the same device, which should enable preservation of polarization entanglement without a need for two devices. As material and device quality continues to improve, orientation-patterned semiconductors will be an interesting platform for quantum frequency conversion.

Appendix A

Efficiency pedestal in QPM devices with random duty-cycle errors

In this Appendix, we calculate the ensemble-averaged statistical properties of the spatial frequency pedestal that arises due to RDC errors. We consider a three-wave difference-frequency generation (DFG) process involving continuous, plane-waves with negligible signal gain or pump depletion. This formulation, combined with an input noise spectrum, can provide a semiclassical description of spontaneous parametric fluorescence as discussed in Chapter 4. Our results are also directly applicable to second harmonic generation (SHG) when the first harmonic is undepleted.

Under the above assumptions, the idler at the end of the QPM grating is related to the signal input by a transfer function which is related to the spatial Fourier transform of the grating [162]. The propagation equation for the generated idler envelope is given by [12]

$$\frac{dA_i}{dz} = -i\frac{\omega_i d(z)}{n_i c} A_s^* A_p e^{-i\Delta k' z}, \tag{A.1}$$

where subscripts (i, s, p) correspond to the idler, signal, and pump respectively. ω_j is the carrier frequency of wave j, and n_j is the refractive index evaluated at ω_j. The envelopes A_j are defined in relation to the electric field as $E = \frac{1}{2}\sum_j A_j \exp[i(\omega_j t - k_j z)] + \text{c.c.}$ where summation is performed over $j \in \{i,\, s,\, p\}$, and $k_j = \omega_j n_j / c$. The phase mismatch is defined as $\Delta k' = k_p - k_s - k_i$, and $d(z) = \pm d_0$ is the value of the relevant second-order nonlinear coefficient based on the $\chi^{(2)}$ tensor and the polarization directions of the interacting fields, and is inverted periodically or aperiodically in the QPM grating.

The idler field A_i can be written in a form normalized to its value at the output of an ideal (phasematched, with no RDC errors) periodic QPM grating (for which the domain size would be given by $l = \pi/\Delta k'$):

$$A_i = -i\frac{2}{\pi}\frac{\omega_i d_0}{n_i c} A_s^* A_p L a_i, \tag{A.2}$$

where a_i is the normalized idler field and L is the length of the QPM grating. With this definition, Eq. (A.1) can be written as

$$\frac{da_i}{dz} = \frac{\pi}{2L}\frac{d(z)}{d_0} e^{-i\Delta k' z} = g(z) e^{-i\Delta k' z}, \tag{A.3}$$

where the normalized grating profile $g(z)$ is defined implicitly in Eq. (A.3), with $g(z) = 0$ for $z < 0$ and $z > L$. By integrating Eq. (A.3), it can be seen that the normalized idler output $a_i(L)$ is simply the Fourier transform of $g(z)$, $\tilde{g}(k)$, evaluated at spatial frequency $k = \Delta k$. The square magnitude of $\tilde{g}$ gives the idler intensity relative to the "maximum" intensity achievable in a QPM grating of the same length, assuming that the pump and signal (or first harmonic in the case of SHG) are undepleted. By writing $g(z)$ as a sum of individual domains as in Eq. (4.4), $\tilde{g}(k)$ can be written as

$$\begin{aligned} \tilde{g}_{\mathbf{z}}(k) &= i\frac{\pi}{2kL}\sum_{n=1}^{N}(-1)^n\left(e^{-ik\mathbf{z}[n]} - e^{-ik\mathbf{z}[n-1]}\right) \\ &= i\frac{\pi}{kL}\left[\frac{e^{-ik\mathbf{z}[0]} + (-1)^N e^{-ik\mathbf{z}[N]}}{2} + \sum_{n=1}^{N-1}(-1)^n e^{-ik\mathbf{z}[n]}\right]. \end{aligned} \tag{A.4}$$

where $\mathbf{z}$ is a vector which specifies the domain boundary positions. The subscript $\mathbf{z}$ is included to indicate the domain boundary vector being considered. We will denote $\tilde{g}_{\mathbf{z}}(k)$ as the normalized transfer function.

Next, we approximate the edge terms in Eq. (A.4), i.e. those related to $\mathbf{z}[0]$

and $\mathbf{z}[N]$, in order to write $\tilde{g}_{\mathbf{z}}(k)$ in a simpler form as a summation of complex exponentials. We note that $\mathbf{z}[0]$ and $\mathbf{z}[N]$ are defined by the start- and end-points of the device and are therefore not random variables. The resulting (approximate) normalized transfer function is given by

$$\tilde{g}_{\mathbf{z}}(k) \approx \frac{i\pi}{kL} \sum_{n=1}^{N} (-1)^n e^{-ik\mathbf{z}[n]}. \tag{A.5}$$

In the presence of random perturbations to each $\mathbf{z}[n]$, this summation can be viewed as a random walk in the complex plane. The ideal vector of domain boundary positions (in the absence of any RDC errors) is denoted $\mathbf{z}_0$; for ideal periodic poling, $\mathbf{z}_0[n] = nl$ for domain boundary length l. For a phasematched interaction in such an ideal grating, $k = \Delta k = \pi/l$, in which case the summand is simply unity for each term, and so $\tilde{g}_{\mathbf{z}_0}(\pi/l) = 1$, consistent with the expected result.

Following Ref. [57], we assume independent and identically distributed (IID) errors in the domain lengths; we assume a normal distribution with variance σ_l^2 and mean 0. A schematic of RDC errors is illustrated in Fig. 4.2. In most cases, RDC errors are introduced during electric-field poling following lithographic fabrication of the QPM electrode pattern, such that their distribution is fixed for a given device. This assumption implies that in any particular device, a single vector $\mathbf{z}$ applies. However, in order to understand the effects of RDC errors it is useful to perform ensemble averaging of $\tilde{g}(k)$, treating $\mathbf{z}$ as a random vector.

The ensemble-averaged mean of the normalized transfer function is given by

$$\langle \tilde{g}_{\mathbf{z}}(k) \rangle = e^{-k^2\sigma_l^2/2} \tilde{g}_{\mathbf{z}_0}(k), \tag{A.6}$$

where the ensemble-averaging is performed over random vectors $\mathbf{z}$ and the relation

$$\left\langle e^{ikz} \right\rangle = e^{-k^2\sigma_l^2/2} e^{ik\langle z \rangle}, \tag{A.7}$$

which is a Gaussian-integral identity for scalar z, has been used. From Eq. (A.6), the expected value of the transfer function is reduced compared to that of the ideal transfer function. For example, the phasematched DFG conversion efficiency averaged over many different QPM gratings with RDC errors would be reduced by a factor $\exp(-k^2\sigma_l^2)$.

In addition to reducing the peak efficiency, RDC errors give rise to additional spatial frequency components far from nominal phasematching. To see this behavior we look at the ensemble-averaged value of $|\tilde{g}_{\mathbf{z}}(k)|^2$, which is given by

$$\begin{aligned}\left\langle|\tilde{g}_{\mathbf{z}}(k)|^2\right\rangle &= \left(\frac{\pi}{kL}\right)^2 \left\langle \sum_{m=1}^{N}\sum_{n=1}^{N}(-1)^{n-m}e^{-ik(\mathbf{z}[n]-\mathbf{z}[m])}\right\rangle \\ &= \left(\frac{\pi}{kL}\right)^2 \left[N\left(1-e^{-k^2\sigma_l^2}\right)+\right. \\ &\qquad \left. e^{-k^2\sigma_l^2}\sum_{n=1}^{N}\sum_{m=1}^{N}(-1)^{n-m}e^{-ik(\mathbf{z}_0[n]-\mathbf{z}_0[m])}\right], \end{aligned} \tag{A.8}$$

where the second relation can be found by separating the first relation into summation terms with $m=n$ and $m\neq n$: those with $m=n$ are independent of $\mathbf{z}[n]$ and hence do not acquire an $\exp[-(k\sigma_l)^2]$ factor. We can write Eq. (A.8) in a simpler form in terms of the ideal transfer function in the absence of RDC errors as

$$\left\langle|\tilde{g}_{\mathbf{z}}(k)|^2\right\rangle = e^{-k^2\sigma_l^2}|\tilde{g}_{\mathbf{z}_0}(k)|^2 + N\left(\frac{\pi}{kL}\right)^2\left(1-e^{-k^2\sigma_l^2}\right), \tag{A.9}$$

where the second term is a QPM noise pedestal originating from the RDC errors. The factor N associated with this noise floor is accurate provided that there are enough domains N that terms $O(1)$, which arise due to the neglected edge terms, can be neglected. For very thin crystals with small N, these edge terms would not be negligible.

For periodic QPM gratings with a 50% duty cycle, there is a particularly simple analytical form for the ideal transfer function when the edge terms are included. Assuming that $\mathbf{z}[n] = nl$ and defining $\Delta k = k - \pi/l$, it can be shown that

$$|\tilde{g}_{\mathbf{z}_0}(k)|^2 = \left[\frac{\pi}{2}\mathrm{sinc}\left(\frac{kl}{2}\right)\right]^2\left[\frac{\sin\left(N\Delta k_1 l/2\right)}{N\sin\left(\Delta k l/2\right)}\right]^2. \tag{A.10}$$

The first factor square brackets represents the reduced Fourier amplitudes in higher orders of the QPM grating relative to to the first order. The second factor is a "comb of sincs", which gives rise to tuning curves at each odd order of quasi-phasematching.

Eq. (A.9), when combined with the QPM tuning of an ideal device described by Eq. (A.10), gives a complete description of the effects of RDC errors for all orders of quasi-phasematching, and is useful for descriptions of highly nonlinear interactions involving multiple coupled nonlinear processes [156]. In this dissertation, we have primarily been concerned with the behavior of the device in the vicinity of first-order QPM. With these assumptions, Eq. (A.9) can be substantially simplified. Near first-order QPM,

$$|\tilde{g}_{\mathbf{z}_0}(k)|^2 \approx \operatorname{sinc}^2\left(\frac{\Delta k L}{2}\right) \tag{A.11}$$

and $k \approx \pi/l$. Therefore, we can rewrite Eq. (A.9) as

$$\left\langle |\tilde{g}_{\mathbf{z}}(\Delta k)|^2 \right\rangle = e^{-\pi^2\sigma_l^2/l^2} \operatorname{sinc}^2\left(\frac{\Delta k L}{2}\right) + \frac{1}{N}\left(1 - e^{-\pi^2\sigma_l^2/l^2}\right). \tag{A.12}$$

This equation, presented in the main text as Eq. (4.6) gives the value of the QPM pedestal far from the QPM peak, the main goal of this Appendix.

As was seen in the simulation results of Fig. 4.3, an individual grating exhibits large fluctuations in the generation efficiency far from phasematching, as might be expected for a random-walk-type process. Here, we calculate the variance of the efficiency pedestal. This quantity is obtained by evaluating both the second and fourth-order moments $\langle|\tilde{g}_{\mathbf{z}}(k)|^2\rangle$ and $\langle|\tilde{g}_{\mathbf{z}}(k)|^4\rangle$ using the same approach used to derive Eq. (A.8). Specifically, the fourth-order moment is given by

$$\left\langle |\tilde{g}_{\mathbf{z}}(k)|^4 \right\rangle = \left(\frac{\pi}{kL}\right)^4 \sum_{j=1}^{N-1}\sum_{k=1}^{N-1}\sum_{l=1}^{N-1}\sum_{m=1}^{N-1} (-1)^{j+k+l+m} \left\langle e^{-ik(\mathbf{z}[j]+\mathbf{z}[k]+\mathbf{z}[l]+\mathbf{z}[m])} \right\rangle. \tag{A.13}$$

Following lengthy algebraic simplification, the fourth-moment result is given by

$$\left\langle |\tilde{g}_{\mathbf{z}}(k)|^4 \right\rangle = \left(\frac{\pi}{kl}\right)^4 \left[\frac{2}{N^2}\left(1 - e^{-k^2\sigma_l^2}\right)^2 \right. \\ \left. + \frac{1}{N^3}\left(-1 - e^{-4k^2\sigma_z^2} + 3e^{-3k^2\sigma_l^2} - 6e^{-2k^2\sigma_l^2} + 5e^{-k^2\sigma_l^2}\right)\right]. \qquad \text{(A.14)}$$

When N is large, the $1/N^2$ term will dominate over the $1/N^3$ term. The variance σ_η^2 of the normalized transfer function is calculated as $\sigma_\eta^2 = \langle|\tilde{g}_{\mathbf{z}}(k)|^4\rangle - \langle|\tilde{g}_{\mathbf{z}}(k)|^2\rangle^2$. The standard deviation σ_η can then be approximated as

$$\sigma_\eta \approx N\left(\frac{\pi}{kL}\right)^2\left(1 - e^{-k^2\sigma_z^2}\right). \qquad \text{(A.15)}$$

This approximation applies for large N and values of k for which the ideal transfer function $|\tilde{g}_{\mathbf{z}_0}(k)|^2$ is negligible. This relation is the same as the mean $\langle|\tilde{g}|^2\rangle$, as would be expected for a random walk process for the generated idler field. The magnitude of the spatial Fourier spectrum of a particular grating with RDC errors is thus with high probability within a few times the ensemble-averaged mean.

Appendix B

Effects of Čerenkov modes on parametric interactions in waveguides with random duty-cycle errors

We consider parametric fluorescence in waveguides with QPM random duty-cycle errors including effects of radiation modes. In planar waveguides, parametric amplification involving an idler mode which is radiated into the substrate can have substantially larger bandwidth than an interaction involving only bound modes [163]. Modeling of large-bandwidth parametric interactions in this Čerenkov-idler configuration has been published in work by Rastogi and coworkers [164]. For simplicity, in this treatment we consider planar waveguides as in previous modeling. This assumption is adequate to describe wave-mixing processes in RPE waveguides, which typically have widths suitable for lateral confinement but modes which may leak into the substrate. The analysis is in any case straightforwardly generalized to channel waveguides, as given in Eq. (B.14). The growth of a particular idler radiation mode with wavevector β_i by the Čerenkov process is given as

$$\frac{\mathrm{d}a_i(\beta_i, z)}{\mathrm{d}z} = \gamma(\beta_i)a_p(z)a_s(z)e^{-i\Delta\beta(\beta_i)z} \tag{B.1}$$

where the coupling coefficient $\gamma(\beta_i)$ and nonlinear polarization $\mathcal{P}_i$ are defined as

$$\gamma(\beta_i) = \frac{\epsilon_0 d_{\text{eff}}}{2} \int_{-\infty}^{\infty} u_p(x) u_s^*(x) u_i^*(x)\ \mathrm{d}x \tag{B.2a}$$

$$= \int_{-\infty}^{\infty} \mathcal{P}_i u_i^*(x)\ \mathrm{d}x \tag{B.2b}$$

where we see that the coupling coefficient $\gamma(\beta_i)$ can be viewed as the projection of the nonlinear polarization onto the idler radiation mode with propagation constant β_i. The nonlinear polarization $\mathcal{P}_i(x)$ has been defined implicitly in Eq. (B.2b).

In the low-gain regime corresponding to parametric fluorescence, we can integrate Eq. (B.1) straightforwardly over the length L of the crystal since the signal and pump fields are unchanged from their initial values:

$$a_i(\beta_i, L) = \gamma(\beta_i) a_p(0) a_s(0) \frac{e^{-i\Delta\beta(\beta_i)L} - 1}{-i\Delta\beta(\beta_i)}. \tag{B.3}$$

The photon flux summed across the idler modes is then given by

$$N_i(L) = \int_{\beta_{\min}}^{\beta_{\max}} |a_i(\beta_i, L)|^2\ \mathrm{d}\beta_i \tag{B.4}$$

where $\beta_{\min}$ and $\beta_{\max}$ are the minimum an maximum values of the range of radiation mode propagation constants. Expanding Eq. (B.4) gives

$$N_i(L) = |a_p(0) a_s(0)|^2 \frac{L^2}{4} \int_{\beta_{\min}}^{\beta_{\max}} \left| \gamma(\beta_i) \operatorname{sinc}\left(\frac{\Delta\beta_i(\beta_i) L}{2} \right) \right|^2 \mathrm{d}\beta_i\,. \tag{B.5}$$

We are interested in evaluating the integral in Eq. (B.5) in two different regimes, corresponding to the case in which a phasematching feature for a Čerenkov idler mode exists, or whether such a phasematching feature does not exist, but there is rather a weak phasematching pedestal independent of β_i. It is the latter case that most concerns us here, but the calculation of the former is illustrative.

We first consider the case in which a phasematched point exists in the range of propagation constants between $\beta_{\min}$ and $\beta_{\max}$. Assuming that the crystal is long enough that the coupling coefficient $\gamma(\beta_i)$ varies slowly over the width of the phase-matching feature at $\beta_i = \beta_{\rm pm}$, we can pull it out of the integral over β_i in Eq. (B.5), and are left with

$$N_i(L) = \frac{\hbar c}{\lambda_i} \left|a_p(0) a_s(0)\right|^2 \frac{\pi L}{2} \left|\gamma(\beta_{\rm pm})\right|^2 \tag{B.6}$$

where we have made use of the definite integral

$$\int_{-\infty}^{\infty} \mathrm{sinc}^2 x \; \mathrm{d}x = \pi. \tag{B.7}$$

As the total number of photons generated into the all the idler modes is equal to that added to the signal mode, we can write the signal gain as

$$G_s = 1 + \frac{N_i(L)}{|a_s(0)|^2} \tag{B.8a}$$

$$= 1 + \frac{\pi L}{2} |a_p(0)|^2 |\gamma(\beta_{\rm pm})|^2 \tag{B.8b}$$

Here, as in most treatments of Čerenkov-idler parametric amplification [164], the gain is dominated by only the idler radiation mode that is phasematched.

We now consider the opposite limit, in which there are no phasematching features over the range of idler propagation constants $\beta_{\min}$ to $\beta_{\max}$. In this limit, Eq. (B.5) becomes

$$N_i(L) = \left|a_p(0) a_s(0)\right|^2 \tilde{g}_\infty^2 \frac{L^2}{4} \int_{\beta_{\min}}^{\beta_{\max}} \left|\gamma(\beta_i)\right|^2 \, \mathrm{d}\beta_i, \tag{B.9}$$

where we have inserted the QPM pedestal height $\tilde{g}_\infty^2$ of Eq. (4.9). We can evaluate the integral of Eq. (B.9) by inserting the definition of the coupling constant from

Eq. (B.1). Expanding, we have

$$\int |\gamma(\beta_i)|^2 \, \mathrm{d}\beta_i = \int \mathrm{d}\beta_i \left| \int_{-\infty}^{\infty} \mathcal{P}_i(x) u_i^*(x) \, \mathrm{d}x \right|^2 , \tag{B.10a}$$

$$= \int \mathrm{d}\beta_i \int_{-\infty}^{\infty} \mathcal{P}_i(x) u_i^*(\beta_i, x) \, \mathrm{d}x \int_{-\infty}^{\infty} \mathcal{P}_i^*(x') u_i(\beta_i, x') \, \mathrm{d}x', \tag{B.10b}$$

$$= \int \mathrm{d}\beta_i \int_{-\infty}^{\infty} \mathrm{d}x \int_{-\infty}^{\infty} \mathrm{d}x' \; \mathcal{P}_i(x) \mathcal{P}_i^*(x) u_i^*(\beta_i, x) u_i(\beta_i, x), \tag{B.10c}$$

$$= \int_{-\infty}^{\infty} \mathrm{d}x \; \mathcal{P}_i(x) \int_{-\infty}^{\infty} \mathrm{d}x' \, \mathcal{P}_i^*(x') \int \mathrm{d}\beta_i \, u_i^*(\beta_i, x) u_i(\beta_i, x'). \tag{B.10d}$$

To evaluate the integral over β_i in Eq. (B.10d) we can use the completeness relation for the waveguide eigenfunction expansion:

$$\delta(x - x') = \sum_n u_{i,n}(x) u_{i,n}^*(x') + \int u_i(\beta_i, x) u_i^*(\beta_i, x') \, \mathrm{d}\beta_i, \tag{B.11}$$

where the sum is over the bound modes of the waveguide and the integral is over the radiation modes. Applying Eq. (B.11), we have:

$$\int |\gamma(\beta_i)|^2 \, \mathrm{d}\beta_i = \int_{-\infty}^{\infty} \mathrm{d}x \; \mathcal{P}_i(x) \int_{-\infty}^{\infty} \mathrm{d}x' \, \mathcal{P}_i^*(x') \left[\delta(x - x') - \sum_n u_{i,n}(x) u_{i,n}^*(x') \right] \tag{B.12a}$$

$$= \int_{-\infty}^{\infty} \mathrm{d}x \, |\mathcal{P}_i(x)|^2 - \sum_n \int_{-\infty}^{\infty} \mathrm{d}x \; \mathcal{P}_i(x) u_{i,n}(x) \int \mathrm{d}x' \; P_i^*(x') u_{i,n}^*(x') \tag{B.12b}$$

$$= \left(\frac{\epsilon_0 d_{\mathrm{eff}}}{2} \right)^2 \left[\int_{-\infty}^{\infty} \mathrm{d}x \, |u_s(x) u_p(x)|^2 - \sum_n \left| \int_{-\infty}^{\infty} \mathrm{d}x \, u_s^*(x) u_p(x) u_{i,n}^*(x) \right|^2 \right] \tag{B.12c}$$

$$= \left(\frac{\epsilon_0 d_{\mathrm{eff}}}{2} \right)^2 \int_{-\infty}^{\infty} \mathrm{d}x \; |u_s(x) u_p(x)|^2 \tag{B.12d}$$

where the sum extends over the bound modes of the idler wave. Eq. (B.12c) follows from Eq. (B.12b) via replacing $\mathcal{P}_i(x)$ with its definition in Eq. (B.2b). The simplification in Eq. (B.12d) is valid when no bound modes at the idler wavelength exist, so the sum can be dropped.

Therefore, in the limit when any phasematching feature can be neglected, we calculate the gain (and correspondingly the signal-photon generation rate) via inserting Eq. (B.12d) into Eq. (B.9):

$$N_i(L) = |a_p(0)a_s(0)|^2\, \tilde{g}_\infty^2 \frac{L^2\epsilon_0^2 d_{\text{eff}}^2}{16} \int_{-\infty}^{\infty} \mathrm{d}x\, |u_p(x)u_s(x)|^2\,. \tag{B.13}$$

Eq. (B.13) represents all photons created into all the idler modes, and has now been expressed without reference to the modal field distributions of the radiating idler modes, making it much simpler to calculate. The integrand, when generalized to a 2D structure, is the Čerenkov-idler mode-overlap integral:

$$\Theta_{\text{Cer}}^2 = \frac{1}{A_I} = \iint_{-\infty}^{\infty} |u_s(x,y)u_p(x,y)|^2\, \mathrm{d}x\, \mathrm{d}y, \tag{B.14}$$

where we define A_I as the interaction area. This expression is used to calculate the expected SPDC rate and the factor r for the discussion of random duty-cycle error tolerances from Sec. 4.1.

Bibliography

[1] T. D. Ladd, F. Jelezko, R. Laflamme, Y. Nakamura, C. Monroe, and J. L. O'Brien. Quantum computers. *Nature*, 464(7285):45–53, March 2010.

[2] H. J. Kimble. The quantum internet. *Nature*, 453(7198):1023–1030, June 2008.

[3] Stephan Ritter, Christian Nölleke, Carolin Hahn, Andreas Reiserer, Andreas Neuzner, Manuel Uphoff, Martin Mücke, Eden Figueroa, Joerg Bochmann, and Gerhard Rempe. An elementary quantum network of single atoms in optical cavities. *Nature*, 484(7393):195–200, April 2012.

[4] E. Togan, Y. Chu, A. S. Trifonov, L. Jiang, J. Maze, L. Childress, M. V. G. Dutt, A. S. Sorensen, P. R. Hemmer, A. S. Zibrov, and M. D. Lukin. Quantum entanglement between an optical photon and a solid-state spin qubit. *Nature*, 466(7307):730–734, 2010.

[5] David Press, Thaddeus D. Ladd, Bingyang Zhang, and Yoshihisa Yamamoto. Complete quantum control of a single quantum dot spin using ultrafast optical pulses. *Nature*, 456(7219):218–221, November 2008.

[6] Prem Kumar. Quantum frequency conversion. *Optics Letters*, 15(24):1476–1478, December 1990.

[7] Jianming Huang and Prem Kumar. Observation of quantum frequency conversion. *Physical Review Letters*, 68(14):2153, April 1992.

[8] P. A. Franken, A. E. Hill, C. W. Peters, and G. Weinreich. Generation of optical harmonics. *Physical Review Letters*, 7(4):118–119, 1961.

[9] C. Langrock, S. Kumar, J.E. McGeehan, A.E. Willner, and M.M. Fejer. All-optical signal processing using $\chi^{(2)}$ nonlinearities in guided-wave devices. *Lightwave Technology, Journal of*, 24(7):2579 – 2592, July 2006.

[10] J. E. Midwinter and J. Warner. Up-conversion of near infrared to visible radiation in lithium-meta-niobate. *Journal of Applied Physics*, 38(2):519–523, February 1967.

[11] J. A. Armstrong, N. Bloembergen, J. Ducuing, and P. S. Pershan. Interactions between light waves in a nonlinear dielectric. *Physical Review*, 127(6):1918–1939, 1962.

[12] Robert W. Boyd. *Nonlinear Optics, Third Edition*. Academic Press, April 2008.

[13] John David Jackson. *Classical Electrodynamics, Third Edition*. Wiley, August 1998.

[14] Dietrich Marcuse. *Theory of Dielectric Optical Waveguides, Second Edition*. Academic Press, April 1991.

[15] Peter D. Drummond. Electromagnetic quantization in dispersive inhomogeneous nonlinear dielectrics. *Physical Review A*, 42(11):6845–6857, December 1990.

[16] Roy J. Glauber and M. Lewenstein. Quantum optics of dielectric media. *Physical Review A*, 43(1):467–491, January 1991.

[17] Rodney Loudon. *The Quantum Theory of Light*. Oxford University Press, USA, 3rd edition, November 2000.

[18] Leonard Mandel and Emil Wolf. *Optical Coherence and Quantum Optics*. Cambridge University Press, 1st edition, September 1995.

[19] M.G. Raymer, S.J. van Enk, C.J. McKinstrie, and H.J. McGuinness. Interference of two photons of different color. *Optics Communications*, 283(5):747–752, March 2010.

[20] Paul G. Kwiat, Klaus Mattle, Harald Weinfurter, Anton Zeilinger, Alexander V. Sergienko, and Yanhua Shih. New high-intensity source of polarization-entangled photon pairs. *Physical Review Letters*, 75(24):4337–4341, December 1995.

[21] Nicolas Gisin, Grgoire Ribordy, Wolfgang Tittel, and Hugo Zbinden. Quantum cryptography. *Reviews of Modern Physics*, 74(1):145–195, March 2002.

[22] Robert H. Hadfield. Single-photon detectors for optical quantum information applications. *Nat Photon*, 3(12):696–705, December 2009.

[23] Aaron P. Vandevender and Paul G. Kwiat. High efficiency single photon detection via frequency up-conversion. *Journal of Modern Optics*, 51(9):1433, 2004.

[24] J. E. Midwinter. Image conversion from 1.6 μm to the visible in lithium niobate. *Applied Physics Letters*, 12(3):68–70, February 1968.

[25] Roy J. Glauber. The quantum theory of optical coherence. *Physical Review*, 130(6):2529–2539, June 1963.

[26] R. W. Boyd and C. H. Townes. An infrared upconverter for astronomical imaging. *Applied Physics Letters*, 31(7):440–442, October 1977.

[27] Michael Vasilyev and Prem Kumar. Frequency up-conversion of quantum images. *Optics Express*, 20(6):6644–6656, March 2012.

[28] Rostislav V. Roussev, Carsten Langrock, Jonathan R. Kurz, and M. M. Fejer. Periodically poled lithium niobate waveguide sum-frequency generator for efficient single-photon detection at communication wavelengths. *Optics Letters*, 29(13):1518–1520, July 2004.

[29] Marius A. Albota and FrancoN. C. Wong. Efficient single-photon counting at 1.55 μm by means of frequency upconversion. *Optics Letters*, 29(13):1449–1451, July 2004.

[30] Carsten Langrock, Eleni Diamanti, Rostislav V. Roussev, Yoshihisa Yamamoto, M. M. Fejer, and Hiroki Takesue. Highly efficient single-photon detection at communication wavelengths by use of upconversion in reverse-proton-exchanged periodically poled $LiNbO_3$ waveguides. *Optics Letters*, 30(13):1725–1727, July 2005.

[31] Huafang Dong, Haifeng Pan, Yao Li, E Wu, and Heping Zeng. Efficient single-photon frequency upconversion at 1.06 μm with ultralow background counts. *Applied Physics Letters*, 93(7):071101–3, 2008.

[32] H. Kamada, M. Asobe, T. Honjo, H. Takesue, Y. Tokura, Y. Nishida, O. Tadanaga, and H. Miyazawa. Efficient and low-noise single-photon detection in 1550 nm communication band by frequency upconversion in periodically poled $LiNbO_3$ waveguides. *Optics Letters*, 33(7):639–641, April 2008.

[33] R T Thew, S Tanzilli, L Krainer, S C Zeller, A Rochas, I Rech, S Cova, H Zbinden, and N Gisin. Low jitter up-conversion detectors for telecom wavelength GHz QKD. *New Journal of Physics*, 8(3):32–32, March 2006.

[34] Eleni Diamanti, Hiroki Takesue, Carsten Langrock, M. M. Fejer, and Yoshihisa Yamamoto. 100 km differential phase shift quantum key distribution experiment with low jitter up-conversion detectors. *Optics Express*, 14(26):13073–13082, December 2006.

[35] S. Tanzilli, W. Tittel, M. Halder, O. Alibart, P. Baldi, N. Gisin, and H. Zbinden. A photonic quantum information interface. *Nature*, 437(7055):116–120, 2005.

[36] S. Ramelow, A. Fedrizzi, A. Poppe, N. K. Langford, and A. Zeilinger. Polarization-entanglement-conserving frequency conversion of photons. *Physical Review A*, 85(1):013845, January 2012.

[37] Qiang Zhang, Carsten Langrock, M. M. Fejer, and Yoshihisa Yamamoto. Waveguide-based single-pixel up-conversion infrared spectrometer. *Optics Express*, 16(24):19557–19561, November 2008.

[38] Eleni Diamanti, Carsten Langrock, M. M. Fejer, Yoshihisa Yamamoto, and Hiroki Takesue. 1.5 μm photon-counting optical time-domain reflectometry with a single-photon detector based on upconversion in a periodically poled lithium niobate waveguide. *Optics Letters*, 31(6):727–729, March 2006.

[39] Matthew T. Rakher, Lijun Ma, Oliver Slattery, Xiao Tang, and Kartik Srinivasan. Quantum transduction of telecommunications-band single photons from a quantum dot by frequency upconversion. *Nature Photonics*, 4(11):786–791, November 2010.

[40] Matthew T. Rakher, Lijun Ma, Marcelo Davano, Oliver Slattery, Xiao Tang, and Kartik Srinivasan. Simultaneous wavelength translation and amplitude modulation of single photons from a quantum dot. *Physical Review Letters*, 107(8):083602, 2011.

[41] Aaron P. VanDevender and Paul G. Kwiat. Quantum transduction via frequency upconversion (Invited). *Journal of the Optical Society of America B*, 24(2):295–299, February 2007.

[42] Lijun Ma, Matthew T. Rakher, Martin J. Stevens, Oliver Slattery, Kartik Srinivasan, and Xiao Tang. Temporal correlation of photons following frequency up-conversion. *Optics Express*, 19(11):10501–10510, May 2011.

[43] W. H. Louisell, A. Yariv, and A. E. Siegman. Quantum fluctuations and noise in parametric processes. I. *Physical Review*, 124(6):1646–1654, December 1961.

[44] Z. Y. Ou. Efficient conversion between photons and between photon and atom by stimulated emission. *Physical Review A*, 78(2):023819, 2008.

[45] Yu Ding and Z. Y. Ou. Frequency downconversion for a quantum network. *Optics Letters*, 35(15):2591–2593, 2010.

[46] Noë Curtz, Rob Thew, Christoph Simon, Nicolas Gisin, and Hugo Zbinden. Coherent frequency-down-conversion interface for quantum repeaters. *Optics Express*, 18(21):22099–22104, October 2010.

[47] Hiroki Takesue. Single-photon frequency down-conversion experiment. *Physical Review A*, 82(1):013833, July 2010.

[48] J. S. Pelc, C. Langrock, Q. Zhang, and M. M. Fejer. Influence of domain disorder on parametric noise in quasi-phase-matched quantum frequency converters. *Optics Letters*, 35(16):2804–2806, 2010.

[49] Sebastian Zaske, Andreas Lenhard, and Christoph Becher. Efficient frequency downconversion at the single photon level from the red spectral range to the telecommunications C-band. *Optics Express*, 19(13):12825–12836, June 2011.

[50] Rikizo Ikuta, Yoshiaki Kusaka, Tsuyoshi Kitano, Hiroshi Kato, Takashi Yamamoto, Masato Koashi, and Nobuyuki Imoto. Wide-band quantum interface for visible-to-telecommunication wavelength conversion. *Nature Communications*, 2:537, November 2011.

[51] Zhen-Sheng Yuan, Yu-Ao Chen, Bo Zhao, Shuai Chen, Joerg Schmiedmayer, and Jian-Wei Pan. Experimental demonstration of a BDCZ quantum repeater node. *Nature*, 454(7208):1098–1101, August 2008.

[52] C. McKinstrie, J. Harvey, S. Radic, and M. Raymer. Translation of quantum states by four-wave mixing in fibers. *Optics Express*, 13(22):9131–9142, October 2005.

[53] A. H. Gnauck, R. M. Jopson, C. J. McKinstrie, J. C. Centanni, and S. Radic. Demonstration of low-noise frequency conversion by bragg scattering in a fiber. *Optics Express*, 14(20):8989–8994, October 2006.

[54] H. J. McGuinness, M. G. Raymer, C. J. McKinstrie, and S. Radic. Quantum frequency translation of single-photon states in a photonic crystal fiber. *Physical Review Letters*, 105(9):093604, 2010.

[55] Krishnan R. Parameswaran. *Highly Efficient Optical Frequency Mixers*. PhD thesis, Stanford University, May 2002.

[56] Rostislav V. Roussev. *Optical-Frequency Mixers in Periodically Poled Lithium Niobate: Materials, Modeling and Characterization*. PhD thesis, Stanford, December 2006.

[57] M.M. Fejer, G.A. Magel, D.H. Jundt, and R.L. Byer. Quasi-phase-matched second harmonic generation: tuning and tolerances. *Quantum Electronics, IEEE Journal of*, 28(11):2631–2654, 1992.

[58] K. Rustagi, S. Mehendale, and S. Meenakshi. Optical frequency conversion in quasi-phase-matched stacks of nonlinear crystals. *IEEE Journal of Quantum Electronics*, 18(6):1029– 1041, June 1982.

[59] L. A Eyres, P. J Tourreau, T. J Pinguet, C. B Ebert, J. S Harris, M. M Fejer, L. Becouarn, B. Gerard, and E. Lallier. All-epitaxial fabrication of thick, orientation-patterned GaAs films for nonlinear optical frequency conversion. *Applied Physics Letters*, 79(7):904–906, August 2001.

[60] S. Matsumoto, E.J. Lim, H.M. Hertz, and M.M. Fejer. Quasiphase-matched second harmonic generation of blue light in electrically periodically-poled lithium tantalate waveguides. *Electronics Letters*, 27(22):2040, 1991.

[61] G. D. Miller, R. G. Batchko, W. M. Tulloch, D. R. Weise, M. M. Fejer, and R. L. Byer. 42%-efficient single-pass cw second-harmonic generation in periodically poled lithium niobate. *Optics Letters*, 22(24):1834–1836, December 1997.

[62] Miller, Gregory David. *Periodically poled lithium niobate: modeling, fabrication, and nonlinear-optical performance*. PhD thesis, Stanford University, July 1998.

[63] L. E. Myers, R. C. Eckardt, M. M. Fejer, R. L. Byer, W. R. Bosenberg, and J. W. Pierce. Quasi-phase-matched optical parametric oscillators in bulk periodically poled $LiNbO_3$. *Journal of the Optical Society of America B*, 12(11):2102–2116, November 1995.

[64] Koichiro Nakamura, Jonathan Kurz, Krishnan Parameswaran, and M. M Fejer. Periodic poling of magnesium-oxide-doped lithium niobate. *Journal of Applied Physics*, 91(7):4528–4534, April 2002.

[65] J. S. Pelc, Q. Zhang, C. R. Phillips, L. Yu, Y. Yamamoto, and M. M. Fejer. Cascaded frequency upconversion for high-speed single-photon detection at 1550 nm. *Optics Letters*, 37(4):476–478, February 2012.

[66] G. D. Boyd. Parametric interaction of focused gaussian light beams. *Journal of Applied Physics*, 39(8):3597, 1968.

[67] J. S. Pelc, L. Ma, C. R. Phillips, Q. Zhang, C. Langrock, O. Slattery, X. Tang, and M. M. Fejer. Long-wavelength-pumped upconversion single-photon detector at 1550 nm: performance and noise analysis. *Optics Express*, 19(22):21445–21456, October 2011.

[68] J. Webjorn, F. Laurell, and G. Arvidsson. Fabrication of periodically domain-inverted channel waveguides in lithium niobate for second harmonic generation. *Journal of Lightwave Technology*, 7(10):1597–1600, October 1989.

[69] Y. Nishida, H. Miyazawa, M. Asobe, O. Tadanaga, and H. Suzuki. Direct-bonded QPM-LN ridge waveguide with high damage resistance at room temperature. *Electronics Letters*, 39(7):609 – 611, April 2003.

[70] M.H. Chou, I. Brener, M.M. Fejer, E.E. Chaban, and S.B. Christman. 1.5-μm-band wavelength conversion based on cascaded second-order nonlinearity in $LiNbO_3$ waveguides. *Photonics Technology Letters, IEEE*, 11(6):653 –655, June 1999.

[71] Yu. N. Korkishko, V. A. Fedorov, T. M. Morozova, F. Caccavale, F. Gonella, and F. Segato. Reverse proton exchange for buried waveguides in $LiNbO_3$. *Journal of the Optical Society of America A*, 15(7):1838–1842, July 1998.

[72] M. L Bortz, S. J Field, M. M Fejer, D. W Nam, R. G Waarts, and D. F Welch. Noncritical quasi-phase-matched second harmonic generation in an annealed proton-exchanged $LiNbO_3$ waveguide. *IEEE Journal of Quantum Electronics*, 30(12):2953–2960, December 1994.

[73] R. Regener and W. Sohler. Loss in low-finesse Ti:LiNbO$_3$ optical waveguide resonators. *Applied Physics B Photophysics and Laser Chemistry*, 36:143–147, March 1985.

[74] Philip Bevington and D. Keith Robinson. *Data Reduction and Error Analysis for the Physical Sciences*. McGraw-Hill Science/Engineering/Math, 3rd edition, July 2002.

[75] J. S. Pelc, C. R. Phillips, D. Chang, C. Langrock, and M. M. Fejer. Efficiency pedestal in quasi-phase-matching devices with random duty-cycle errors. *Optics Letters*, 36(6):864–866, March 2011.

[76] Sten Helmfrid and Gunnar Arvidsson. Influence of randomly varying domain lengths and nonuniform effective index on second-harmonic generation in quasi-phase-matching waveguides. *Journal of the Optical Society of America B*, 8(4):797–804, April 1991.

[77] M. Baudrier-Raybaut, R. Haidar, Ph. Kupecek, Ph. Lemasson, and E. Rosencher. Random quasi-phase-matching in bulk polycrystalline isotropic nonlinear materials. *Nature*, 432(7015):374–376, November 2004.

[78] G. Binnig, C. F. Quate, and Ch. Gerber. Atomic force microscope. *Physical Review Letters*, 56(9):930–933, March 1986.

[79] G. D. Miller, R. G. Batchko, M. M. Fejer, and R. L. Byer. Visible quasi-phasematched harmonic generation by electric-field-poled lithium niobate. *SPIE Proceedings on Nonlinear Frequency Generation and Conversion*, 2700, 1996.

[80] Daniel J. Gauthier, Robert W. Boyd, Robert K. Jungquist, Jerold B. Lisson, and Laurie Lyon Voci. Phase-conjugate fizeau interferometer. *Optics Letters*, 14(6):323–325, March 1989.

[81] S. E. Harris, M. K. Oshman, and R. L. Byer. Observation of tunable optical parametric fluorescence. *Physical Review Letters*, 18(18):732, May 1967.

[82] Thomas J. Kane and Robert L. Byer. Monolithic, unidirectional single-mode Nd:YAG ring laser. *Optics Letters*, 10(2):65–67, February 1985.

[83] Marco Fiorentino, Sean M. Spillane, Raymond G. Beausoleil, Tony D. Roberts, Philip Battle, and Mark W. Munro. Spontaneous parametric down-conversion in periodically poled KTP waveguides and bulk crystals. *Optics Express*, 15(12):7479–7488, June 2007.

[84] Byer, Robert L. Optical parametric oscillators. In Rabin, H. and Tang, C. L., editors, *Quantum Electronics, a Treatise*, volume 1. Academic Press, 1975.

[85] C. V. Raman and K. S. Krishnan. A new type of secondary radiation. *Nature*, 121(3048):501–502, March 1928.

[86] R. Loudon. The raman effect in crystals. *Advances in Physics*, 50(7):813–864, 2001.

[87] R. F. Schaufele and M. J. Weber. Raman scattering by lithium niobate. *Physical Review*, 152(2):705–708, December 1966.

[88] R. S. Weis and T. K. Gaylord. Lithium niobate: Summary of physical properties and crystal structure. *Applied Physics A: Materials Science & Processing*, 37(4):191–203, 1985.

[89] Gustavo R PazPujalt, David D Tuschel, Gabriel Braunstein, Thomas Blanton, S. Tong Lee, and Lillie M Salter. Characterization of proton exchange lithium niobate waveguides. *Journal of Applied Physics*, 76(7):3981–3987, October 1994.

[90] C. R. Phillips, Carsten Langrock, J. S. Pelc, M. M. Fejer, J. Jiang, Martin E. Fermann, and I. Hartl. Supercontinuum generation in quasi-phase-matched $LiNbO_3$ waveguide pumped by a Tm-doped fiber laser system. *Optics Letters*, 36(19):3912–3914, October 2011.

[91] C. R. Phillips, Carsten Langrock, J. S. Pelc, M. M. Fejer, I. Hartl, and Martin E. Fermann. Supercontinuum generation in quasi-phasematched waveguides. *Optics Express*, 19(20):18754–18773, 2011.

[92] Tatyana Volk and Manfred Whlecke. *Lithium Niobate Defects, Photorefraction and Ferroelectric Switching*. Springer Series in Materials Science. 2009.

[93] A Ridah, P Bourson, M D Fontana, and G Malovichko. The composition dependence of the raman spectrum and new assignment of the phonons in $LiNbO_3$. *Journal of Physics: Condensed Matter*, 9(44):9687–9693, November 1997.

[94] P. Chufyrev, N. Sidorov, M. Palatnikov, and A. Yanichev. Manifestation of the specific structural features of lithium niobate single crystals of different composition in their raman spectra. *Optics and Spectroscopy*, 105(6):913–918, 2008.

[95] M. G. Raymer and J. Mostowski. Stimulated Raman scattering: unified treatment of spontaneous initiation and spatial propagation. *Physical Review A*, 24(4):1980, October 1981.

[96] N. Surovtsev, V. Malinovskii, A. Pugachev, and A. Shebanin. The nature of low-frequency raman scattering in congruent melting crystals of lithium niobate. *Physics of the Solid State*, 45(3):534–541, 2003.

[97] C. R. Phillips, J. S. Pelc, and M. M. Fejer. Continuous wave monolithic quasi-phase-matched optical parametric oscillator in periodically poled lithium niobate. *Optics Letters*, 36(15):2973–2975, 2011.

[98] E. Knill, R. Laflamme, and G. J. Milburn. A scheme for efficient quantum computation with linear optics. *Nature*, 409(6816):46–52, January 2001.

[99] G. N. Goltsman, O. Okunev, G. Chulkova, A. Lipatov, A. Semenov, K. Smirnov, B. Voronov, A. Dzardanov, C. Williams, and Roman Sobolewski. Picosecond superconducting single-photon optical detector. *Applied Physics Letters*, 79(6):705, 2001.

[100] B. Cabrera, R. M. Clarke, P. Colling, A. J. Miller, S. Nam, and R. W. Romani. Detection of single infrared, optical, and ultraviolet photons using superconducting transition edge sensors. *Applied Physics Letters*, 73(6):735, 1998.

[101] Robert G. W. Brown, Kevin D. Ridley, and John G. Rarity. Characterization of silicon avalanche photodiodes for photon correlation measurements. 1: Passive quenching. *Applied Optics*, 25(22):4122–4126, November 1986.

[102] Robert G. W. Brown, Robin Jones, John G. Rarity, and Kevin D. Ridley. Characterization of silicon avalanche photodiodes for photon correlation measurements. 2: Active quenching. *Applied Optics*, 26(12):2383–2389, June 1987.

[103] S. Cova, A. Longoni, and A. Andreoni. Towards picosecond resolution with singlephoton avalanche diodes. *Review of Scientific Instruments*, 52(3):408–412, March 1981.

[104] A. R. Dixon, Z. L. Yuan, J. F. Dynes, A. W. Sharpe, and A. J. Shields. Gigahertz decoy quantum key distribution with 1 mbit/s secure key rate. *Optics Express*, 16(23):18790–18979, November 2008.

[105] R.E. Warburton, M.A. Itzler, and G.S. Buller. Improved free-running InGaAs/InP single-photon avalanche diode detectors operating at room temperature. *Electronics Letters*, 45(19):996 –997, 2009.

[106] Mark A. Itzler, Xudong Jiang, Mark Entwistle, Krystyna Slomkowski, Alberto Tosi, Fabio Acerbi, Franco Zappa, and Sergio Cova. Advances in InGaAsP-based avalanche diode single photon detectors. *Journal of Modern Optics*, 58(3/4):174–200, February 2011.

[107] Naoto Namekata, Shunsuke Adachi, and Shuichiro Inoue. 1.5 GHz single-photon detection at telecommunication wavelengths using sinusoidally gated InGaAs/InP avalanche photodiode. *Optics Express*, 17(8):6275–6282, April 2009.

[108] W. J. Kozlovsky, C. D. Nabors, R. C. Eckardt, and R. L. Byer. Monolithic MgO:LiNbO$_3$ doubly resonant optical parametric oscillator pumped by a frequency-doubled diode-laser-pumped Nd:YAG laser. *Optics Letters*, 14(1):66–68, January 1989.

[109] Dieter H. Jundt. Temperature-dependent sellmeier equation for the index of refraction, n_e, in congruent lithium niobate. *Optics Letters*, 22(20):1553–1555, October 1997.

[110] J. S Pelc, G. -L Shentu, Q. Zhang, M. M Fejer, and J. -W Pan. Upconversion of optical signals with multi-longitudinal-mode pump lasers. *arXiv:1204.6383*, April 2012.

[111] C. R. Phillips and M. M. Fejer. Stability of the singly resonant optical parametric oscillator. *Journal of the Optical Society of America B*, 27(12):2687–2699, December 2010.

[112] Mikhail Meleshkevich, Anton Drozhzhin, Nikolai Platonov, Denis Gapontsev, and Dmitry Starodubov. 10 W single-mode single frequency Tm-doped fiber amplifiers optimized for 1800-2020-nm band. In L. N. Durvasula, Andrew J. W. Brown, and Johan Nilsson, editors, *Fiber Lasers II: Technology, Systems, and Applications*, volume 5709, pages 117–124, San Jose, CA, USA, April 2005. SPIE.

[113] Shibin Jiang. Private communication.

[114] Hiroki Takesue, Eleni Diamanti, Carsten Langrock, M. M. Fejer, and Yoshihisa Yamamoto. 1.5-μm single photon counting using polarization-independent upconversion detector. *Optics Express*, 14(26):13067–13072, December 2006.

[115] Kai-Mei C. Fu, Thaddeus D. Ladd, Charles Santori, and Yoshihisa Yamamoto. Optical detection of the spin state of a single nucleus in silicon. *Physical Review B*, 69(12):125306, March 2004.

[116] Carl A. Kocher and Eugene D. Commins. Polarization correlation of photons emitted in an atomic cascade. *Physical Review Letters*, 18(15):575–577, April 1967.

[117] David C. Burnham and Donald L. Weinberg. Observation of simultaneity in parametric production of optical photon pairs. *Physical Review Letters*, 25(2):84–87, July 1970.

[118] Christian Brunel, Brahim Lounis, Philippe Tamarat, and Michel Orrit. Triggered source of single photons based on controlled single molecule fluorescence. *Physical Review Letters*, 83(14):2722–2725, October 1999.

[119] B A Joyce. Molecular beam epitaxy. *Reports on Progress in Physics*, 48(12):1637–1697, December 1985.

[120] Charles Santori, David Fattal, and Yoshihisa Yamamoto. *Single-photon Devices and Applications*. Wiley-VCH, 1st edition, October 2010.

[121] Kristiaan De Greve, Peter L. McMahon, David Press, Thaddeus D. Ladd, Dirk Bisping, Christian Schneider, Martin Kamp, Lukas Worschech, Sven Hofling, Alfred Forchel, and Yoshihisa Yamamoto. Ultrafast coherent control and suppressed nuclear feedback of a single quantum dot hole qubit. *Nature Physics*, 7(11):872–878, August 2011.

[122] P. Michler, A. Imamoglu, M. D. Mason, P. J. Carson, G. F. Strouse, and S. K. Buratto. Quantum correlation among photons from a single quantum dot at room temperature. *Nature*, 406(6799):968–970, August 2000.

[123] P. Michler, A. Kiraz, C. Becher, W. V Schoenfeld, P. M Petroff, Lidong Zhang, E. Hu, and A. Imamoglu. A quantum dot single-photon turnstile device. *Science*, 290(5500):2282–2285, December 2000.

[124] Charles Santori, Matthew Pelton, Glenn Solomon, Yseulte Dale, and Yoshihisa Yamamoto. Triggered single photons from a quantum dot. *Physical Review Letters*, 86(8):1502–1505, February 2001.

[125] Charles Santori, David Fattal, Jelena Vuckovic, Glenn S. Solomon, and Yoshihisa Yamamoto. Indistinguishable photons from a single-photon device. *Nature*, 419(6907):594–597, October 2002.

[126] R. Hanbury Brown and R. Q. Twiss. A test of a new type of stellar interferometer on sirius. *, Published online: 10 November 1956; | doi:10.1038/1781046a0*, 178(4541):1046–1048, November 1956.

[127] Rick Trebino and Daniel J. Kane. Using phase retrieval to measure the intensity and phase of ultrashort pulses: frequency-resolved optical gating. *Journal of the Optical Society of America A*, 10(5):1101–1111, May 1993.

[128] Govind Agrawal. *Nonlinear Fiber Optics, Fourth Edition.* Academic Press, October 2006.

[129] A. Gröne and S. Kapphan. Direct OH and OD librational absorption bands in $LiNbO_3$. *Journal of Physics and Chemistry of Solids*, 57(3):325–331, March 1996.

[130] M. G. Tanner, C. M. Natarajan, V. K. Pottapenjara, J. A. OConnor, R. J. Warburton, R. H. Hadfield, B. Baek, S. Nam, S. N. Dorenbos, E. Bermdez Urea, T. Zijlstra, T. M. Klapwijk, and V. Zwiller. Enhanced telecom wavelength single-photon detection with NbTiN superconducting nanowires on oxidized silicon. *Applied Physics Letters*, 96(22):221109, 2010.

[131] L. Allen and J. H. Eberly. *Optical Resonance and Two-Level Atoms.* Dover Publications, December 1987.

[132] A. G. Radnaev, Y. O. Dudin, R. Zhao, H. H. Jen, S. D. Jenkins, A. Kuzmich, and T. A. B. Kennedy. A quantum memory with telecom-wavelength conversion. *Nature Physics*, 6(11):894–899, 2010.

[133] Sebastian Zaske, Andreas Lenhard, Christian A Kessler, Jan Kettler, Christian Hepp, Carsten Arend, Roland Albrecht, Wolfgang-Michael Schulz, Michael

Jetter, Peter Michler, and Christoph Becher. Visible-to-telecom quantum frequency conversion of light from a single quantum emitter. *arXiv:1204.6253*, April 2012.

[134] M. Reischle, C. Kessler, W. -M Schulz, M. Eichfelder, R. Robach, M. Jetter, and P. Michler. Triggered single-photon emission from electrically excited quantum dots in the red spectral range. *Applied Physics Letters*, 97(14):143513–143513–3, October 2010.

[135] Muhammad Danang Birowosuto, Hisashi Sumikura, Shinji Matsuo, Hideaki Taniyama, Peter J. van Veldhoven, Richard Ntzel, and Masaya Notomi. Fast purcell-enhanced single photon source in 1,550-nm telecom band from a resonant quantum dot-cavity coupling. *Scientific Reports*, 2, March 2012.

[136] De Greve, K. *et al.* Entanglement between a single quantum dot spin and a telecom-wavelength photon. *Submitted*, 2012.

[137] D. L. Moehring, P. Maunz, S. Olmschenk, K. C. Younge, D. N. Matsukevich, L.-M. Duan, and C. Monroe. Entanglement of single-atom quantum bits at a distance. *Nature*, 449(7158):68–71, September 2007.

[138] Masaki Asobe, Osamu Tadanaga, Hiroshi Miyazawa, Yoshiki Nishida, and Hiroyuki Suzuki. Multiple quasi-phase-matched $LiNbO_3$ wavelength converter with a continuously phase-modulated domain structure. *Optics Letters*, 28(7):558–560, April 2003.

[139] Ron Lifshitz, Ady Arie, and Alon Bahabad. Photonic quasicrystals for nonlinear optical frequency conversion. *Physical Review Letters*, 95(13):133901, 2005.

[140] F. Jelezko and J. Wrachtrup. Single defect centres in diamond: A review. *physica status solidi (a)*, 203(13):3207–3225, October 2006.

[141] C Santori, P E Barclay, K-M C Fu, R G Beausoleil, S Spillane, and M Fisch. Nanophotonics for quantum optics using nitrogen-vacancy centers in diamond. *Nanotechnology*, 21(27):274008, July 2010.

[142] Andrei Faraon, Paul E. Barclay, Charles Santori, Kai-Mei C. Fu, and Raymond G. Beausoleil. Resonant enhancement of the zero-phonon emission from a colour centre in a diamond cavity. *Nature Photonics*, 5(5):301–305, April 2011.

[143] B. B Buckley, G. D Fuchs, L. C Bassett, and D. D Awschalom. Spin-Light coherence for Single-Spin measurement and control in diamond. *Science*, 330(6008):1212–1215, November 2010.

[144] Paulina S. Kuo, Jason S. Pelc, Oliver Slattery, Lijun Ma, Martin M. Fejer, and Xiao Tang. Dual-channel, single-photon upconversion detector at 1300 nm. OSA Technical Digest (online), page NM3C.6. Optical Society of America, June 2012.

[145] M. Asobe, O. Tadanaga, H. Miyazawa, Y. Nishida, and H. Suzuki. Multiple quasi-phase-matched device using continuous phase modulation of $\chi^{(2)}$ grating and its application to variable wavelength conversion. *IEEE Journal of Quantum Electronics*, 41(12):1540– 1547, December 2005.

[146] Joseph W. Goodman. *Statistical Optics*. Wiley-Interscience, August 2000.

[147] W. Martienssen. Coherence and fluctuations in light beams. *American Journal of Physics*, 32(12):919, 1964.

[148] Lijun Ma, Joshua C. Bienfang, Oliver Slattery, and Xiao Tang. Up-conversion single-photon detector using multi-wavelength sampling techniques. *Optics Express*, 19(6):5470–5479, March 2011.

[149] A. Spinelli and A. L Lacaita. Physics and numerical simulation of single photon avalanche diodes. *IEEE Transactions on Electron Devices*, 44(11):1931–1943, November 1997.

[150] A. M Weiner. Femtosecond pulse shaping using spatial light modulators. *Review of Scientific Instruments*, 71(5):1929–1960, May 2000.

[151] Th. Udem, J. Reichert, R. Holzwarth, and T. W. Haensch. Accurate measurement of large optical frequency differences with a mode-locked laser. *Optics Letters*, 24(13):881–883, July 1999.

[152] C.V. Bennett and B.H. Kolner. Principles of parametric temporal imaging. I. System configurations. *IEEE Journal of Quantum Electronics*, 36(4):430–437, April 2000.

[153] Mark A. Foster, Reza Salem, David F. Geraghty, Amy C. Turner-Foster, Michal Lipson, and Alexander L. Gaeta. Silicon-chip-based ultrafast optical oscilloscope. *Nature*, 456(7218):81–84, November 2008.

[154] C. Niclass, C. Favi, T. Kluter, M. Gersbach, and E. Charbon. A 128-by-128 Single-Photon image sensor with Column-Level 10-Bit Time-to-Digital converter array. *IEEE Journal of Solid-State Circuits*, 43(12):2977–2989, December 2008.

[155] Joseph E. Schaar, Jason S. Pelc, Konstantin L. Vodopyanov, and Martin M. Fejer. Characterization and control of pulse shapes in a doubly resonant synchronously pumped optical parametric oscillator. *Applied Optics*, 49(24):4489–4493, 2010.

[156] Phillips, Christopher Richard. *Broadband optical sources based on highly nonlinear quasi-phasematched interactions.* PhD thesis, Stanford University, June 2012.

[157] A Martin, O Alibart, M P De Micheli, D B Ostrowsky, and S Tanzilli. A quantum relay chip based on telecommunication integrated optics technology. *New Journal of Physics*, 14(2):025002, February 2012.

[158] D. Kielpinski, J. F. Corney, and H. M. Wiseman. Quantum optical waveform conversion. *Physical Review Letters*, 106(13):130501, March 2011.

[159] Eyres, Loren Alan. *All-epitaxially orientation-patterned semiconductors for nonlinear optical frequency conversion.* PhD thesis, Stanford University, December 2011.

[160] P. S. Kuo, K. L. Vodopyanov, M. M. Fejer, X. Yu, J. S. Harris, D. F. Bliss, and D. Weyburne. GaAs optical parametric oscillator with circularly polarized and depolarized pump. *Optics Letters*, 32(18):2735–2737, 2007.

[161] V. Tassev, M. Snure, R. Peterson, D. Bliss, G. Bryant, W. Goodhue, S. Vangala, K. Termkoa, A. Lin, J.S. Harris, M.M. Fejer, and C. Yapp. Fast epitaxial growth of thick quasi-phase matched GaP for applications in the MIR and THz: determination of the optimal substrate and pattern orientation. In *Infrared, Millimeter and Terahertz Waves (IRMMW-THz), 2011 36th International Conference on*, pages 1 –2, October 2011.

[162] G. Imeshev, M. A. Arbore, M. M. Fejer, A. Galvanauskas, M. Fermann, and D. Harter. Ultrashort-pulse second-harmonic generation with longitudinally nonuniform quasi-phase-matching gratings: pulse compression and shaping. *Journal of the Optical Society of America B*, 17(2):304–318, February 2000.

[163] P. Baldi, P. Aschieri, S. Nouh, M. De Micheli, D. B Ostrowsky, D. Delacourt, and M. Papuchon. Modeling and experimental observation of parametric fluorescence in periodically poled lithium niobate waveguides. *IEEE Journal of Quantum Electronics*, 31(6):997–1008, June 1995.

[164] Vipul Rastogi, K. Thyagarajan, M. R. Shenoy, P. Baldi, M. De Micheli, and D. B. Ostrowsky. Modeling of large-bandwidth parametric amplification in the čerenkov-idler configuration in planar waveguides. *Journal of the Optical Society of America B*, 14(11):3191–3196, November 1997.